[Papers in Palaeontology, Vol. 12, Part 3, 2026, e70085]

An exquisitely preserved young iguanodontian from the Upper Jurassic of Tanzania sheds light on skeletal fusion patterns within Archosauria

by RICCARDO ROCCHI[1,*], FILIPPO MARIA ROTATORI[2,3,4,*], GABRIEL S. FERREIRA[5,6] *and* FEDERICO FANTI[1,7]

[1]Dipartimento di Scienze Biologiche, Geologiche e Ambientali, University of Bologna, via Zamboni 33, 40126 Bologna, Italy; riccardo.rocchi4@studio.unibo.it, riccardo.rocchi.2001@gmail.com
[2]GEOBIOTEC, Department of Earth Sciences, NOVA School of Science and Technology, Universidade NOVA de Lisboa, P-2829 516 Campus de Caparica, Caparica, Portugal; f.rotatori@campus.fct.unl.pt, filippo.rotatori.93@gmail.com
[3]Museu da Lourinhã, Rua João Luis de Moura 95, 2530-158 Lourinhã, Portugal
[4]Institute of Geological Sciences, Freie Universität Berlin, Malteserstrasse 74–100, 12249 Berlin, Germany
[5]Department of Biology, Faculty of Philosophy, Sciences, and Letters of Ribeirão Preto, University of São Paulo, Av. Bandeirantes 3900, Ribeirão Preto-SP 14040-901, Brazil
[6]Senckenberg Centre for Human Evolution and Palaeoenvironment at the University of Tübingen, Hölderlinstrasse 12, Tübingen 72074, Germany
[7]Collezione di Geologia ‘Museo Giovanni Capellini’, University of Bologna, via Zamboni 63, Bologna 40126, Italy
*Corresponding author

Typescript received 5 September 2025; accepted in revised form 5 April 2026

Abstract: *Dysalotosaurus lettowvorbecki* (Ornithopoda, Dinosauria) is a small-sized dryosaurid iguanodontian known from various isolated remains collected from the Tendaguru Formation (Upper Jurassic, Tanzania). Micro-computed tomography of a small individual encased in a block offered a unique opportunity to describe *c.* 40 associated elements and clarify previously undocumented anatomical details of this species. The preserved material includes cranial elements, an almost complete cervical series, four dorsal vertebrae, and part of the appendicular skeleton. A comprehensive assessment of the individual, based on qualitative features and morphometric analyses, indicates an early ontogenetic stage and an absolute age of 4–5 years. Notably, the cervical vertebrae predominantly exhibit partially closed neurocentral sutures, whereas the two more posterior dorsal vertebrae have open sutures, along with disarticulated neural arches. This finding challenges the simple ‘tail-to-head’ fusion pattern typically assumed for the vertebral series of Ornithopoda, and suggests a potential cervical locus of neurocentral fusion within this clade. Phylogenetic comparative methods indicate a complex distribution of these neurocentral fusion patterns within Archosauria.

Key words: *Dysalotosaurus*, Iguanodontia, Tendaguru Formation, skeletal fusion, neurocentral suture, ontogeny.

IGUANODONTIA is a diverse ornithopod clade, ranging from the Early–Middle Jurassic to the Late Cretaceous (Norman 2004; Rotatori *et al.* 2026). Early-diverging iguanodontians were likely to have been lightly built bipeds (Norman 2004; Maidment & Barrett 2011; Panciroli *et al.* 2025), whereas during the Cretaceous the clade diversified, with several taxa attaining large size and becoming facultatively quadrupedal, ultimately culminating in the highly successful hadrosaurids (Horner *et al.* 2004; Norman 2004; Barrett & Maidment 2017). Late Jurassic iguanodontians appear to be somewhat less diverse, although several specimens have been recovered from North America, Western Europe and Central Africa (e.g. Gilmore 1909; Galton 1981; Carpenter & Wilson 2008; Escaso *et al.* 2014; Carpenter & Galton 2018; Maidment *et al.* 2022; Sánchez-Fenollosa *et al.* 2023; Rotatori *et al.* 2025). Large forms present in Late Jurassic ecosystems, such as *Camptosaurus dispar* (Marsh 1879), *Cumnoria prestwichii* (Hulke 1880), some Iberian taxa (including *Draconyx loureiroi* Mateus & Antunes 2001; *Oblitosaurus bunnueli* Sánchez-Fenollosa *et al.* 2023; SHN.JJS.015, Rotatori *et al.* 2025), and *Uteodon aphanoecetes* (Carpenter & Wilson 2008), are often ascribed to Ankylopollexia (Sereno 1986; Madzia *et al.* 2021). Small iguanodontians dated to Late Jurassic are usually ascribed to Dryosauridae (Sereno 1986; Madzia *et al.* 2021), including the North American genus *Dryosaurus* Marsh 1894, the East African species *Dysalotosaurus lettowvorbecki* Pompeckj 1920, and the Western European *Eousdryosaurus nanohallucis* Escaso *et al.* 2014. Other taxa considered dryosaurids are the Early Cretaceous *Valdosaurus canaliculatus* (Galton 1975), *Elrhazosaurus nigeriensis* (Galton & Taquet 1982) and *Iyuku raathi* Forster *et al.* 2023 (Poole 2023), whereas the enigmatic

doi: 10.1002/spp2.70085

Callovosaurus leedsi (Lydekker 1889) (Ruiz-Omeñaca *et al.* 2006) is from the Middle Jurassic, and *Kangnasaurus coetzeei* Haughton 1915 is from the Late Cretaceous. However, recent analyses recovered *Iy. raathi*, *K. coetzeei* and *Callovosaurus leedsi* as members of Elasmaria or early diverging members of Iguanodontia (Fonseca *et al.* 2024).

Dysalotosaurus lettowvorbecki is pivotal for understanding iguanodontian evolution, being the best-documented dryosaurid and the only Late Jurassic iguanodontian from the southern hemisphere. More than 14 000 catalogued elements from the excavation site Ig/WJ ('iguanodontid'/'Werner Janensch') in Tendaguru are attributed to *Dy. lettowvorbecki* (Hübner 2011; Hübner *et al.* 2021; Schwarz *et al.* 2023). First mentioned by Virchow (1919) and formally diagnosed by Pompeckj (1920), its remains were stored and prepared at multiple German institutions, including the Institut und Museum für Geologie und Paläontologie of the University of Tübingen (GPIT) (Hübner *et al.* 2021). However, due to the early death of Pompeckj and the destruction of part of the prepared material during World War II (Maier 2003; Hübner 2011), only in 1955 did Janensch eventually describe the species, using newly prepared and mostly isolated elements in conjunction with the sketches of Pompeckj (Janensch 1955). In addition, thousands of elements from the Ig/WJ quarry in Tendaguru remain unprepared (Hübner *et al.* 2021; Schwarz *et al.* 2023). Subsequently, Galton (1977, 1981, 1983, 1989) redescribed the taxon and proposed a genus synonymy with *Dryosaurus*. However, later studies re-established the validity of the genus *Dysalotosaurus*, based on numerous anatomical differences (Hübner & Rauhut 2010; Hübner 2011, 2018). More recently, the abundance of isolated elements of the species enabled detailed studies of its palaeopathology (Witzmann *et al.* 2008, 2011), ontogeny (Hübner & Rauhut 2010; Hübner 2018), histology (Hübner 2012), endocranial anatomy (Sobral *et al.* 2012; Lautenschlager & Hübner 2013) and taphonomy (Hübner *et al.* 2021).

A newly identified block at GPIT contains a small, semi-articulated specimen of *Dy. lettowvorbecki* catalogued as GPIT-PV-122984 and offers a rare chance to examine the associated material of the species. This study aims to describe the specimen and assess its ontogenetic stage, discussing the anatomy and the ontogenetic changes of *Dy. lettowvorbecki* and, moreover, providing new insights into the life history of dinosaurs in general.

Institutional abbreviations. BSPG, Bayerische Staatssammlung für Paläontologie und Geologie, München, Germany; CM, Carnegie Museum, Pittsburgh, PA, USA; GPIT, Institut und Museum für Geologie und Paläontologie of the University of Tübingen, Germany; GZG, Geowissenschaftliches Zentrum, University of Göttingen, Germany; MB, Museum für Naturkunde, Berlin, Germany; NHMUK, Natural History Museum, London, UK; RBINS, Royal Belgian Institute of Natural Sciences, Brussels, Belgium; SHN, Sociedade de Historia Natural, Torres Vedras, Portugal; SMNS, Staatliches Museum für Naturkunde, Stuttgart, Germany; YPM, Peabody Museum, Yale College, New Haven, CT, USA.

GEOLOGICAL CONTEXT

The Tendaguru area, located *c.* 60 km from Lindi in coastal southern Tanzania, was first reported in 1906, after the recovery of massive pieces of bone (Fraas 1908; Hübner *et al.* 2021). Between 1909 and 1913, the Museum für Naturkunde (MB) exploited the fossil sites in the area, leading the German Tendaguru Expedition (GTE), which extracted *c.* 230 metric tons of mostly dinosaur fossils (Janensch 1914a; Maier 2003; Díez Díaz *et al.* 2025). The GTE was followed by the British Tendaguru Expedition (1924–1931) and later the German–Tanzanian Tendaguru Expedition (GTTE 2000) (Aberhan *et al.* 2002; Bussert *et al.* 2009). The GTE yielded abundant remains of sauropods (e.g. Janensch 1914b), *Kentrosaurus* Hennig 1915, *Elaphrosaurus bambergi* Janensch 1920, and more than 14 000 catalogued elements attributed to the small iguanodontian *Dysalotosaurus lettowvorbecki* (Hübner 2011; Hübner *et al.* 2021).

Bussert *et al.* (2009) elevated the previously called Tendaguru beds in the Lindi hinterland ('Tendaguruschichten') to the rank of Tendaguru Formation (Fig. 1A). These deposits, ranging from the middle Oxfordian to the Hauterivian, accumulated under multiple transgressive–regressive events and have been subdivided into six members (Fig. 1B, C), in ascending order: Lower Dinosaur Member, Nerinella Member, Middle Dinosaur Member, *Indotrigonia africana* Member, Upper Dinosaur Member, and *Rutitrigonia bornhardti-schwarzi* Member (Bussert *et al.* 2009).

All known *Dy. lettowvorbecki* material, and probably GPIT-PV-122984, were recovered from the Ig/WJ quarry, where the Middle Dinosaur Member (MDM) is exposed (Fig. 1C). Around Tendaguru Hill, the MDM reaches 13–30 m in thickness and has been dated to the late Kimmeridgian based on dinoflagellate cyst assemblage (Bussert *et al.* 2009; Hübner *et al.* 2021). Its sedimentology indicates a transition from tidal flats to sabkha-like coastal plains (Bussert *et al.* 2009), with ostracod assemblages that show a transition from marine to freshwater conditions upwards (Sames 2008). *Dysalotosaurus lettowvorbecki* are found in monodominant bonebeds, with the taxon representing more than 90% of identified fossils (Hübner *et al.* 2021). Most material consists of isolated

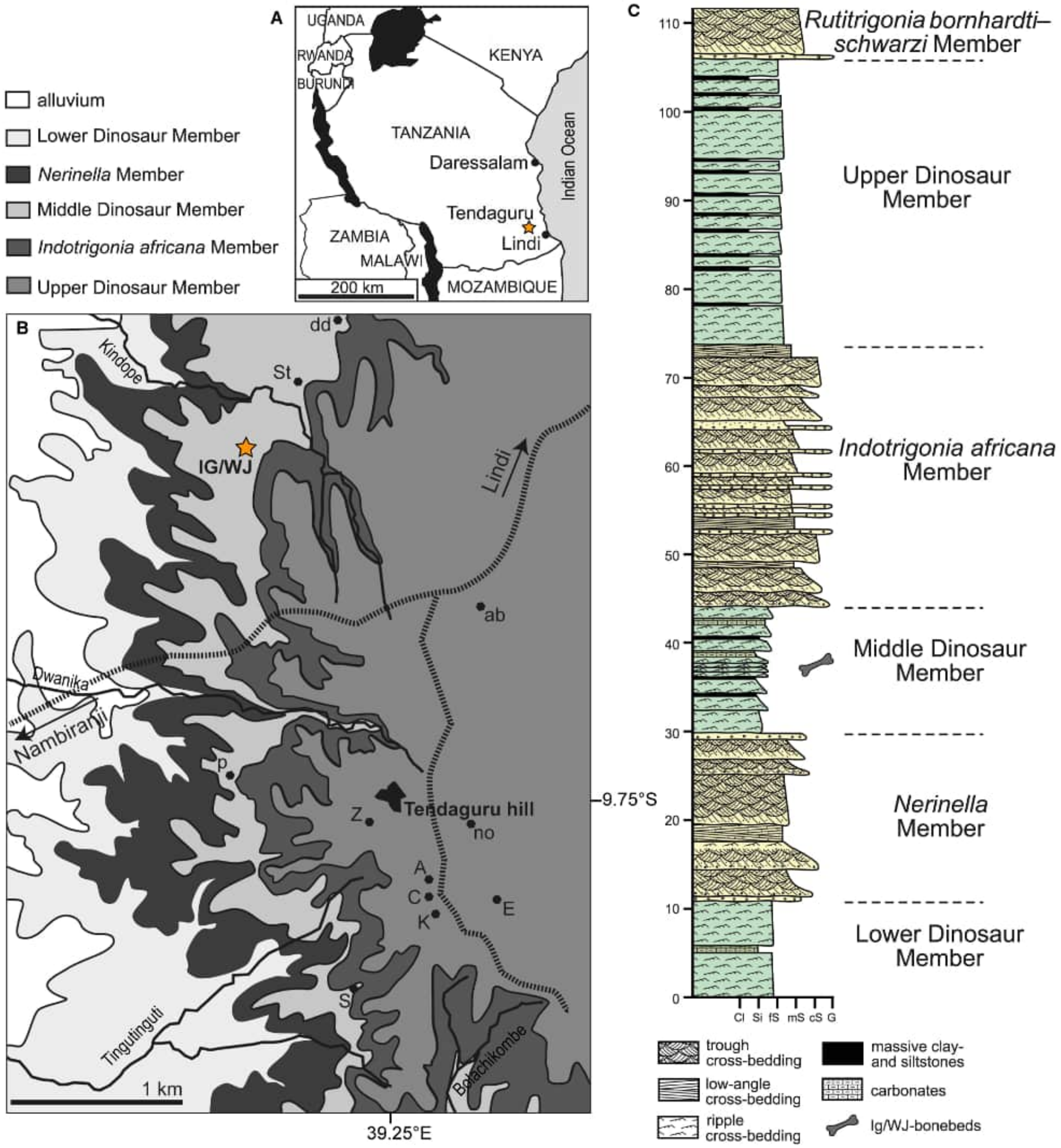

FIG. 1. The Tendaguru Formation. A, position of the Tendaguru locality in Tanzania, marked with an orange star. B, geological map of the Tendaguru area with the main stratigraphic units; the position of the Ig/WJ quarry is marked with an orange star, and some other important quarries from the German Tendaguru Expedition are labelled with their respective letters; roads are marked by dashed lines. C, simplified composite section of the Tendaguru Formation in the type area (based on Bussert *et al.* 2009); the position of the Ig/WJ bonebeds is only approximate, based on the field results of the German–Tanzanian Tendaguru Expedition; green marks the Dinosaur members, yellow marks the intermediate members. *Abbreviations*: Cl, clay; cS, coarse-grained sand; fS, fine-grained sand; G, gravel; mS, medium-grained sand; Si, silt. All images are modified from Hübner *et al.* (2021).

elements, with a few semi-articulated and associated skeletons (Hübner *et al.* 2021). Although the exact stratigraphic position of the bonebeds is uncertain, the geographic location of the site suggests attribution to the middle part of the MDM (Aberhan *et al.* 2002; Hübner *et al.* 2021).

Of the four bonebeds of the Ig/WJ quarry that were excavated during the GTE (Reck 1913; Janensch 1914b), the third ('Iguanodontenschicht') and fourth ones were the most productive. The third bonebed yielded numerous well-preserved specimens between 1910 and 1912, whereas the fourth bonebed, accessed later in 1912, contained smaller individuals and was described as a 'large herd of small saurians' ('große Herde kleiner Saurier') (Hübner *et al.* 2021). The excavation number of GPIT-PV-122984, which is '9827', indicates that the specimen should have been extracted from the fourth bonebed (Hübner *et al.* 2021). During the years, different taphonomic interpretations have been proposed: Janensch (1914b) suggested reworking by wave action, whereas other authors proposed attritional mortality during drought events (Russell *et al.* 1980; Heinrich 1999). Hübner (2011, 2012) hypothesized a single mass death event, and Hübner *et al.* (2021) argued for multiple catastrophic events linked to repeated tidal channel crossings.

MATERIAL & METHOD

Studied material

The specimen GPIT-PV-122984 is a block that has never been fully prepared, leaving numerous embedded elements in a mudstone matrix (Fig. 2). A label signed by Dr Philipe Havlik in December 2009 tentatively identified it as 'Tendaguru material': its fine-grained matrix, bone colouration and morphology (notably of the femur and vertebrae), together with its small size, support its attribution to *Dy. lettowvorbecki* from the Tendaguru area.

The specimen bears the field number 9827 painted on a flat bone, probably corresponding to one of the WJ-series labels assigned during the GTE (Hübner *et al.* 2021). According to the Hans Reck 1912–1913 field catalogue, numbers from 9800 to 9860 were assigned on 20 November 1912, probably to material of the fourth bonebed of the Ig/WJ quarry ('große Herde kleiner Saurier' *sensu* Reck 1913). The small size of GPIT-PV-122984 is consistent with what is described for the *Dy. lettowvorbecki* material coming from this specific bonebed (Reck 1913). In addition, Hübner *et al.* (2021) recovered most of the *Dy. lettowvorbecki* specimens stored at GPIT as originating from the fourth bonebed.

Data acquisition & 3D imaging

A textured surface 3D model of GPIT-PV-122984 was digitized with an Artec Spider hand scanner using ArtecStudio 14 Professional (Artec 3D, Luxembourg) and exported in polygon file format (.ply).

The specimen GPIT-PV-122984 was scanned using micro-computed tomography (μ-CT) at the 3D Imaging Lab of the University of Tübingen using a Nikon XT H 320 with a tungsten reflection target with a maximum voltage of 225 kV. The CT scanning was performed at 195 kV and 165 μA, using a copper filter 0.5 mm thick. A total of 4476 projections were taken, holding four frames per projection at 354 ms and 0.05659851 mm voxel size. The resulting CT data were manually segmented in Amira 2021.1 (Thermo Fisher Scientific). A surface mesh was generated for each element segmented, with a smoothing extent factor of 5, then exported in polygon file format (.ply) and imported into Blender v4.4.1 (https://www.blender.org/) for articulation (Fig. 3) and rendering (detailed information in Appendix S1). 3D meshes and micro-CT image series are available in MorphoSource (Rocchi *et al.* 2026a; individual record links in Appendix S1, Table S1.1).

Measurements

All skeletal measurements were taken digitally in Blender, with semicircular canal lengths obtained using the MeasureIt add-on (Vazquez 2024). A summary of postcranial measurements is provided in Table 1. The complete set of measurements is reported in Appendix S1 (Tables S1.2–S1.19). Measurements were taken following the definitions of Hübner & Rauhut (2018), when possible.

Ontogenetic stage assessment

To confidently assess the ontogenetic stage of GPIT-PV-122984, different proxies were considered (Griffin *et al.* 2021). Cranial element fusion was described following Bailleul *et al.* (2016), and Hübner & Rauhut (2010) more specifically for *Dy. lettowvorbecki*. The degree of neurocentral suture closure was assessed after Hübner (2018), using the nomenclature of Brochu (1996). In particular, a 'closed' vertebra is defined as 'one in which the neurocentral suture is no longer visible'. An open vertebra is defined as 'completely visible from all aspects, and the centrum and neural arch can be separated easily'. A partially closed vertebra is 'one in which the suture has started closing, but is still discernible'.

Other qualitative traits and ratios were considered, which have been shown to vary ontogenetically in *Dy. lettowvorbecki* (Hübner & Rauhut 2010; Hübner 2018) or *Dryosaurus elderae* Carpenter & Galton 2018 (Dunfee 2022).

A multivariate morphometric analysis was also performed following Rotatori *et al.* (2020). Measurements produced on the femur and tibia of GPIT-PV-122984

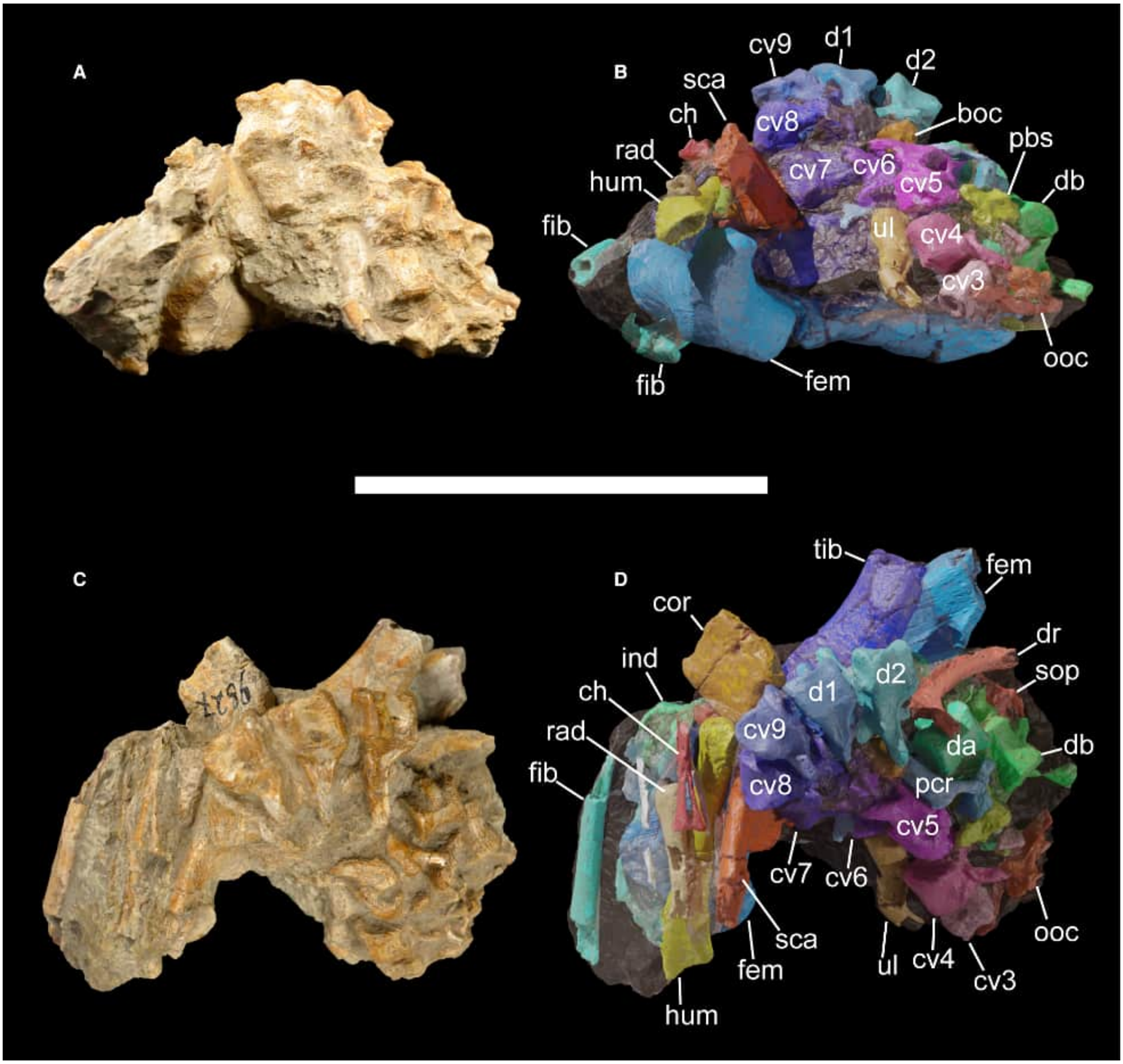

FIG. 2. The GPIT-PV-122984 block. A, view from a side of the block. B, segmentation of the CT data in the same view as A. C, view of the block from above the semi-articulated vertebral series. D, segmentation of the CT data in the same view as C. *Abbreviations*: boc, basioccipital; ch, chevron; cor, coracoid; cv3–9, cervical vertebrae 3–9; d1–2, dorsal vertebrae 1–2; da, dorsal vertebra Da; db, dorsal vertebra Db; dr, dorsal rib; fem, femur; fib, fibula; hum, humerus; ind, indeterminate cranial bone; ooc, otoccipital; pbs, parabasisphenoid; rad, radius; sca, scapula; sop, supraoccipital; tib, tibia; ul, ulna. Scale bar represents 100 mm.

were added to the *Dy. lettowvorbecki* datasets produced by Hübner (2018). Two principal component analyses (PCAs) were performed on both the femora and tibiae datasets (including GPIT-PV-122984) separately, enabling GPIT-PV-122984 to be plotted in two *Dy. lettowvorbecki* population morphospaces. These analyses aimed to obtain a first principal component (PC1) that explains a major part of the total variance of each metric dataset, given that in this case it is safe to assume that this component approximately represents a 'size axis' (Hammer & Harper 2008). Subsequently, two reduced major axis (RMA) regressions were performed, one for each dataset (both including GPIT-PV-122984), with PC1 scores regressed against the log-transformed geometric means of the measures of each specimen. Because the growth of the hindlimb long bones is described by a power function, the geometric mean is a reliable proxy of absolute size (Klingenberg 1996). Given that size has been demonstrated to be a reliable indicator of age in *Dy. lettowvorbecki* (Hübner 2012, 2018), the obtained

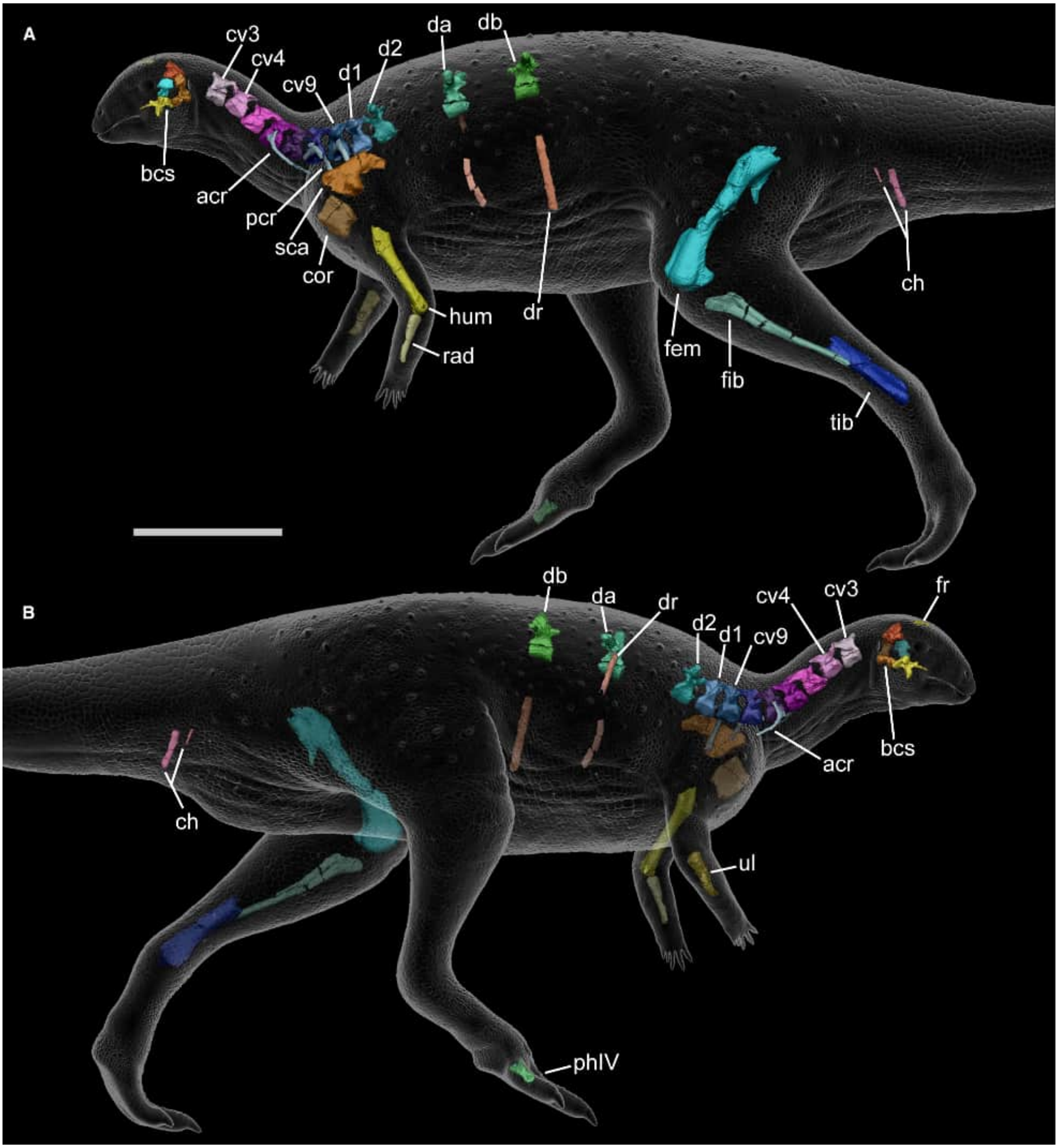

FIG. 3. Elements of GPIT-PV-122984 mounted in their anatomical position. A, left lateral view. B, right lateral view. *Abbreviations*: acr, anterior cervical rib; bcs, braincase; ch, chevron; cor, coracoid; cv3–9, cervical vertebrae 3–9; d1, first dorsal vertebra; d2, second dorsal vertebra; da, anterior dorsal vertebra; db, posterior dorsal vertebra; drb, dorsal rib; fem, femur; fib, fibula; fr, frontal; hum, humerus; otc, otoccipital; pcr, posterior cervical rib; ph, phalanx; rad, radius; sca, scapula; tib, tibia; ul, ulna. Scale bar represents 100 mm. Life reconstruction by Fabio Manucci.

RMA regressions enable the growth series of the *Dy. lettowvorbecki* population and the position of GPIT-PV-122984 in them, to be elucidated. The entire analytical workflow was carried out in R v4.3.3 (R Core Team 2024), using the following packages: ade4 v1.7–23 (Dray & Dufour 2007; Dray *et al.* 2025); ggplot2 v3.5.0; tidyr v1.3.1 (Wickham *et al.* 2024, 2025); ggrepel v0.9.6 (Slowikowski *et al.* 2024). The missing data were replaced with

TABLE 1. Postcranial most representative measurements (in mm).

Element	Measurement	
Cervical vertebrae	Anteroposterior centrum ventral length	12.7 (min)–14.8 (max)
	Anteroposterior centrum dorsal length	10.1 (min)–13.6 (max)
	Posterior centrum dorsoventral height	7.8 (min)–10.6 (max)
	Anterior centrum dorsoventral height	7.0 (min)–10.3 (max)
Dorsal vertebrae	Anteroposterior centrum ventral length	12.4 (min)–13.7 (max)
	Anteroposterior centrum dorsal length	13.6 (min)–16.1 (max)
	Posterior centrum dorsoventral height	7.0 (min)–8.8 (max)
	Anterior centrum dorsoventral height	8.0 (min)–9.5 (max)
Scapula	Shaft minimum	11.7
	Maximum width distally between acromion process and glenoid	29.1
Coracoid	Length between sternal process and lateroventral corner	23.4
	Minimum dimension between the dorsal concavity and the lateroventral corner	19.5
Humerus	Minimum shaft width	6.9
	Length distal from the deltopectoral crest to the condyles	49.5
Radius	Minimum shaft thickness mediolaterally	5.9
Ulna	Medial or lateral minimum shaft thickness	6.1
Femur	Maximum lateromedial width distally	33.7
	Partial length from the posterior nutrient foramen to the distal end laterally	96.0
	Midshaft circumference	53.4
Tibia	Maximum width of the distal end	38.0
Fibula	Maximum width proximally	18.7
Phalanx	Median total length	15.3

the average value of the specimens for that feature, and all of the measurements were log-transformed prior to PCA, to explore metric linear relationships of the variables measured (Hammer & Harper 2008). PC1 and PC2 (second principal component) scores were all multiplied by −1 for graphical purposes, to produce inverted scores. The inverted PC1 scores were then regressed against the log-transformed geometric means of the measures of each specimen, obtained without replacing missing data. Scripts and datasets used for the morphometric analyses are available in Rocchi *et al.* (2026b). The age of GPIT-PV-122984 was estimated using the formula proposed by Hübner *et al.* (2021), which found a strong correlation between the distal femur width and the age for *Dy. lettowvorbecki*, based on the histology of 19 specimens (Hübner 2012).

Ancestral state reconstruction

The new information on the neurocentral suture fusion of *Dy. lettowvorbecki* was used to investigate vertebral fusion patterns in Archosauromorpha, considering the presence or absence of loci of neurocentral fusion. Verrière *et al.* (2022) defined a locus as a point from which ossification spreads, whether it is the first vertebrae in which ossification centres are visible or the first vertebrae in which given elements (as is the case for the neurocentral sutures) begin to fuse. A dataset was compiled from a deep literature review, recording the presence (1) or absence (0) of loci in the cervical and caudal series of various archosauromorphs (complete list in Appendix S3, Table S3.1). The information used by Verrière *et al.* (2022) was revised: ambiguous data for *Allosaurus* and many species of bird genera (Gilmore 1920; Starck 1993) were excluded; *Bonitasaura* and *Dromaius* were recoded for this study as possessing both cervical and caudal loci (Gallina 2011; Caldwell *et al.* 2024). For *Dysalotosaurus*, a caudal locus of fusion (state 1) was already recognized by Hübner (2018), who described a ‘tail-to-head’ pattern of neurocentral closure. However, GPIT-PV-122984 demonstrated the additional presence of a cervical locus of fusion (state 1), previously considered absent (state 0).

Using phylogenetic comparative methods following Verrière *et al.* (2022), we performed two ancestral state reconstructions (ASRs) on the archosauromorph dataset to trace the evolution of the neurocentral fusion loci within the clade. A supertree of the selected taxa was composed as a nexus file in Mesquite v3.81 (Maddison & Maddison 2021), using published phylogenies (Wilson 2002; Nesbitt 2011; Yu *et al.* 2020; Rotatori *et al.* 2023; Cau 2024; Lania *et al.* 2025). The ASRs were performed by importing supertree and the dataset into R v4.3.3 (R Core Team 2024), using the following packages: ape (Paradis & Schliep 2018); phytools (Revell 2024);

paleotree (Bapst 2012); geiger (Harmon *et al.* 2008). The supertree was time-calibrated using the first appearance datum and the last appearance datum of each of its tips, that is to say, every taxon included in the analysis, as reported by the Paleobiology Database (https://paleobiodb.org/; Uhen *et al.* 2023). Two separate ASRs were carried out with a maximum likelihood approach, using an all rates are different (ARD) model, one for the cervical locus and one for the caudal locus, respectively, and results were then plotted as percentage pies on the nodes of a time-calibrated supertree. Given the small size of the phylogenetic tree and the dataset, model choice has little impact on the outcome in terms of statistical fitting. Script and data used for the ASRs are available in Rocchi *et al.* (2026b).

Phylogenetic analysis

Phylogenetic analyses were performed by adding GPIT-PV-122984 to the matrix of Poole (2022), following the character list of Poole (2023). As is the case for *Dy. lettowvorbecki*, the coding for ornithopod operational taxonomic units (OTUs) is often based on immature individuals. To calibrate this issue, Poole (2022) detected as ontogenetically sensitive characters (OSCs) the traits that differed between the scoring of juvenile specimens of *Orodromeus*, *Dryosaurus* and *Hypacrosaurus* and their respective adult form. Poole (2022) carried out four different phylogenetic analyses. In the fourth analysis, scorings were based on skeletally mature specimens, when it was possible, while for species represented only by immature individuals the OSCs were rescored as unknown (‘?’). In the present study, the fourth analysis of Poole (2022) was replicated with modifications: both the juvenile and adult OTUs of *Orodromeus*, *Dryosaurus* and *Hypacrosaurus* were included, and for species known only from skeletally immature individuals, including *Dy. lettowvorbecki* (also *Gasparinisaura*, *Leaellynasaura*, *Anabisetia*, *Iyuku* and *Bolong*), both the normal OTU codification and the OSC version were retained. GPIT-PV-122984, identified as an early ontogenetic stage, was therefore represented by two OTUs (GPIT-PV-122984 and GPIT-PV-122984 OSC). A matrix of 323 characters for 80 OTUs was edited using Mesquite v3.81 (Maddison & Maddison 2021). *Eocursor* was set as the outgroup.

Five phylogenetic analyses were run in TNT v1.6 (Goloboff & Morales 2023) on the modified dataset, using New Technology search strategies to search for the most parsimonious trees (MPTs), using a script modified from Vila *et al.* (2022). Each run included 100 rounds of sectorial searches, 100 cycles of tree-drifting, 100 cycles of ratchet, and 10 rounds of tree fusing. For sectorial searches, a minimum sector size of 5 was chosen, and random sector selections and 100 cycles of constraint-based selection with a minimum fork of 5 were used. For tree-drifting, the trees with a maximum difference in absolute fit of 5 and a maximum difference in relative fit of 0.1 were explored. All other settings were left at their default values.

One analysis used equal weighting (EW) of characters, whereas the other four used extended implied weighting (EIW), with k-values of 3, 5, 10 and 11, following the range proposed by Ezcurra (2024) for 80 OTUs. A strict consensus tree was calculated on the optimal trees of each analysis, with synapomorphies identified for each clade. Node robustness of each consensus tree was assessed using bootstrap values (1000 replicates) and Bremer supports (keeping trees suboptimal by 10 steps). The script and character matrix used for the phylogenetic analyses and the resulting consensus trees are available in Rocchi *et al.* (2026b).

SYSTEMATIC PALAEONTOLOGY

DINOSAURIA Owen 1842 (*sensu* Madzia *et al.* 2021)
ORNITHISCHIA Seeley 1888 (*sensu* Madzia *et al.* 2021)
ORNITHOPODA Marsh 1881 (*sensu* Madzia *et al.* 2021)
IGUANODONTIA Baur 1891 (*sensu* Madzia *et al.* 2021)
DRYOMORPHA Sereno 1986 (*sensu* Madzia *et al.* 2021)
DRYOSAURIDAE Milner & Norman 1984 (*sensu* Madzia *et al.* 2021)

Genus *Dysalotosaurus* Pompeckj 1920
Dysalotosaurus lettowvorbecki Pompeckj 1920

Cranial skeleton

Different disarticulated but associated cranial elements were identified, mostly from the braincase (Fig. 4A). Their lack of fusion suggests that they were connected by cartilage in life.

Basioccipital. The basioccipital is preserved as an isolated element with a rhomboidal outline in dorsal view (Fig. 5E, F). Its posterior portion comprises most of the occipital condyle, with a smooth articular surface for the atlas–axis complex, partially eroded on its left side (Fig. 5A, B, D, E). On the dorsal surface, irregular lateral facets for the otoccipitals indicate that the basioccipital had a limited contribution (*c.* 3 mm) to the ventral margin of the foramen magnum (Fig. 4B). Dorsally, the medial surface is gently transversely concave, forming the posterior braincase floor (Fig. 5C, D, F). The ventral lip of the basioccipital component of the occipital condyle has a single, rounded posterior tip, anterior to which a low step develops into the neck that separates the condyle from the anteriorly located, ventrally projecting basioccipital contribution to the basal tubera. Therefore, the ventral surface has a concave profile in lateral view (Fig. 5A, B). The narrowest lateral width of the neck is located

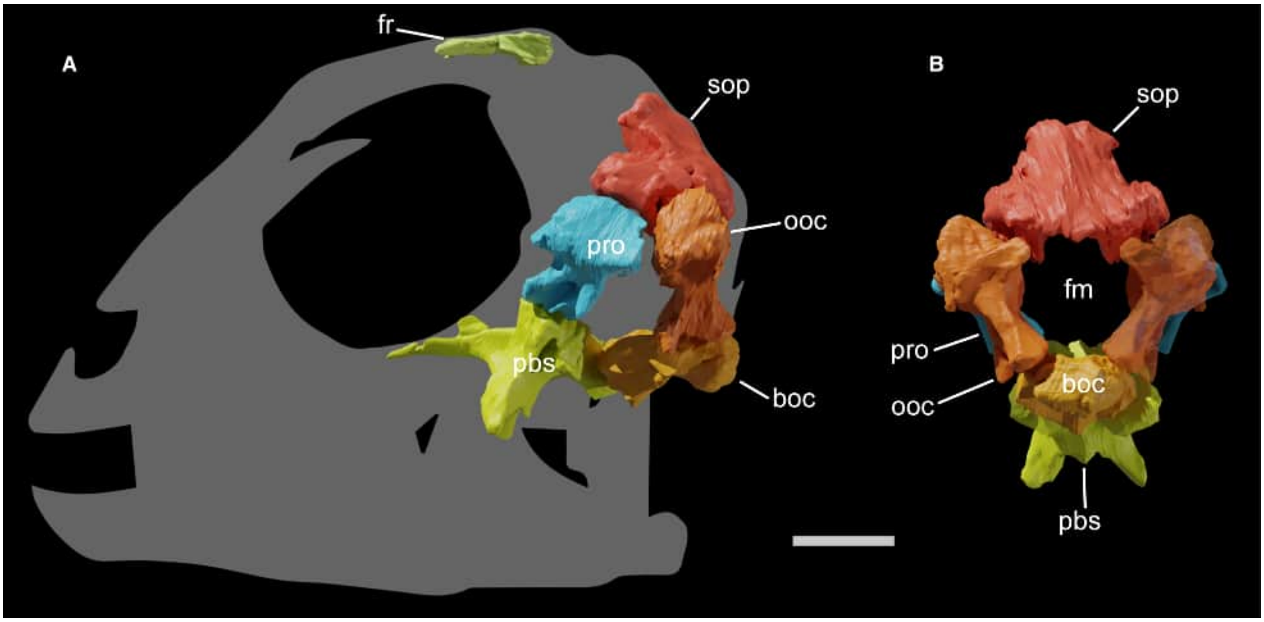

FIG. 4. Cranial skeleton of GPIT-PV-122984. A, preserved cranial elements mounted in anatomical position in left lateral view. B, braincase in occipital view. Right otoccipital and prootic and parabasisphenoid contribution to the left basal tuber is reconstructed by mirroring the contralateral element. *Abbreviations*: boc, basioccipital; fm, foramen magnum; fr, frontal; ooc, otoccipital; pbs, parabasisphenoid; pro, prootic; sop, supraoccipital. Scale bar represents 10 mm. Silhouette modified from Lautenschlanger & Hübner (2013).

near the edge of the articular surface of the condyle, while the anterior part is wider than the condyle itself. The basioccipital contribution to the basal tubera is formed by two laterally protruding tubercles, connected by a transverse ridge on the ventral surface. This ridge extends ventrally below the level of the occipital condyle and would have contacted the parabasisphenoid anteriorly (Fig. 5A–E), contributing to the most posterior part of the basal tubera. Medially, the ridge forms a triradiate structure, with a very short but prominent median keel (Fig. 5E). Anterior to the transverse ridge, a rounded articular surface probably penetrated deep above the basisphenoid (Fig. 5E, F). No foramina are evident.

Remarks. The basioccipital of GPIT-PV-122984, with a concave ventral surface between a smooth contribution to the occipital condyle and a well-developed contribution to the basal tubera, resembles that of dryosaurids, such as *Dryosaurus* (Galton 1983; Dunfee 2022) and *Dy. lettowvorbecki* (Sobral *et al.* 2012). Its rhomboidal outline closely resembles the early ontogenetic stages of *Dy. Lettowvorbecki* as in MB.R.3536 (Hübner & Rauhut 2010), whereas the contribution to the occipital condyle is more prominent in advanced ontogenetic stages of dryosaurids (e.g. *Dy. lettowvorbecki* dyA/MB.R.1373) and in larger iguanodontians (Norman 1980, 1986; Hübner & Rauhut 2010; Carpenter & Lamanna 2015; Lockwood *et al.* 2024). In GPIT-PV-122984, the basioccipital contributed only slightly to the ventral margin of the foramen magnum, as in dryosaurids (Galton 1983; Hübner & Rauhut 2010), *Ca. dispar* (Gilmore 1909), *Comptonatus chasei* Lockwood *et al.* 2024 and *Tenontosaurus tilletti* Ostrom 1970 (Thomas 2015). By contrast, the basioccipital in non-iguanodontian ornithopods such as *Hypsilophodon foxii* Huxley 1870 (Galton 1974) shows a broader participation, whereas in some large iguanodontians such as *Iguanodon bernissartensis* Boulenger 1881 and ‘*Dollodon bampingi*’ Paul 2008 the basioccipital is excluded altogether (Norman 1980, 1986). As in most iguanodontians, GPIT-PV-122984 does not present a midline ridge on the dorsal surface (endocranial floor) of the basioccipital (e.g. Norman 1980; Hübner & Rauhut 2010), in contrast to *Jeholosaurus shangyuanensis* Xu *et al.* 2000 (Bertozzo *et al.* 2025) and *Thescelosaurus neglectus* Gilmore 1913 (Boyd 2014). The basioccipital contribution to the basal tubera of GPIT-PV-122984 resembles *Dy. lettowvorbecki* dyA/MB.R.1373 and *Dr. elderae*, both with a short median keel (Hübner & Rauhut 2010; Sobral *et al.* 2012; Dunfee 2022). In contrast, Galton (1983, fig. 1c) illustrated a ventral keel for *Dryosaurus altus* (Marsh 1878) that is notably more elongated than in GPIT-PV-122984, similar to some thescelosaurids (Boyd 2014; Avrahami *et al.* 2024). The transverse ridge of GPIT-PV-122984 is more prominent than in *Dr. elderae* (Dunfee 2022), extending below the level of the occipital condyle, a condition also seen in *Cu. prestwichii*, *Ca. dispar* (McDonald 2011) and *Te. tilletti* (Galton 1989), although these taxa lack a keel and possess a button-like basioccipital contribution to the basal tubera. In GPIT-PV-122984, the basioccipital contribution to the basal tubera is relatively less developed, similar to the condition documented photographically for *Dy. lettowvorbecki* dyA/MB.R.1373, where, even if not reported in any description, the basal tubera (composed of parabasisphenoid and basioccipital) clearly extend below the level of the occipital condyle (Hübner & Rauhut 2010, fig. 7A). The anterior prolongation that inserts between the two lateral parabasisphenoid contributions to the basal tubera in GPIT-PV-122984 matches the condition documented in *Dy. lettowvorbecki* dyA/MB.R.1373 (Janensch 1955) and, as previously observed by Dieudonné *et al.* (2021), *Dryosaurus* (Carpenter & Lamanna 2015, fig. 7C) and *Ca. dispar* (Gilmore 1909, pp. 206, 208; Carpenter & Lamanna 2015, fig. 7D).

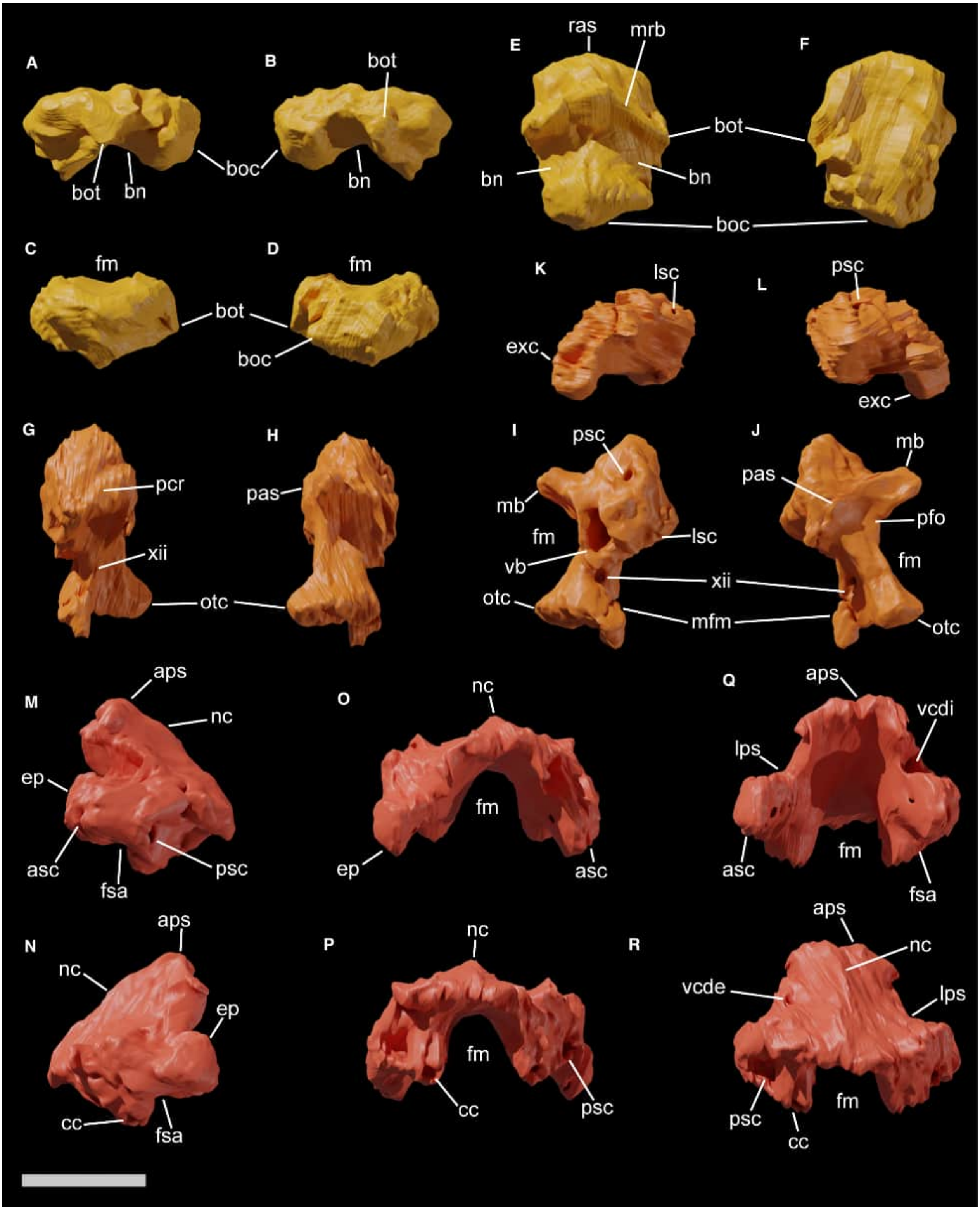

FIG. 5. Cranial skeleton of GPIT-PV-122984. A–F, basioccipital in: A, left lateral; B, right lateral; C, anterior; D, posterior; E, ventral; F, dorsal view. G–L, left otoccipital in: G, lateral; H, medial; I, anterior; J, posterior; K, ventral; L, dorsal view. M–R, supraoccipital in: M, left lateral; N, right lateral; O, anterior; P, posterior; Q, ventral; R, dorsal view. *Abbreviations*: asc, anterior semicircular canal; aps, ascending process of the supraoccipital; bn, basioccipital neck; boc, basioccipital contribution to occipital condyle; bot, basioccipital contribution to the basal tubera; btr, basioccipital transverse ridge; cc, common crus; otc, otoccipital condyloid; ep, epiotic co-ossification (or anterior process of supraoccipital); fm, foramen magnum; fsa, fossa subarcuata; lps, lateral process of the supraoccipital; lsc, lateral semicircular canal; mb, medial bridge; mfm, metotic fissure posterior margin; mrb, medial ridge of the basioccipital; nc, nuchal crest; pas, proatlas articular surface; pcr, prootic crest; pfo, posterior fossa of the otoccipital; psc, posterior semicircular canal; ras, rounded articular surface; vcd, vena capitis dorsalis (e external, i internal) foramen; vb, vestibule; xii, foramen for the cranial nerve XII. Scale bar represents 10 mm.

Otoccipital. The left exoccipital and left opisthotic are fused into a complex, also defined as the otoccipital (*sensu* Kuzmin *et al.* 2021), with no visible sutures. Preserved as an isolated element, it lacks the paroccipital process and much of the anteroventral region. Ventrally, a rugose facet for the basioccipital is present (Fig. 5K), whereas posteroventrally, a squared condyloid contributed to the dorsal part of the occipital condyle (Fig. 5G, H, J). A pillar-like process, slightly twisted mediolaterally above the condyloid, formed the left margin of the foramen magnum (Figs 4B, 5J). At the dorsomedial corner of this margin lies a shallow depression, forming a posterior fossa of the otoccipital, surmounted by a transversely elongated, slightly convex proatlas facet (Fig. 5H, J). A medial bridge of the otoccipital further contributed to the left dorsolateral margin of the foramen magnum (Fig. 5I, J), probably excluding the participation of most of the supraoccipital, although its medial-most portion appears to be eroded (Fig. 4B). The supraoccipital should have draped over the left (and right) otoccipital (Fig. 3B), contacting it on its rugose dorsomedial surface, which preserves the cross-section of the posterior semicircular canal in its anterior portion (Fig. 5I, L). Anterior to the condyloid, the lateral surface curves anterolaterally, suggesting the presence of the broken crista tuberalis (*sensu* Sampson & Witmer 2007) and the posterior margin of the metotic fissure (Fig. 5I, J). However, in the area posterior to the breakage surface, a neurovascular foramen probably including the posterior ramus of the hypoglossal nerve (CN XII) is preserved (Fig. 5I, J). In the dorsolateral wall, the base of the paroccipital process is marked by a concavity bounded by two crests, the dorsalmost being the prootic crest (Fig. 5G), which continues into the left prootic. This anterior facet, although damaged, shows the cross-sections of the vestibule on its ventral portion and of the anterior semicircular canal on its lateral portion (Fig. 5I). The medial surface of the left otoccipital is broadly concave, forming the left posterolateral braincase wall (Fig. 5H, I).

Remarks. In GPIT-PV-122984 the exoccipital and opisthotic are fused into an otoccipital, as in most ornithopods (Norman 2004). The participation in the occipital condyle of the otoccipital of GPIT-PV-122984 is comparable to dryosaurids (Galton 1983; Hübner & Rauhut 2010), *Ca. dispar* (Gilmore 1909) and *Te. tilletti* (Thomas 2015), but less extensive than in many rhabdodontomorphs (Weishampel *et al.* 2003; Chanthasit 2010; Zanno *et al.* 2023), whereas the otoccipitals appear not to participate in the occipital condyle in *Ouranosaurus nigeriensis* Taquet 1976. The left otoccipital of GPIT-PV-122984 does not appear to contact its counterpart ventrally to form the foramen magnum floor, resembling the condition in dryosaurids (Galton 1983; Hübner & Rauhut 2010), *Ca. dispar* (Gilmore 1909), *Co. chasei* (Lockwood *et al.* 2024) and *Te. tilletti* (Thomas 2015), but unlike *Ig. bernissartensis* (Norman 1980). The posterior fossa of the otoccipital and the proatlas facet of GPIT-PV-122984 are similar to that in *Dy. lettowvorbecki* BSPG AS I 834 (Hübner & Rauhut 2010), whereas they are less developed than in *Ca. dispar* (Carpenter & Lamanna 2015), *Cu. prestwichii* (Maidment *et al.* 2022) and *Th. neglectus* (Boyd 2014). The dorsolateral depressed surface of the otoccipital of GPIT-PV-122984 resembles the description provided for *Dy. lettowvorbecki* (Sobral *et al.* 2012), and it is shallower than in *Dr. elderae* (Carpenter & Lamanna 2015).

Supraoccipital. The supraoccipital was found as an isolated but nearly complete element. Its posterior surface is anterodorsally inclined, and it shows a triradiate morphology, formed by a dorsal ascending process and two lateral processes (Fig. 5Q, R). Each lateral process bears a subrectangular facet for an otoccipital (Fig. 5P, R) that suggests a small contribution of the supraoccipital (*c.* 4 mm) to the dorsal foramen magnum margin (Figs 4B, 5O–R). Each facet preserves the posterior semicircular canal passage laterally, more exposed on the right side due to erosion (Fig. 5M, N, P, R). An anterior projection of each lateral process (possibly a separate co-ossification, the epiotic; e.g. Sereno 1991) forms a small portion of the lateral braincase wall and a subtriangular ventral facet for the prootic, which bears the anterior semicircular canal passage and the fossa subarcuata for the floccular lobe (Fig. 5M–O, Q). The common crus (*sensu* Oelrich 1956) is a large and deep recess visible in ventral view between the prootic and otoccipital facets (Fig. 5P, R). Along the dorsal surface of the supraoccipital, a very low and faint sagittal nuchal crest develops from the bilobed nuchal shelf at the end of the ascending process until nearly the dorsal margin of the foramen magnum (Fig. 5O–Q). Lateral to the nuchal crest, the ascending process is mostly smooth. On the dorsal surface, near the bases of the parietal facets that border the ascending process, a small foramen is present on each side, probably marking the external passage of the main trunk of the vena capitis dorsalis (more distinguishable on the left side; Fig. 5R). In ventral view it is possible to see the internal foramen of that vein (more distinguishable on the left side; Fig. 5Q), which would have continued its path following the ventral margin of the parietal facet. Internally, the strongly concave surface (Fig. 5O–Q) would have enclosed the posterodorsal brain.

Remarks. GPIT-PV-122984 shows the typical triradiate shape of the supraoccipital of non-hadrosauroid ornithopods (Norman 2004), with an anterodorsally inclined posterior surface as in *Dy. lettowvorbecki* dyA/MB.R.1372 (Sobral *et al.* 2012), *Hippodraco scutodens* McDonald *et al.* 2010 and *Th. neglectus* (Boyd 2014), contrasting with the vertical orientation in *Ig. bernissartensis* (Norman 1980), '*Do. bampingi*' (Norman 1986) and *Ou. nigeriensis* (Taquet 1976). The participation in the dorsal margin of the foramen magnum is reduced for the supraoccipital of GPIT-PV-122984, as in most dryosaurids (Galton 1983; Hübner & Rauhut 2010; Dunfee 2022), *Ca. dispar* (Gilmore 1909), some rhabdodontomorphs (Chanthasit 2010; Zanno *et al.* 2023) and *Thescelosaurus* Gilmore 1913 (Boyd 2014), but unlike the majority of large iguanodontians, including hadrosaurids, in which the supraoccipital is excluded (Taquet 1976; Norman, 1980; Norman, 1986; Horner *et al.* 2004; Thomas 2015; Lockwood *et al.* 2024). The exclusionary condition was recently reported also for the specimen of *Dr. elderae* CM 87688, the latest ontogenetic stage known for the species (Carpenter & Lamanna 2015; Dunfee 2022). In many early-diverging ornithopods, the exposure of the supraoccipital on the dorsal margin of the foramen magnum is much more extensive than in GPIT-PV-122984 (e.g. Galton 1974; Avrahami *et al.* 2024; Bertozzo *et al.* 2025). The position of the openings for the semicircular canals and of the common crus matches *Dy. lettowvorbecki* dyA/MB.R.1372 (Sobral *et al.* 2012). The ascending process of GPIT-PV-122984 lacks ridges or grooves, probably correlated with the insertion of the rectus capitis posterior muscles, seen in *Co. chasei* (Lockwood *et al.* 2024) and some rhabdodontomorphs (Weishampel *et al.* 2003; Zanno *et al.* 2023). For GPIT-PV-122984, there is no flaring posterior to the ascending process or of the ventral processes, both reported for *Te. tilletti* (Thomas 2015). The low nuchal crest of GPIT-PV-122984 is similar to that in some thescelosaurids (Boyd 2014; Krumenacker *et al.* 2023; Avrahami *et al.* 2024), whereas it is notably more marked in the lectotype of *Dr. altus* YPM 1876 (Galton 1983), *Ig. bernissartensis* (Norman 1980), *Iani smithi* Zanno *et al.* 2023, *Zalmoxes robustus* (Nopcsa 1902) (Weishampel *et al.* 2003) and *Hy. Foxii* (Galton 1974). A low nuchal crest is also described for the smaller supraoccipitals of *Dy. lettowvorbecki* (BSPG AS I 834) and *Dr. elderae* (CM 11340), comparable in size and morphology to that of GPIT-PV-122984, whereas in larger individuals, as *Dy. lettowvorbecki* dyA/MB.R.1372 and *Dr. elderae* CM 3392 and CM 87688, it is much sharper (Janensch 1955; Hübner & Rauhut 2010; Sobral *et al.* 2012; Dunfee 2022). *Tenontosaurus tilletti* has a mostly flat external surface of the supraoccipital (Thomas 2015). The foramina for the main trunk of the vena capitis dorsalis of GPIT-PV-122984 resemble those reported in *Dy. lettowvorbecki* (Sobral *et al.* 2012), whereas in *Co. chasei* they are probably more dorsally located (Lockwood *et al.* 2024).

Prootic. The left prootic is almost entirely preserved, with minor damage to its posterior margins. It is a subrectangular, dorsoventrally elongated, and mediolaterally compressed bone that formed a substantial portion of the left dorsolateral braincase wall. Rugose articular facets for the surrounding elements are present (although no fusion is evident), including those for the laterosphenoid anteriorly, the parabasisphenoid ventrally, the supraoccipital dorsomedially and the otoccipital on the posterior dorsal surface. On the dorsal portion of the lateral surface, a low prootic crest, the attachment site of the musculus levator pterygoideus (as reported by Norman 2004), extends posteriorly and curves dorsally, overlapping the otoccipital and contributing to the base of the paroccipital process (Fig. 6A, D). Beneath the crest, the ventral portion is anteroposteriorly narrower and centrally pierced by a rounded and relatively large foramen (Fig. 6A, B) for the facial nerve (CN VII). On the lateral surface, the ventral border of the facial nerve foramen shows an anteroventrally defined canal for the palatine branch of CN VII (Fig. 6A), leading into the Vidian canal of the parabasisphenoid. The arcuate anterior margin of this region bounded the posterior edge of the large trigeminal foramen (CN V) (Fig. 6A, B). Given that this portion seems complete, the anterior margin of the trigeminal foramen was probably not fully formed by the prootic and was completed by the laterosphenoid anteriorly. No clear foramen for the auditory nerve (CN VIII) is visible on the medial surface, probably due to erosion or a non-ossified posteroventral border. An anteroventral projection forms the prootic contribution to the crista alaris (alternatively named processus clinoideus by some authors, e.g. Maisch & Matzke 2019) (Fig. 6A, B, E), continuous with the crista alaris of the parabasisphenoid. A depression on the lateral surface, posteroventrally to the facial nerve foramen (Fig. 6A), probably marked the attachment of musculus protractor pterygoideus (Bertozzo *et al.* 2025). The posterior surface bears a smooth ventral convexity for the lagenar recess, above which lie the large vestibule cross-sections, separated by a lagenar crest, whereas more dorsally stands the lateral semicircular canal passage (Fig. 6B, D, E). A wide ventral gap between the prootic and otoccipital would have housed the middle ear (Fig. 4A). In fact, the prootic contributed to the anterior margins of the metotic fissure and, more dorsally, the fenestra ovalis (Fig. 6A), positioned at about the same level as the trigeminal foramen and above the facial nerve foramen. Mediodorsally, the contact with the supraoccipital shows the anterior semicircular canal (Fig. 6B, F) and a depression, probably the continuation of the fossa subarcuata, bounded ventrally by a pronounced vestibular pyramid (Fig. 6B, D–F). Despite being relatively pronounced, the fossa subarcuata narrows posteriorly and does not project more anteriorly than the level of the anterior semicircular canal, probably accommodating only a small floccular lobe.

Remarks. In GPIT-PV-122984, the prootic seems to form only the posterior portion of the trigeminal foramen, as reported for most of the ornithopods (e.g. Gilmore 1909; Norman 1986; Galton 1989; Zanno *et al.* 2023; Lockwood *et al.* 2024; Bertozzo *et al.* 2025), including the early ontogenetic stages of *Dr. elderae*, such as CM 11340 (Dunfee 2022). Conversely, advanced ontogenetic stages of *Dy. lettowvorbecki* (MB.R.1370) and *Dr. elderae* (CM 3392), as also *Dr. altus* YPM 1876, have the foramen fully enclosed by the prootic (Galton 1983, 1989; Sobral *et al.* 2012; Dunfee 2022), a condition also seen in *Th. neglectus* (Boyd 2014) and *Fona herzogae* Avrahami *et al.* 2024. Hübner &

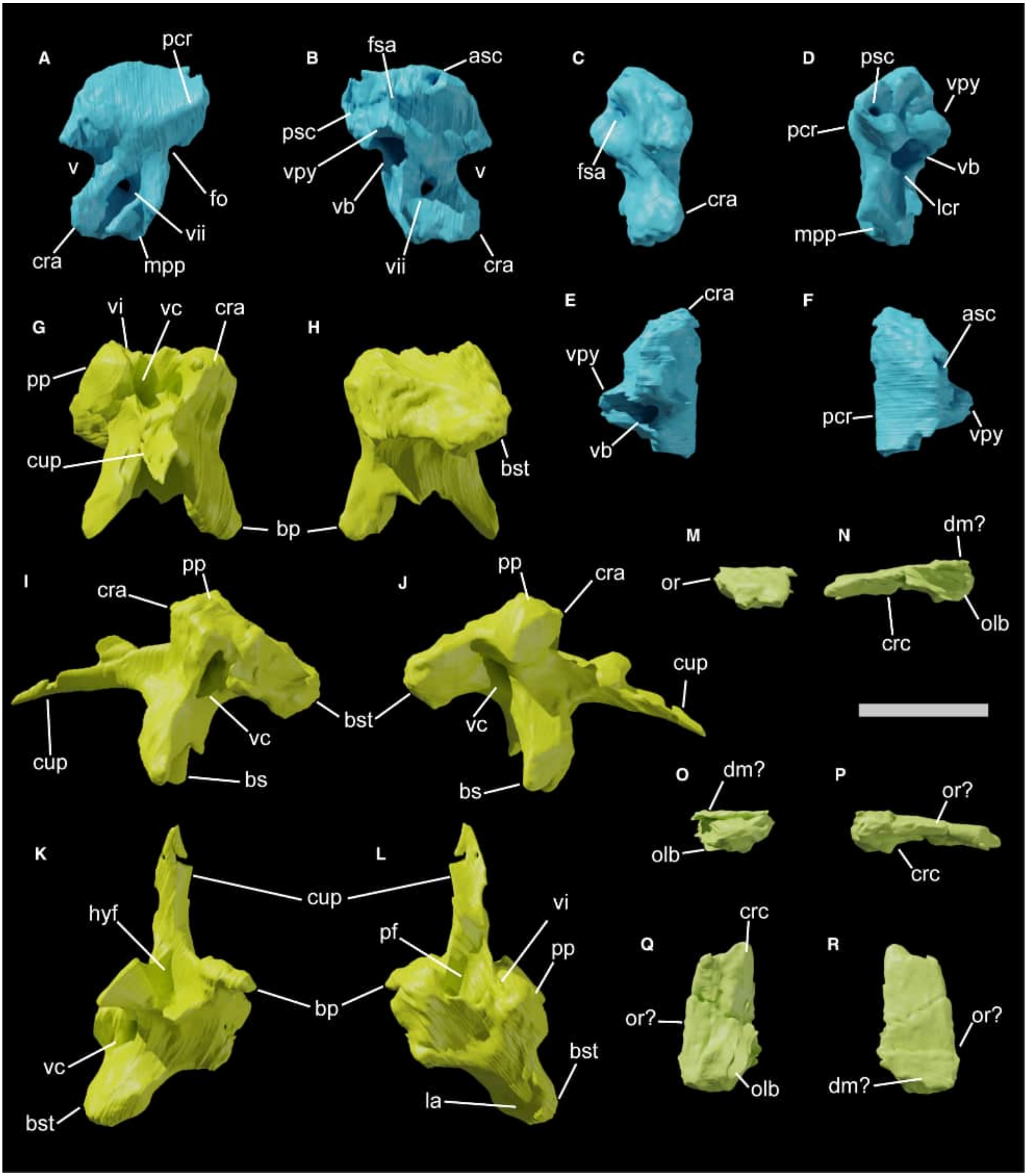

FIG. 6. Cranial skeleton of GPIT-PV-122984. A–F, prootic in: A, left lateral; B, right lateral; C, anterior; D, posterior; E, ventral; F, dorsal view. G–L, prootic in: G, anterior; H, posterior; I, left lateral; J, right lateral; K, ventral; L, dorsal view. M–R, right frontal in: M, anterior; N, medial; O, posterior; P, lateral; Q, ventral; R, dorsal view. *Abbreviations*: bp, basipterygoid process; bst, parabasisphenoid contribution to the basal tubera; cra, crista alaris; crc, crista cranii; cup, cultriform process; dm, frontal dome; fo, fenestra ovalis; fsa, fossa subarcuata; hyf, closed hypophyseal fenestra; la, lagenar recess; lcr, lagenar crest; mpp, m. protractor pterygoideus site; olb, surface for the olfactory bulb; or, orbital rim; pcr, prootic crest; pf, pituitary fossa (no sella turcica); pp, preotic pendant; psc, posterior semicircular canal; v, foramen for the trigeminal nerve; vb, vestibule; vc, Vidian canal (carotid aorta foramen); vi, notch for the abducens foramen; vpy, vestibular pyramid. Scale bar represents 10 mm.

Rauhut (2010) hypothesized that in the early ontogenetic stage *Dy. lettowvorbecki* BSPG AS I 834 may also have a fully enclosed foramen, but the matrix obscures the anterior margin, while in the small isolated *Dy. lettowvorbecki* prootic GPIT-PV-69072 the foramen is clearly fully enclosed (Appendix S1, Fig. S1.1A, B). The arrangement of the cranial nerve foramina and fenestra ovalis in GPIT-PV-122984 is similar to that described for *Dy. lettowvorbecki* MB.R.1370 and *Hy. foxii*, with the CN VII foramen more ventral than both the fenestra ovalis and the trigeminal foramen (Galton 1974; Hübner & Rauhut 2010; Sobral *et al.* 2012). In contrast, these structures are aligned in *Dr. elderae* CM 3392 (Galton 1983) and *Tenontosaurus dossi* Winkler *et al.* 1997, whereas the trigeminal foramen lies more dorsally in the large iguanodontian NHMUK R2501 (Norman 1986). The ventral margin of the CN VII foramen in GPIT-PV-122984 bears an anteroventrally directed canal, as in *Dy. lettowvorbecki* (Sobral *et al.* 2012). The marked depression on the dorsal portion of the medial surface of the prootic resembles that of *Dy. lettowvorbecki* MB.R.1370 and *Dr. elderae* CM 11340, commonly interpreted as the fossa subarcuata (e.g. Galton 1983; Norman 1986; Boyd 2014; Thomas 2015; Dunfee 2022), as adopted here. Alternatively, it has been considered part of the channel for the endolymphatic duct (Sobral *et al.* 2012) or the entrance for the 'vena cerebralis media' (Sues 1980). Similar fossae occur in *Hy. foxii* and *Te. tilletti* (Galton 1989; Thomas 2015), whereas *Th. neglectus* shows a shallower condition (Boyd 2014). The floccular lobe did not project anterior to the anterior semicircular canal, as in *Dy. lettowvorbecki* (Lautenschlager & Hübner 2013).

Parabasisphenoid. Most of the parasphenoid and basisphenoid are preserved and fused to each other to form a parabasisphenoid complex, with no distinguishable suture. The parasphenoid probably forms most of the anterior rostrum, whereas the basisphenoid contributes mostly to the main body. The parabasisphenoid was found isolated and appears to be unfused to the basioccipital antemortem. The anteroposterior length of the basisphenoid body (from its posterior margin to the base of the rostrum) is *c.* 13.5 mm, which is subequal to the basioccipital (Fig. 4A). Posteriorly, the basisphenoid forms two dorsoventrally flattened, posterolaterally elongate contributions to the basal tubera, divided medially by a notch (Fig. 6K, L). The parabasisphenoid contribution to the left basal tubera is mostly lost, whereas the right is preserved as an oblique plate, protruding posterolaterally, with a rugose ventral surface for attachment of the constrictor dorsalis musculature (Fig. 6K). Therefore, the basal tubera would have been formed by a major contribution of the parabasisphenoid and a minor one of the basioccipital. A shallow depression on the dorsal surface of the parabasisphenoid contribution to the right basal tuber is interpreted as the lagenar recess (Fig. 6L). The dorsal surface of the parabasisphenoid is gently transversely concave, forming the anterior braincase floor (Fig. 6H, L). Laterally, subrectangular inclined preotic pendants contacted the prootics (Fig. 6I, J). Anteriorly, a step defines the posteromedial walls of the pituitary fossa, and the floor of the hypophysis (Fig. 6G, K, L). On the ventral surface, a concavity separates the parabasisphenoid contributions to the basal tubera from the two anterior, strongly ventrolaterally projecting basipterygoid processes (Fig. 6G–L). Between their bases lies a deep median pit, probably marking the closed hypophyseal fenestra beneath the pituitary fossa (Fig. 6K). The posterior pit margin forms a sharp transverse wall with a pointed medial projection. Each basipterygoid process bears a thin ridge separating the posterior and anterolateral surfaces. The dorsal anterolateral surface, at the lateral corner of the main body, forms most of the crista alaris for attachment of musculus protractor pterygoideus. The ventralmost part of the anterior surface of each basipterygoid process is flat. Between this ventralmost portion of the processes and the crista alaris, on each side, a smooth concavity may indicate a venous path (Fig. 6I, J). On the dorsal posterior surface of the basipterygoid left process, a wide foramen probably transmitted the cerebral carotid artery and the palatine branch of the facial nerve (CN VII) into the Vidian canal (Fig. 6I, J). The right side is broken, exposing the canal section. Both Vidian canals extend anteromedially, with exit foramina opening on the posterolateral pituitary fossa walls (Fig. 6G, K). Directly above the exit of the Vidian canal, a small notch could represent the passage of the abducens nerve (CN VI), not fully enclosed in a canal (Fig. 6G, L). The elongated parasphenoid rostrum originates at the pituitary fossa floor, with a posterior dorsal process for the anterior restriction of the hypophysis (Fig. 6I, J). Anteriorly, it extends as a cultriform process, tapering forward with a smooth dorsal groove (Fig. 6L).

Remarks. The parabasisphenoid of GPIT-PV-122984 closely resembles dryosaurids, having an elongated, tapering parasphenoid fused to the basisphenoid, posteriorly developed basal tubera contributions, and ventrolaterally oriented basipterygoid processes (Hübner & Rauhut 2010; Sobral *et al.* 2012; Dunfee 2022). The anteroposterior length of the basisphenoid body of GPIT-PV-122984 is almost identical to the basioccipital, as in dryosaurids, *Ca. dispar* and *Hy. foxii*, whereas in *Z. robustus* and in the thescelosaurids the basisphenoid body is much shorter (Dieudonné *et al.* 2021; Avrahami *et al.* 2024). The parabasisphenoid contributions to the basal tubera of GPIT-PV-122984 form prominent posterolateral flanges, comparable to *Dy. lettowvorbecki* dyA/MB.R.1373 (Hübner & Rauhut 2010; Sobral *et al.* 2012) and to *Cu. prestwichii* (Maidment *et al.* 2022). In *Dr. elderae* advanced ontogenetic stages (CM 87688, CM 3392), the parabasisphenoid contributions to the basal tubera contributions are similar but proportionally less elongate, whereas in the early ontogenetic stage CM 11340 they are more flattened, a condition accentuated in *Ca. dispar* with tongue-shaped tubera contributions (Carpenter & Lamanna 2015; Dunfee 2022). The parabasisphenoid of GPIT-PV-122984 does not bear prominent lateral cristae tuberales or ventral ridges, unlike *Te. tilletti* (Thomas 2015) and *Ia. smithi* (Zanno *et al.* 2023). The basipterygoid processes of GPIT-PV-122984 project strongly ventrally and slightly laterally, divided by a thin ridge into posterior and anterolateral surfaces, a condition comparable to *Dy. lettowvorbecki* (BSPG AS I 834 and dyA/MB.R.1373; Hübner & Rauhut 2010; Sobral *et al.* 2012) and *Dr. elderae* (Carpenter & Lamanna 2015; Dunfee 2022). In contrast, in *Ou. nigeriensis* and *Ca. dispar*, these processes are short and project almost laterally (Taquet 1976; Carpenter & Lamanna 2015). These processes are also shorter for *Z. robustus*

(Weishampel *et al.* 2003). The deep pit between the basipterygoid processes of GPIT-PV-122984 is described for *Dy. lettowvorbecki* dyA/MB.R.1373 (Sobral *et al.* 2012), *Dr. elderae* (Dunfee 2022) and *Hy. foxii* (Galton 1974), whereas *Ca. dispar* lacks it (Carpenter & Lamanna 2015). Thescelosaurids usually have an anteroposteriorly oriented ventral groove, but no pits (e.g. Boyd 2014; Krumenacker *et al.* 2023; Avrahami *et al.* 2024). The transverse crest related to the hypophyseal pit bears a medial ventral process, comparable to *Dy. lettowvorbecki* dyA/MB.R.1373 (Sobral *et al.* 2012) and *Dr. edlerae* (Carpenter & Lamanna 2015; Dunfee 2022). The foramina of the Vidian canals lie in the usual ornithopod position (e.g. Sobral *et al.* 2012; Thomas 2015; Bertozzo *et al.* 2025). The abducens nerve in GPIT-PV-122984 probably passed through a small notch on both sides of the posterior pituitary fossa wall, a condition similar to the early ontogenetic stage of *Dr. elderae* CM 11340, whereas in the advanced stage of *Dr. elderae* CM 87688 and *Te. tilletti* a complete canal is present (Thomas 2015; Dunfee 2022). The abducens foramen was illustrated for *Dy. lettowvorbecki* dyA/MB.R.1373 by Galton (1989, pl. 1, fig. 8), but was not confirmed by Sobral *et al.* (2012). The cultriform process of GPIT-PV-122984 is elongated and bears a dorsal process, comparable to *Hy. foxii* (Galton 1974) and dryosaurids (Hübner & Rauhut 2010; Sobral *et al.* 2012; Dunfee 2022). In *Ou. nigeriensis*, *Te. tilletti* and *Ca. dispar* no dorsal process appears to be present (Taquet 1976; Thomas 2015; Carpenter & Lamanna 2015).

Frontal. A fragment of the right frontal is preserved, broken anteriorly and posteriorly. The bone is flat, subrectangular, at least twice as long anteroposteriorly as wide mediolaterally, and slightly narrower anteriorly (Fig. 6Q, R). The lateral margin may represent part of the orbital dorsal rim (Fig. 6N–R). The medial margin forms the straight and extended interfrontal suture (Fig. 6N, Q, R). The dorsal surface is smooth (Fig. 6R). On the ventral side, a sinuous low ridge (the crista cranii) separates the lateral orbital facet from the medial surface, corresponding to the position of the right olfactory bulb (Fig. 6O–Q). Posteriorly, part of a small, flat dome is preserved (Fig. 6N, O, R). The extent of the frontal contribution to the orbital dorsal rim cannot be determined.

Remarks. The frontal of GPIT-PV-122984 is subrectangular and anteroposteriorly elongated, as for dryosaurids (Janensch 1955; Hübner & Rauhut 2010; Dunfee 2022), *Ca. dispar* (Gilmore 1909) and *Iy. raathi* (Forster *et al.* 2023). This contrasts with the more quadrangular to polygonal (pentagonal/hexagonal), anteroposteriorly shorter and lateromedially wider frontals of larger iguanodontians such as *Ou. nigeriensis* (Taquet 1976), *Ig. bernissartensis* (Norman 1980), *Te. tilletti* (Thomas 2015) or *Co. chasei* (Lockwood *et al.* 2024). GPIT-PV-122984 also differs from the narrower frontal of *Hy. foxii* (Galton 1974) and *Th. neglectus* (Boyd 2014). The interfrontal suture of GPIT-PV-122984 is straight, as in *Dy. lettowvorbecki* (e.g. BSPG AS I 834, GPIT/RE/1595/17 and MB.R.1377; Hübner & Rauhut 2010), *Dr. elderae* (Dunfee 2022), *Ou. nigeriensis* (Taquet 1976) and rhabdodontids (Weishampel *et al.* 2003; Chanthasit 2010), whereas it is sinusoidal in *Co. chasei* (Lockwood *et al.* 2024). Posteriorly, the frontal bears a slightly marked, flat dome, comparable to small specimens of *Dy. lettowvorbecki* (e.g. BSPG AS I 834, GPIT/RE/1595/15, GPIT/RE/1595/17; Hübner & Rauhut 2010), *Iy. raathi* (Forster *et al.* 2023), and in skeletally immature lambeosaurines (Horner *et al.* 2004; Evans *et al.* 2007).

Indeterminate bone. A nearly V-shaped and highly distorted bone was recovered inside the block (Fig. 2D; Appendix S1, Fig. S1.2). It possibly represents the predentary or a palatal element, but its deformation does not allow a secure identification.

Inner ear. Almost the entire left endosseous labyrinth of GPIT-PV-122984 could be reconstructed (Fig. 7A), described following the nomenclature of Sobral *et al.* (2012), in turn based on Oelrich (1956). The vestibule is a large cavity between the otoccipital and prootic (Fig. 7D–J), above the metotic fissure. It measures *c.* 12.36 mm anteroposteriorly, 3.76 mm mediolaterally and 3.32 mm dorsoventrally, although its posterior tract within the prootic is not preserved. At its posterior end, within the otoccipital, there is a posterior ampullar recess that houses the termination of the posterior semicircular canal and lies close to the posterior end of the lateral semicircular canal. The lateral semicircular canal extends for *c.* 11.15 mm along the prootic crest (Fig. 7D–J), running from the otoccipital into the prootic, where it ends forming a lateral ampullar recess, close to the anterior ampullar recess of the anterior semicircular canal end. The posterior end of the lateral semicircular canal lies slightly more dorsally than the anterior one. The anterior semicircular canal, *c.* 12.6 mm long, exits the prootic anteriorly at its dorsomedial contact with the supraoccipital (Fig. 7H–J), then extends dorsally into the anterior expansion of the supraoccipital (‘epiotic’), bending ventrally to converge with the posterior canal in the common crus (Fig. 7B, C). The common crus probably extended out of the supraoccipital into the dorsal otic capsule to rejoin the vestibule. The posterior canal describes an arcuate path of *c.* 11.48 mm, descending from the common crus, entering the otoccipital on its dorsomedial surface, and ending in the posterior ampullar recess (Fig. 7B–G). The anterior semicircular canal is taller than the posterior one (Fig. 7A). On the ventral surface of the posterior prootic a depression for the lagenar recess is visible (Fig. 6D), extending into the parabasisphenoid, marked dorsally by a shallow depression on the contribution to the basal tuber (visible on the right side; Fig. 6F). This recess probably housed the perilymphatic cistern laterally and the cochlear duct medially. The cochlea measures at least 8.01 mm in length, estimated from the distance between the lagenar crest and the ventral contact of the prootic with the parabasisphenoid.

Remarks. Given that the braincase elements of GPIT-PV-122984 were found disarticulated, the measurements on the inner ear structures are an approximation based on the reconstructed morphology of the area. The semicircular canals appear to be of comparable length, as in *Dy. lettowvorbecki* dyA (including MB.R.1370 and MB.R.1372) and BSPG AS I 834 (Sobral *et al.* 2012; Lautenschlanger & Hübner 2013), whereas in *Iguanodon* Mantell 1825 the lateral canal is proportionally shorter than

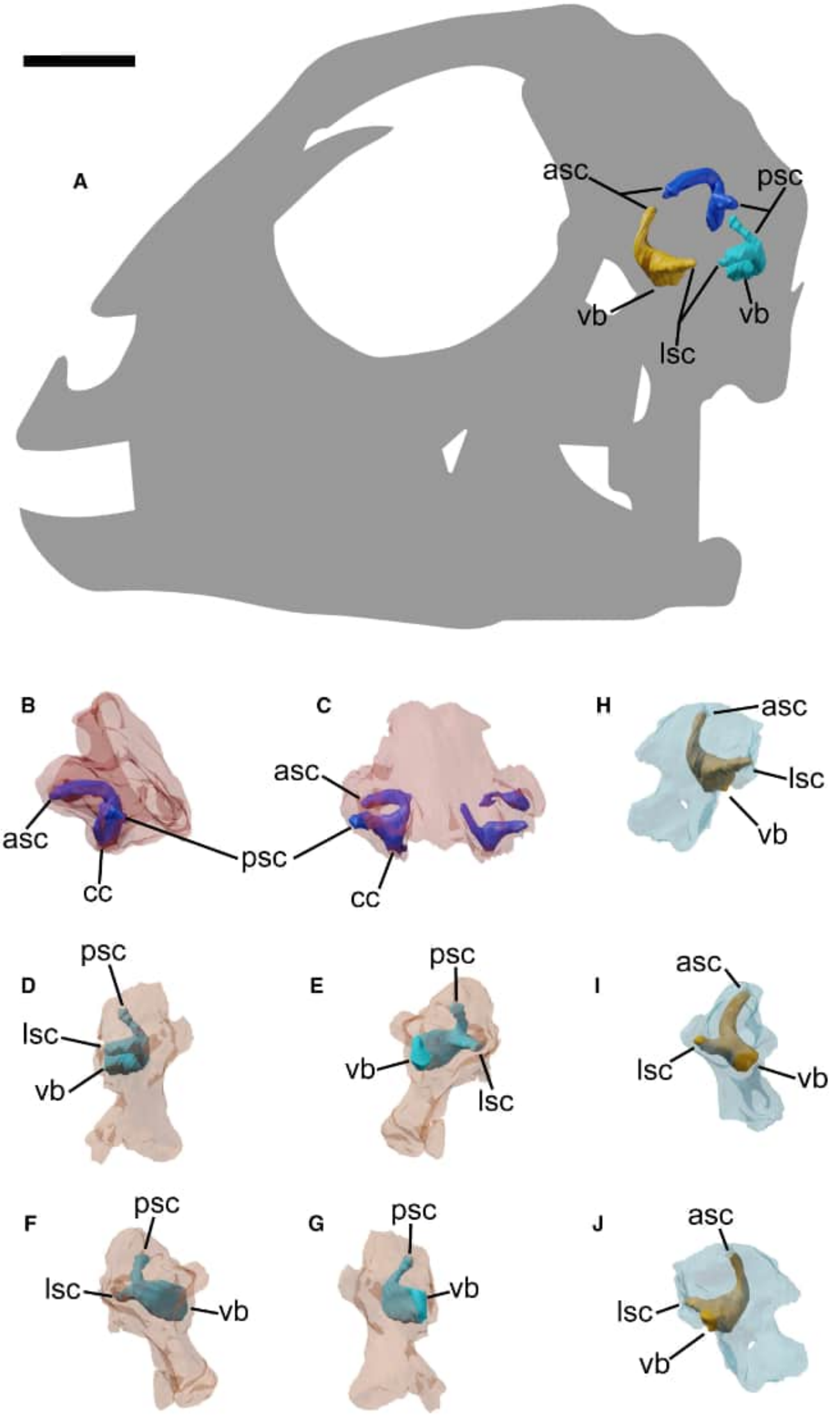

FIG. 7. Inner ear of GPIT-PV-122984. A, inferred position of the semicircular canal in left lateral view. B–C, semicircular canals of the supraoccipital in: B, left lateral; C, posterior view. D–G, semicircular canals of the otoccipital in: D, lateral, E, posterior; F, anterior; G, medial view. H–J, semicircular canals of the prootic in: H, lateral, I, posterior; J, medial view. *Abbreviations*: asc, anterior semicircular canal; cc, common crus; lsc, lateral semicircular canal; psc, posterior semicircular canal; vb, vestibule. Silhouette modified from Lautenschlanger & Hübner (2013). Scale bar represents 10 mm.

the other two (Norman 2004, fig. 19.9). The anterior semicircular canal is taller than the posterior semicircular canal, as reported for various ornithopods (Sobral *et al.* 2012; Thomas 2015; Cruzado-Caballero *et al.* 2015). The lateral canal shows a dorsoventral inclination, as in *Dy. lettowvorbecki* dyA/MB.R.1370 (Sobral *et al.* 2012; Lautenschlanger & Hübner 2013) and *Th. neglectus* (Button & Zanno 2023), whereas in other ornithopods it lies more subhorizontally (e.g. Farke *et al.* 2013; Cruzado-Caballero *et al.* 2015; Thomas 2015). The cochlea seems to be dorsoventrally elongated as in other ornithopods (Sobral *et al.* 2012; Norman 2004).

Axial skeleton

The cervical series, lacking only the atlas and axis, and the first two dorsal vertebrae were found semi-articulated, in opisthotonic posture (Figs 6B, D, 8A). Two additional dorsal vertebrae were recovered as disarticulated elements.

Cervical vertebrae. Seven post-axial cervical vertebrae (Cv3–9) are preserved. Cervicals are here defined as the vertebrae with at least part of the parapophysis ventral to the neurocentral suture, as in Norman (1980, 1986) and Forster (1990). Cv5–9 are preserved in articulation in the block (Fig. 6B, D), whereas Cv4 lies disarticulated but closely associated, positioned immediately anterior to Cv5. An isolated neural arch, found near Cv4, is referred to Cv3 based on morphology, and a cervical centrum found immediately anterior to Cv4 is interpreted as the corresponding centrum of Cv3, given its size and fit with the arch (Fig. 8A–I). Because Cv9 remains articulated posteriorly with the first dorsal vertebra, the specimen can be confidently interpreted as possessing nine cervical vertebrae in total, including the missing atlas and axis (Fig. 8A). The post-axial cervical vertebrae are only weakly opisthocoelous to plano-concave. The posterior articular surface of the centra is gently concave (Figs 8F, L, R, 9C, I, O, U), whereas the anterior surface is planar to slightly convex (Figs 8D, J, P, 9A, G, M, S). Cv5 shows an apparent ventral protrusion of the anterior articular surface (Fig. 8Q, S), but this is probably the result of taphonomic deformation. Similar deformation is evident in Cv4 and Cv9 (Figs 8J, L, 9S, U). The dorsal margin of the anterior articular surface is slightly everted, a feature especially clear in Cv9 (Fig. 9T, V). All cervical centra are anteroposteriorly longer than dorsoventrally tall. This is exaggerated in Cv3 (Fig. 8E, G), which shows an anteroposterior length (on the ventral surface) to dorsoventral height (on the anterior surface) ratio of 1.84. The ratio decreases posteriorly, ranging between 1.38 and 1.61 in Cv4–6 (Figs 8K, M, Q, S, 9B, D) and 1.25–1.34 in Cv7–9 (Fig. 9H, J, N, P, T, V). Thus, anterior cervical centra (Cv3–5) are proportionally longer than the posterior ones (Cv6–9), with Cv7 the shortest. In lateral view, the Cv3 centrum is dorsoventrally taller posteriorly than anteriorly, whereas the other centra have a straighter or slightly ventrally convex ventral margin, shaped by a low keel present in Cv4–9 (Figs 8O, U, 9F, L, R, X). Cv3 also bears a keel, although reduced (Fig. 8I). In ventral view, centra are hourglass shaped, with anterior parapophyses laterally wider than the posterior margin. Therefore, in lateral view, shallow ventrolateral depressions extend on each side ventrally to a low ridge, which terminates anteriorly in the subtriangular, laterally projecting parapophysis (Figs 8I, O, U, 9F, L, R, X). On both lateral surfaces, the parapophyses form a continuous curve with the lateral portion of the anterior articular surface of the centrum. Parapophyses are relatively small in the anterior centra (especially Cv4) but develop progressively larger facets posteriorly. In Cv3 a single vascular foramen for the anterior spinal artery (also named as foramen venosum by Witzmann *et al.* 2008) lies between the unfused neurocentral synchondroses (Fig. 8B), a condition also visible on the pedicles of its neural arch (Fig. 8C), indicating a low degree of fusion (Brochu 1996; Ikejiri 2012). In Cv4–9, neurocentral sutures remain variably visible (see Sutural Closure in the ontogenetic stage assessment section below). These sutures pass dorsally to the parapophyses in Cv3–7, but divide the parapophyses in Cv8–9. Each neural arch encloses a subcircular neural canal with thin walls and bears the diapophyses, prezygapophyses and postzygapophyses. Cv3 bears short, pointed, ventrolaterally directed diapophyses (Fig. 8D, F, H, I). In Cv4 the diapophyses are weakly developed, possibly reduced to a ridge continuous with the prezygapophysis (Fig. 8M), although erosion may account for their poor preservation. In Cv5–9 the diapophyses are convex facets located on the distal tip of transverse processes that protrude on each side of the neural arch (Figs 8P, R, 9A, C, G, I, M, O, S, U). The transverse processes change shape along the series, from short, hooked projections in Cv5 (Fig. 8P, R) to elongate posterolateral processes in Cv9 (Fig. 9S, U). The transverse process is incompletely preserved in several vertebrae, with the left missing in Cv6 and the right broken distally in Cv5 and Cv7–9. Prezygapophyses vary along the series: Cv3 bears stout, anterodorsally directed prezygapophyses (Fig. 8E, G, H); in Cv4 they are slenderer, elongated, anterolaterally oriented processes (Fig. 8K, M, N); Cv5–9 have reduced prezygapophyses, with medially facing triangular facets positioned at the anterior base of the transverse processes (Figs 8Q, S–T, 9A, E, G, K, M, Q, S, W). The prezygapophyses migrate progressively laterally from Cv5 to Cv9. The postzygapophyses are two posterolaterally elongated processes at the posterior margin of the neural roof. In Cv3, the postzygapophyses are twisted and bifid distally (Fig. 8E, G, H), diverging posteriorly to the level of the posterior articular surface of the centrum. In Cv4, the postzygapophyses diverge from an elongate posteriorly directed stalk almost at the level of the posterior articular surface, although the left side is damaged (Fig. 8N). Cv5 has two separate, elongate postzygapophyses diverging at the posterior articular surface level (Fig. 8T). In Cv6–9 the divergence occurs anterior to the posterior articular surface (Fig. 9E, K, Q, W). The length of the postzygapophyses increases from Cv4 to Cv6, then decreases towards Cv9. At the end of each postzygapophysis, facets face ventrolaterally for articulation with the prezygapophyses of the succeeding vertebra. Cv9 bears a deep postspinal fossa at the junction of the postzygapophyses, immediately above the neural canal (Fig. 9U); similar fossae may have been present in Cv6–8, although damage occurred. The neural spine is virtually absent in Cv3–5, leaving a smooth roof profile (Fig. 9E, G, K, M, Q, S). A short, hook-like neural spine appears in Cv6–9, increasing in height posteriorly (Fig. 9B, D, H, J, N, P, T, V). Each spine arises immediately anterior to the divergence of the postzygapophyses and is connected to them by the spinopostzygapophyseal laminae.

Remarks. The cervical vertebrae count of nine, as recorded in GPIT-PV-122984, is consistent with several non-styracosternan iguanodontians (Norman 2004), including *Dy. lettowvorbecki*

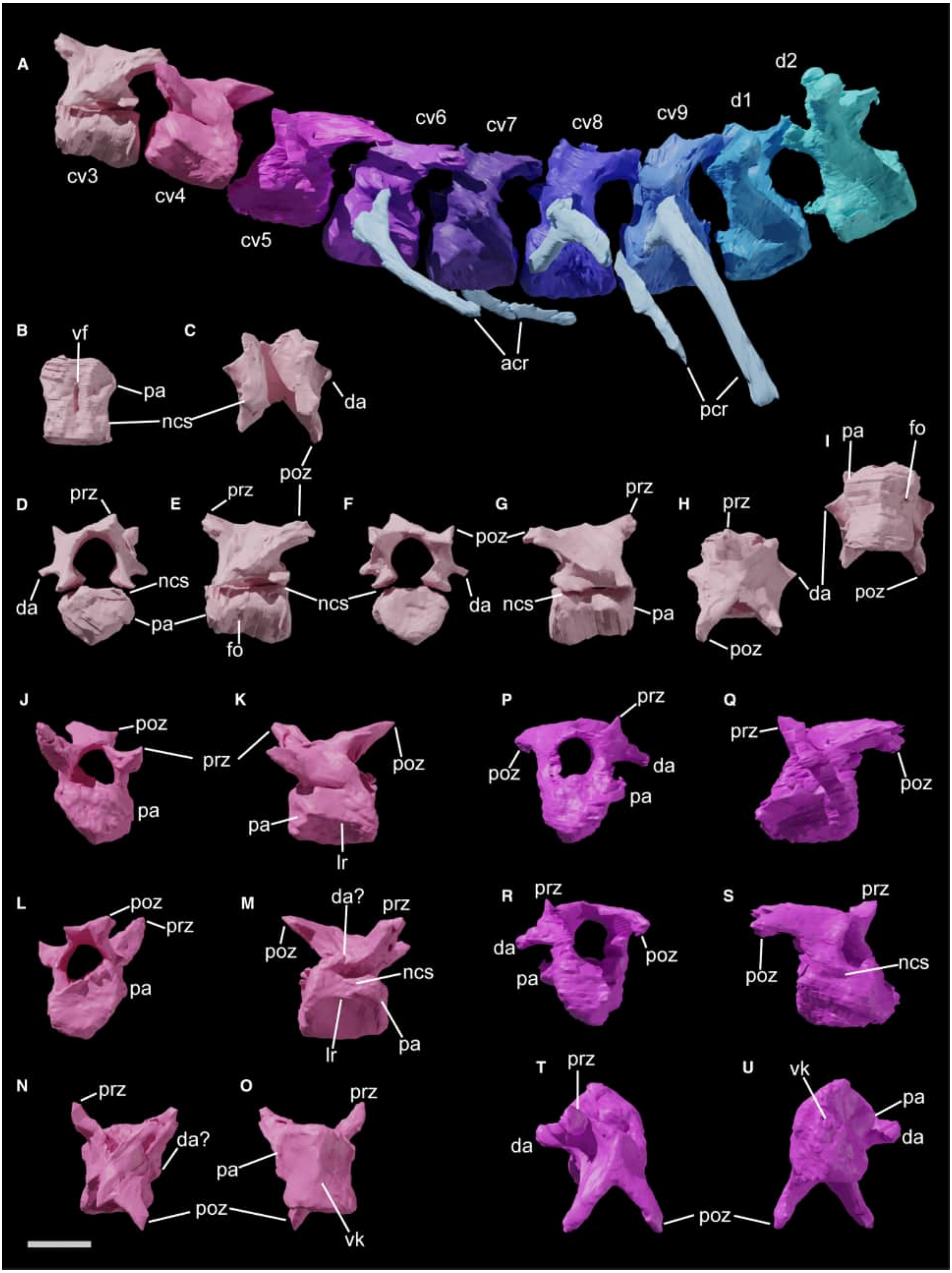
A
cv3
cv4
cv5
cv6
cv7
cv8
cv9
d1
d2
acr
pcr
B
vf
pa
ncs
C
da
poz
D
prz
da
ncs
pa
E
prz
fo
F
ncs
da
G
poz
prz
ncs
pa
H
prz
poz
I
pa
fo
da
poz
J
poz
prz
pa
K
poz
pa
lr
P
prz
poz
da
pa
Q
prz
poz
L
poz
prz
pa
M
da?
prz
poz
ncs
lr
pa
R
prz
da
pa
poz
S
prz
poz
ncs
N
prz
da?
poz
O
prz
pa
vk
T
prz
da
U
vk
pa
da
poz

FIG. 8. Anterior cervical vertebral series of GPIT-PV-122984. A, preserved cervical and first two dorsal vertebrae mounted in anatomical position. B, neural arch of Cv3 in ventral view. C, centrum of Cv3 in dorsal view. D–I, reconstructed Cv3 appearance in: D, anterior; E, left lateral; F, posterior; G, right lateral; H, dorsal; I, ventral view. J–O, Cv4 in: J, anterior; K, left lateral; L, posterior; M, right lateral; N, dorsal; O, ventral view. P–U, Cv5 in: P, anterior; Q, left lateral; R, posterior; S, right lateral; T, dorsal; U, ventral view. *Abbreviations*: acr, anterior cervical rib; cv3–9, cervical vertebrae 3–9; da, diapophysis; fo, nutritional foramen; lr, lateral ridge; ncs, neurocentral suture or synchondrosis; pa, parapophysis; pcr, posterior cervical rib; poz, postzygapophysis; prz, prezygapophysis; vf, vascular foramen; vk, ventral keel. Scale bar represents 10 mm.

(Galton 1981; Hübner 2018), *Ca. dispar* (Gilmore 1909) and *U. aphanoecetes* (Carpenter & Wilson 2008). A similar number is also reported in the non-iguanodontian ornithopods *Hy. foxii* (Galton 1974) and *Talenkauen santacrucensis* Novas *et al.* 2004 (Rozadilla *et al.* 2019). By contrast, most non-hadrosaurid styracosternans usually possess 10–11 cervicals (e.g. Norman 1980, 1986, 2004; Bertozzo *et al.* 2017), and *Te. tilletti* has 12 (Forster 1990). Janensch (1955) described only eight cervicals in *Dy. lettowvorbecki*, based on the mounted specimen ‘dyI’ at the MB. However, Pompeckj (1920), in his preliminary account of now mostly lost material, suggested the presence of nine vertebrae. This higher count was subsequently adopted by Galton (1981) and Hübner (2018), who hypothesized that Cv9 was missing in dyI, a condition more consistent with other ornithopods. As previously noted, the distinction between cervical and dorsal vertebrae is commonly based on the position of the parapophyses relative to the neurocentral suture/synchondrosis. However, as stressed by Lockwood *et al.* (2024), this criterion is somewhat arbitrary and may have introduced artificial differences in vertebral counts across ornithopods. The cervical centra of GPIT-PV-122984 are slightly opisthocoelous to planoconcave, as reported for some dryosaurids (Galton 2009; Carpenter & Lamanna 2015), *Ca. dispar* (Gilmore 1909), *Cu. prestwichii* (Maidment *et al.* 2022), rhabdodontids (Weishampel *et al.* 2003; Chanthasit 2010) and *Te. tilletti* (Forster 1990). In contrast, *V. canaliculatus* and large non-hadrosaurid styracosternans possess strongly opisthocoelous cervical vertebrae (Norman, 1980, 1986, 2002; Barrett *et al.* 2011; Bertozzo *et al.* 2017; Bonsor *et al.* 2023), whereas *U. aphanoecetes* has amphiplatyan middle and posterior cervical vertebrae (Carpenter & Wilson 2008). No notochordal pits are visible on the anterior articular surfaces, in contrast to *Ig. bernissartensis* (Norman 1980) and *Mantellisaurus atherfieldensis* (Hooley 1925) (Bonsor *et al.* 2023). In GPIT-PV-122984, the cervical centra are consistently longer anteroposteriorly than tall dorsoventrally, as reported for *Dy. lettowvorbecki* dyI (Janensch 1955), *Iy. raathi* (Forster *et al.* 2023), *Ca. dispar* (Gilmore 1909), *Cu. prestwichii* (Maidment *et al.* 2022), *Co. chasei* (Lockwood *et al.* 2024) and *Te. tilletti* (Forster 1990). However, centra are not as elongate as in *V. canaliculatus* and *Ta. santacrucensis*, in which the length is more than double the dorsoventral height (Barrett *et al.* 2011; Rozadilla *et al.* 2019). Conversely, the cervical centra are proportionally taller than long in *Ig. bernissartensis* (Norman 1980), *M. atherfieldensis* (Bonsor *et al.* 2023) and *Zalmoxes shqiperorum* Weishampel *et al.* 2003. The ventral margin of the post-axial cervical centra of GPIT-PV-122984 is nearly straight, resembling that of *Dy. lettowvorbecki* dyI (Janensch 1955, pl. 12, figs 5–9), *U. aphanoecetes* (Carpenter & Wilson 2008) and *M. atherfieldensis* (Bonsor *et al.* 2023), whereas it is concave in *Ig. bernissartensis* (Norman 1980) and *Te. tilletti* (Forster 1990). None of the cervical vertebrae of GPIT-PV-122984 has the wedge-shaped ventral margin of Cv8 described for *U. aphanoecetes* (Carpenter & Wilson 2008). A ventral keel is present in GPIT-PV-122984, as in *Dy. lettowvorbecki* dyI (Janensch 1955), *Dr. altus* (Shepherd *et al.* 1977), styracosternans (e.g. Taquet 1976; Norman 1980; Bonsor *et al.* 2023), and many other non-hadrosaurid ornithopods (e.g. Galton 1974; Forster 1990; Carpenter & Wilson 2008; Chanthasit 2010; Barrett *et al.* 2011; Forster *et al.* 2023). *Thescelosaurus neglectus* reportedly lacks a keel and has a ventrally flattened centrum (Gilmore 1915). In GPIT-PV-122984 the parapophyses form a continuous curve with the anterior articular surface of the centrum, as in *Dy. lettowvorbecki* dyI (Janensch 1955) and *Dryosaurus* (Galton 1981). Conversely, in *Ca. dispar* (Gilmore 1909; Carpenter & Wilson 2008, fig. 7) and *M. atherfieldensis* (Bonsor *et al.* 2023) they are positioned more posteriorly, whereas in *Hy. foxii* they form a marked angle with the articular surface (Galton 1981). The cervical neural arches of GPIT-PV-122984 enclose a subcircular neural canal, proportionally similar to those of *Dy. lettowvorbecki* dyI (Janensch 1955, pl. 12, figs 5–9) and *Dr. altus* (Carpenter & Galton 2018), whereas in *Dr. elderae* (Carpenter & Galton 2018) the canal is lower dorsoventrally and longer anteroposteriorly. Cv3 of GPIT-PV-122984 lacks the median crest posterior to the prezygapophyses described for *Ca. dispar* (Gilmore 1909). Epipophyses are also absent in GPIT-PV-122984, in contrast to some rhabdodontomorphs (Weishampel *et al.* 2003; Chanthasit 2010; Zanno *et al.* 2023) and *Ta. santacrucensis* (Rozadilla *et al.* 2019). A small but distinct neural spine is present on Cv5–9 of GPIT-PV-122984, resembling the condition of *Dy. lettowvorbecki* dyI (Janensch 1955) and other dryosaurids (Shepherd *et al.* 1977; Barrett *et al.* 2011), but also *Co. chasei* (Lockwood *et al.* 2024), *Z. robustus* (Weishampel *et al.* 2003) and *Hy. foxii* (Galton 1974). In *Te. tilletti* the spines are more prominent (Forster 1990, fig. 1), whereas in *Ca. dispar* they are nearly absent (Gilmore 1909; Carpenter & Wilson 2008).

Cervical ribs. Four cervical ribs were found in the block (Figs 3, 8A). Two of them, a left and a right one, probably belonged to the anterior portion of the series, given that their shafts extend posteroventrally, gently curving backward and downward from the centrum articulation, and remain approximately parallel to the anteroposterior axis. The other two left ribs were associated with more posterior cervical vertebrae because they have a shaft that curves almost vertically from the centrum articulation. In the two anterior cervical ribs, the tuberculum is longer than the

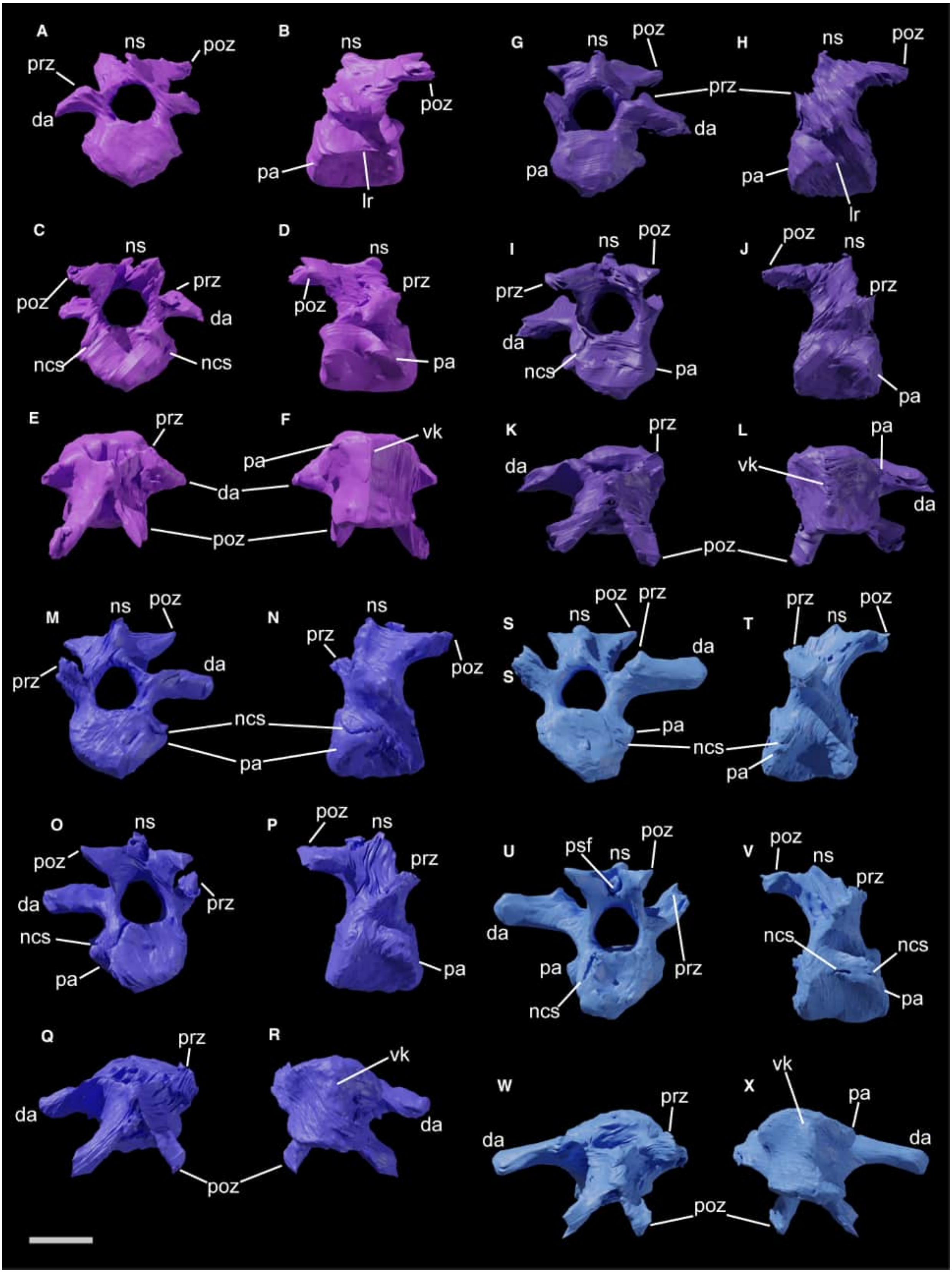
A
ns
poz
prz
da
B
ns
poz
pa
lr
G
ns
poz
prz
da
pa
H
ns
poz
pa
lr
C
ns
prz
poz
da
ncs
ncs
D
ns
prz
poz
pa
I
ns
poz
prz
da
ncs
pa
J
poz
ns
prz
pa
E
prz
da
poz
F
vk
pa
K
prz
da
poz
L
pa
vk
da
M
ns
poz
prz
da
ncs
pa
N
ns
prz
poz
S
poz
prz
ns
da
S
pa
ncs
T
prz
ns
poz
pa
O
ns
poz
da
prz
ncs
pa
P
poz
ns
prz
pa
U
psf
ns
poz
da
pa
prz
ncs
V
poz
ns
prz
ncs
ncs
pa
Q
prz
da
poz
R
vk
da
W
prz
da
poz
X
vk
pa
da

FIG. 9. Anterior cervical vertebral series of GPIT-PV-122984. A–F, Cv6 in: A, anterior; B, left lateral; C, posterior; D, right lateral; E, dorsal; F, ventral view. G–L, Cv7 in: G, anterior; H, left lateral; I, posterior; J, right lateral; K, dorsal; L, ventral view. M–R, Cv8 in: M, anterior; N, left lateral; O, posterior; P, right lateral; Q, dorsal; R, ventral view. S–X, Cv9 in: S, anterior; T, left lateral; U, posterior; V, right lateral; W, dorsal; X, ventral view. *Abbreviations*: da, diapophysis; lr, lateral ridge; ncs, neurocentral suture or synchondrosis; ns, neural spine; pa, parapophysis; poz, postzygapophysis; prz, prezygapophysis; psf, postspinal fossa; vk, ventral keel. Scale bar represents 10 mm.

---

capitulum, which instead is stouter. Conversely, in the posterior ribs, the tuberculum is short yet robust, whereas the capitulum is distinctly elongated. A low ridge projects posteriorly from the dorsal margin of the shaft in the posterior cervical ribs.

Dorsal vertebrae. The 10th and the 11th presacral vertebrae were found in articulation with Cv9 (Fig. 2B, D; 8A) and, given that their parapophyses lie above the neurocentral suture, they were identified as the first two dorsals (D1 and D2), following Norman (1980, 1986) and Forster (1990). D1 bears transitional features between cervical and dorsal vertebrae. Two additional dorsal vertebrae were found isolated, with their neural arches detached from their centra but still associated, named from now on as Da and Db (Fig. 2B, D). They represent anterior to middle dorsals, posterior to D2: spatial arrangement inside the block and the morphology suggest that Da belonged to the D3–5 range, with Db slightly more posterior (Fig. 8A). The centra of D1 and D2 are deformed by compression. D1 has a flat anterior and a slightly concave posterior articular surface, whereas D2 is gently concave on both ends (Fig. 10A, D, G, J). Da and Db have amphicoelous centra with more pronounced concavity (Fig. 11A, D, I, L). In D1–D2, the dorsal margins of the anterior surfaces are slightly everted, as in the cervical series (Fig. 10B, E, H, K). All dorsal centra are longer than tall (length/height ratio between 1.70 and 1.31). D1 and D2 bear a prominent ventral keel, probably accentuated by deformation (Fig. 10F, L), whereas Da and Db have smoother keels and more rounded ventral aspects (Fig. 11F, N). Ventrolateral depressions formed by an anteroposterior concavity at the mid-length of the centra give D1 and D2 an hourglass outline in ventral view. This mid-length constriction is instead nearly absent in Da and Db. The neurocentral suture remains visible in Da and Db (see Sutural Closure in the ontogenetic stage assessment section below). In Da and Db, the detached centra expose a median vascular foramen dorsally, flanked by irregular neurocentral synchondrosial surfaces that would have articulated with the neural arch pedicles (Fig. 11G, H, O, P). Parapophyses are consistently positioned on the neural arch. In D1 they are small, dorsoventrally elongated facets at the anterior base of the transverse processes (Fig. 10B, E). In D2 they are set more dorsally, at the level of the prezygapophyses, forming a small anterolateral knob (Fig. 10H, K, L). In Da and Db this parapophysis knob is more squared, situated above the prezygapophyses, and more prominent in Db (Fig. 11B, C, E, F, J, K, N). The transverse processes are stout, with distal ends broken in D1, D2 and Db, exposing a subtriangular cross-section with a ventral apex (Fig. 10E, K). The transverse processes orientation in dorsal view shifts from posterolateral in D1 (Fig. 10C, F) to more laterally directed in D2, Da and Db (Figs 10I, L, 11C, F, K, N). In anterior view the transverse processes are only slightly dorsally inclined in D1 and D2 (Fig. 10A, D, G, J), while in the more posterior Da and Db the processes are markedly laterodorsally directed (Fig. 11A, D, I, L). Robustness of the transverse processes also increases posteriorly. D2, Da and Db show a series of laminae (*sensu* Wilson 1999): a posterior centrodiapophyseal lamina extends from the ventral surface of the transverse process to the centrum; a centropostzygapophyseal lamina extends from the pedicle to the ventral margin of the postzygapophyses; and a postzygodiapophyseal lamina develops from the posterior margin of the transverse process to the anterior margin of the postzygapophysis. Together, these laminae delimit a posterior triangular depression, shallow in D2 but deeper in Da and Db (Figs 10J, L, 11D, F, L, N). In D1 these laminae and the depression are only weakly developed (Fig. 10D, F). Prezygapophyses originate from the dorsal surface of the transverse process base. They are small in D1 (Fig. 10B, C, E), larger and anteriorly expanded in D2 (Fig. 10H, I, K), mostly broken in Da (Fig. 11E), and in Db modified into two anterodorsally directed sheets positioned at *c.* 45° to the horizontal (Fig. 11J, K, M). In dorsal view it is possible to define a lateral constriction at the base of the prezygapophysis of D2 and Db (Figs 10I, 11K). The prezygapophyses facets consistently face dorsomedially. Postzygapophyses consistently change through the series: D1 retains elongated, posterolaterally directed processes similar to posterior cervicals (Fig. 10B, C, E); D2 has shorter, subhorizontal projections (Fig. 10H, J, K); whereas Da and Db preserve only reduced, subhorizontal posterior projections, partially broken (Fig. 11B, C, E, J, M, N). As in Cv9, a postspinal fossa is present between the postzygapophyses of D1 and D2 (Fig. 10D, J), while it is not recognizable in Da and Db. The point of divergence between the postzygapophyses of D1 and D2 is anterior to the level of the posterior centrum surface, whereas the postzygapophyses in Da and Db diverge posteriorly to the level of the posterior centrum surface. Each postzygapophysis has a ventrolaterally facing facet, inclined at *c.* 45° to the horizontal. In D1 the neural spine, although relatively tall, retains a more similar morphology to the posterior cervicals (Fig. 10B, E) than to the more posterior dorsals. In contrast, the spine of D2 is considerably taller, blade-like, and marked by an anteroposterior constriction just below the tip (Fig. 10H, I). The base of the neural spine of D1 is dorsoventrally inclined in lateral view, whereas it is subhorizontal in D2. In Da, the neural spine is eroded near its base (Fig. 11A, D), whereas in Db the dorsal portion is damaged but still preserved as a taller element than the spine of D2 (Fig. 11I, L). The base of the neural spine of Da and Db is subhorizontal, located on a broad platform that forms the roof of the neural canal. In D2 a deep fossa separates the prezygapophyses from the

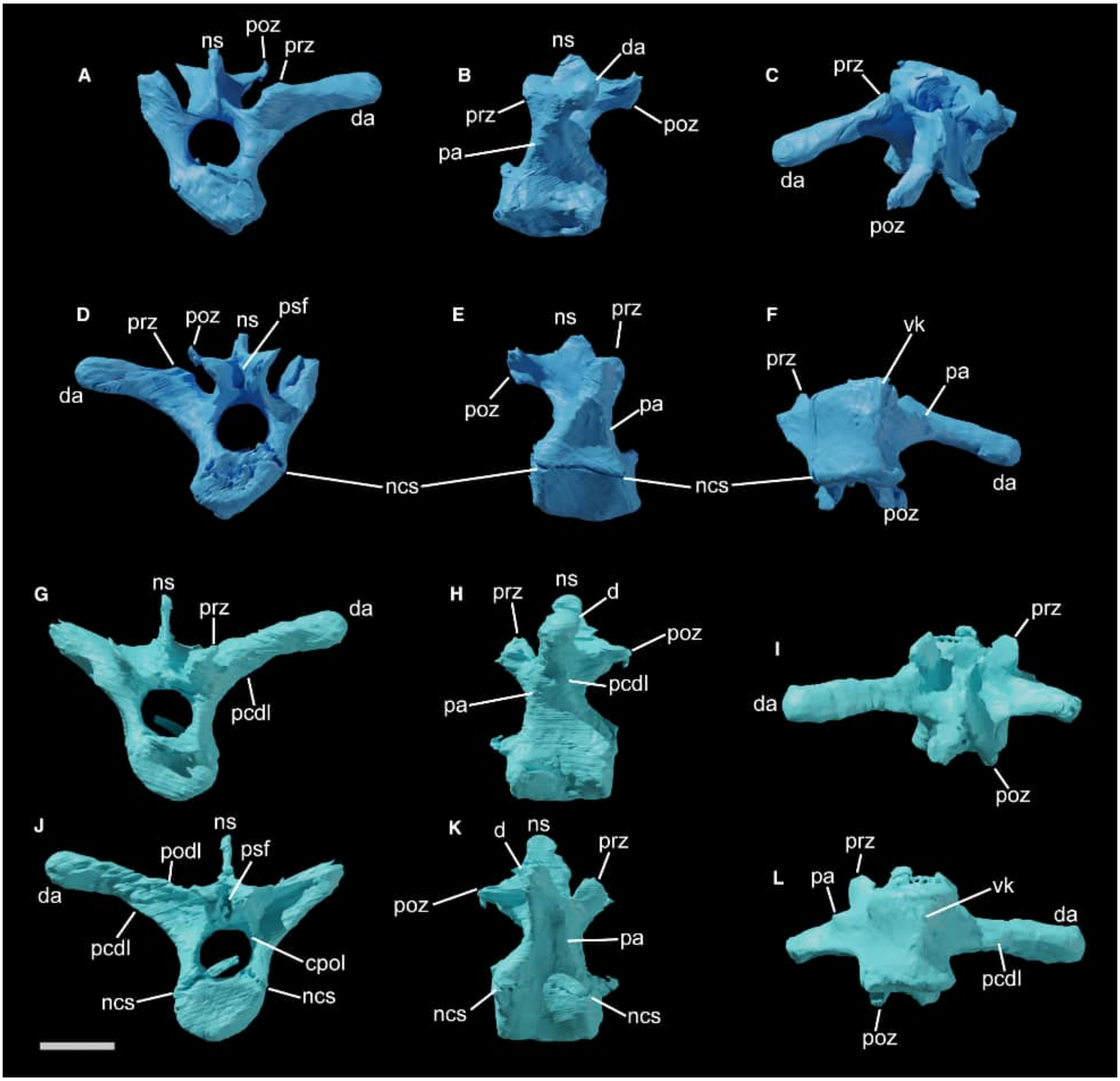

FIG. 10. Anterior dorsal vertebral series of GPIT-PV-122984. A–F, D1 in: A, anterior; B, left lateral; C, dorsal; D, posterior; E, right lateral; F, ventral view. G–L, D2 in: G, anterior; H, left lateral; I, dorsal; J, posterior; K, right lateral; L, ventral view. *Abbreviations*: cpol, centropostzygapophyseal lamina; da, diapophysis; ncs, neurocentral suture or synchondrosis; ns, neural spine; pa, parapophysis; pcdl, posterior centrodiapophyseal lamina; podl, postzygodiapophyseal lamina; poz, postzygapophysis; prz, prezygapophysis; psf, postspinal fossa; vk, ventral keel. Scale bar represents 10 mm.

FIG. 11. Isolated dorsal vertebrae of GPIT-PV-122984. A–F, reconstructed appearance of Da in: A, anterior; B, left lateral; C, dorsal; D, posterior; E, right lateral; F, ventral view. G, Da centrum in dorsal view. H, Da neural arch in ventral view. I–N, reconstructed appearance of Db in: I, anterior; J, left lateral; K, dorsal; L, posterior; M, right lateral; N, ventral view. O, Db centrum in dorsal view. P, Db neural arch in ventral view. *Abbreviations*: cpol, centropostzygapophyseal lamina; da, diapophysis; ncs, neurocentral suture or synchondrosis; ns, neural spine; pa, parapophysis; pcdl, posterior centrodiapophyseal lamina; podl, postzygodiapophyseal lamina; poz, postzygapophysis; prz, prezygapophysis; vf, vascular foramen. Scale bar represents 10 mm.

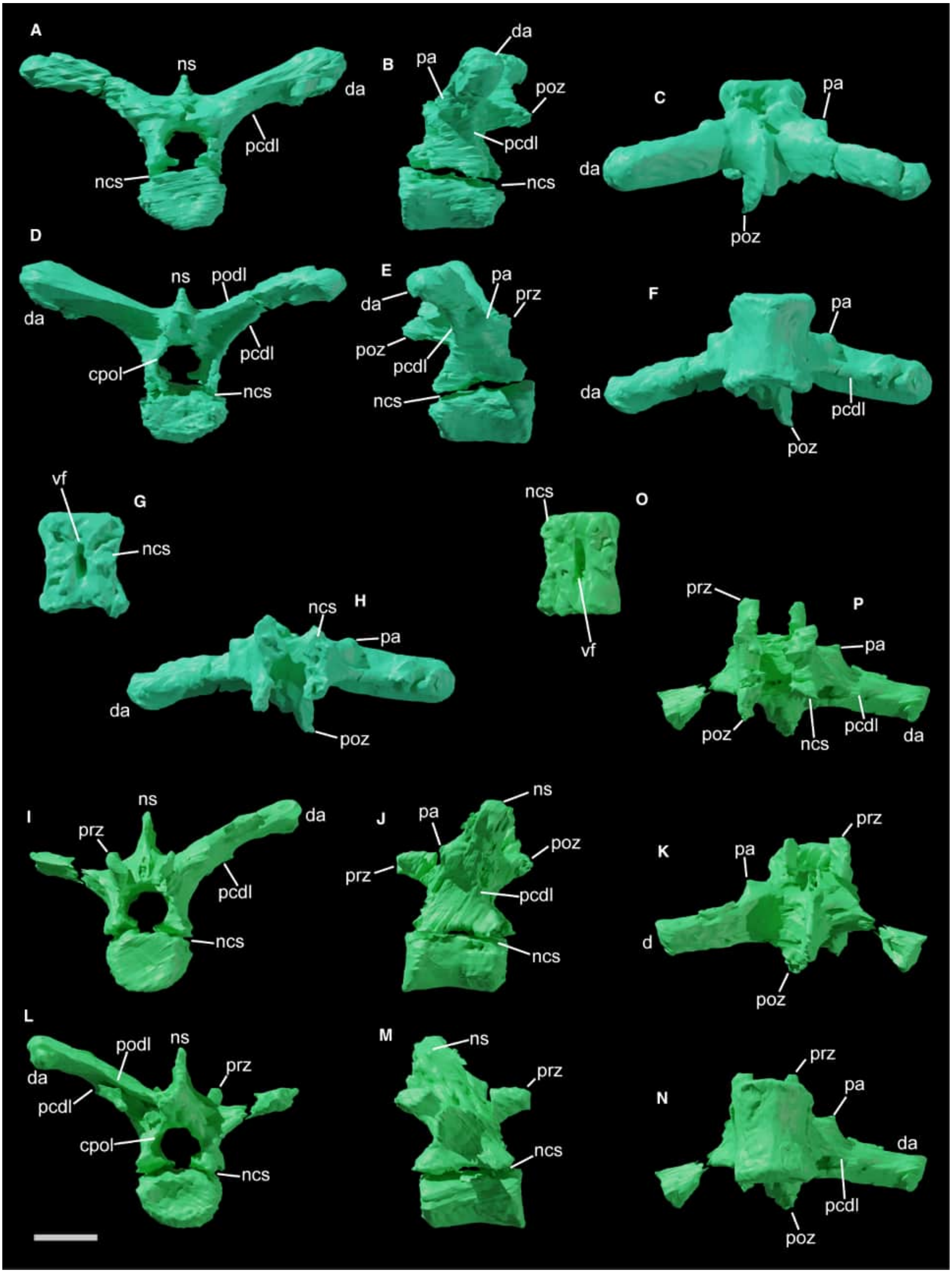
A
ns
da
pcdl
ncs
B
da
pa
poz
pcdl
ncs
C
pa
da
poz
D
ns
podl
da
pcdl
cpol
ncs
E
da
pa
prz
poz
pcdl
ncs
F
pa
da
pcdl
poz
vf
G
ncs
ncs
H
pa
da
poz
ncs
O
vf
prz
P
pa
poz
ncs
pcdl
da
I
ns
da
prz
pcdl
ncs
J
pa
ns
poz
prz
pcdl
ncs
K
prz
pa
d
poz
L
podl
ns
prz
da
pcdl
cpol
ncs
M
ns
prz
ncs
N
prz
pa
da
pcdl
poz

neural spine (Fig. 10I), whereas the same structure is shallower in Da and Db (Fig. 11C, K).

Remarks. In GPIT-PV-122984, D1 exhibits transitional features between cervical and dorsal vertebrae, as in most iguanodontians (Norman 2004). The centrum of D1 is less markedly opisthocoelous and anteriorly convex than the first dorsal vertebrae of *V. canaliculatus* (Barrett *et al.* 2011) or some styracosternans (e.g. Norman 1980, 1986; Bertozzo *et al.* 2017). The centra posterior to D1 of GPIT-PV-122984 have gently concave articular surfaces, resembling *Dy. lettowvorbecki* (dyI and dyII/MB.R.1586; Janensch 1955), other iguanodontians (e.g. Gilmore 1909; Carpenter & Wilson 2008; Bonsor *et al.* 2023), and thescelosaurids (e.g. Gilmore 1915; Avrahami *et al.* 2024). D1 and D2 centra of GPIT-PV-122984 are anteroposteriorly longer than dorsoventrally tall, as in *Dy. lettowvorbecki* (dyI and dyII/MB.R.1586; Janensch 1955; Hübner *et al.* 2021, fig. 12A), *Dr. altus* (Galton 1981, fig. 1C, E), *Ou. nigeriensis* (Bertozzo *et al.* 2017), and some thescelosaurids (Gilmore 1915; Krumenacker *et al.* 2023), contrasting with the nearly subequal proportions of *Ig. bernissartensis* (Norman 1980), *Brighstoneus simmondsi* Lockwood *et al.* 2021 and rhabdodontomorphs (Weishampel *et al.* 2003; Godefroit *et al.* 2009; Zanno *et al.* 2023). A ventral keel is present on the anterior dorsal centra of GPIT-PV-122984, diminishing posteriorly, as in *Dy. lettowvorbecki* dyI (Janensch 1955), *Ca. dispar* (Gilmore 1909), *Probactrosaurus gobiensis* Rozhdestvensky 1966 (Norman 2002), *Te. tilletti* (Forster 1990) and some thescelosaurids (e.g. Scheetz 1999; Krumenacker *et al.* 2023; Avrahami *et al.* 2024). In contrast, no keel occurs in *Cu. prestwichii* (Maidment *et al.* 2022), whereas in many styracosternans it persists posteriorly (Norman 1980; Bertozzo *et al.* 2017; Bonsor *et al.* 2023; Lockwood *et al.* 2024). The parapophyses of D1 in GPIT-PV-122984 are distinct in position, size and shape from those of the preceding cervicals, as in *Dy. lettowvorbecki* dyI (Janensch 1955). D1 parapophyses are reduced, unlike the enlarged condition in *Ca. dispar* (Gilmore 1909). The parapophyses follow the typical iguanodontian migration: dorsally onto the neural arch and laterally along the transverse process (Norman 2004). Posterior to D1, the transverse processes show a posterior depression bounded by laminae, as in *Dy. lettowvorbecki* (dy27/MB.R.1486; Janensch 1955), *V. canaliculatus* (Barrett *et al.* 2011), but also, for example, *Cu. prestwichii* (Maidment *et al.* 2022), *Co. chasei* (Lockwood *et al.* 2024), *Ia. smithi* (Zanno *et al.* 2023), *J. shangyuanensis* (Han *et al.* 2012) and *F. herzogae* (Avrahami *et al.* 2024). The prezygapophyses of D2 and Db have a basal lateral constriction, comparable to *Dy. lettowvorbecki* dyI (Janensch 1955, pl. 12, figs 17–20; Galton 1981, fig. 2K) and a Portuguese dryosaurid (Rotatori *et al.* 2020). The neural spine of D2 of GPIT-PV-122984 is apically constricted anteroposteriorly, possibly due to taphonomy, but a similar morphology occurs in *Dy. lettowvorbecki* dyI (Janensch 1955, pl. 12, figs 12, 13). The neural arches of the anterior dorsal vertebrae of GPIT-PV-122984 are dorsoventrally low, increasing in height posteriorly, as in many iguanodontians (Norman 2004). Their neural spines are relatively reduced compared with the transverse processes, as in dryosaurids (Galton 1981, fig. 1C–F; Carpenter & Galton 2018, fig. 29K–N), *Ca. dispar* (Gilmore 1909, fig. 15; Carpenter & Galton 2018, fig. 22D) and *Cu. prestwichii* (Maidment *et al.* 2022). In contrast, *Ig. bernissartensis*, *B. simmondsi* and some rhabdodontids show reduced transverse processes relative to neural spines (Norman 1980; Weishampel *et al.* 2003; Chanthasit 2010; Lockwood *et al.* 2021).

Dorsal ribs. Three dorsal rib fragments are preserved (Fig. 3). Two represent distal shaft segments of anterior to central dorsal ribs. Another fragment, probably from an anterior to central right dorsal rib, bears a stout tuberculum as a short dorsal projection anterior to the capitular process, which forms the proximal end of the fragment. The capitular process is elongated but broken medially. That third fragment has a prominent ridge that extends posteriorly from the dorsal margin, immediately distal to the tuberculum.

Chevrons. Two associated chevrons are preserved. Both are relatively slender and dorsoventrally short, although one is notably smaller and interpreted as the first chevron, the larger as an anterior chevron (Fig. 3). The first is broken distally, whereas the larger is nearly complete. In lateral view, both have subparallel margins with only slight proximal and distal expansion. The larger chevron is gently posteriorly arched. In anterior view, each chevron consists of two blade-like sheets of bone converging distally and connected dorsally by a transverse bridge that would have articulated between adjacent caudal vertebrae.

Remarks. The first chevron of GPIT-PV-122984 is notably small as observed in *Dy. lettowvorbecki* (dyI/MB.R.1586 in Janensch 1955, pl. 13, fig. 12). This feature is listed by Galton (1981) to distinguish *Dy. lettowvorbecki* from *Dr. altus*, which in contrast has a strong first chevron.

Appendicular skeleton

Scapula. For description, the long axis of the scapula was oriented anteroposteriorly. The anterior portion of the left scapula is preserved, whereas most of the posterodorsal blade is broken. A crack divides the bone into anterior and posterior segments. The element flares anteriorly into its articular end (Fig. 12A, B). The upper portion of this end bears the articular surface for the coracoid, which terminates anterodorsally, below the protruding acromion process. The ventral part of the articular end instead contributes to the border of the glenoid fossa (Fig. 12A–C). The medial surface of the scapula is gently mediolaterally concave and smooth, except for the canal for the supracoracoid foramen near the coracoid facet (Fig. 12A). In contrast, laterally, two marked depressions are present at the anterior end: the extensive deltoid fossa, dorsally delimited by a faint and dorsoventrally narrow deltoid ridge that rises into the acromion process at *c.* 20° to the long axis (Fig. 12B, C); and the smaller but deeper supraglenoid fossa, situated near the ventral corner of the anterior end of the scapula. The supraglenoid fossa is posteriorly delimited by the marked, anteroventrally directed, scapular labrum (ventral buttress of some authors) (Fig. 12B). Posterior to the acromion process, the dorsal margin of the

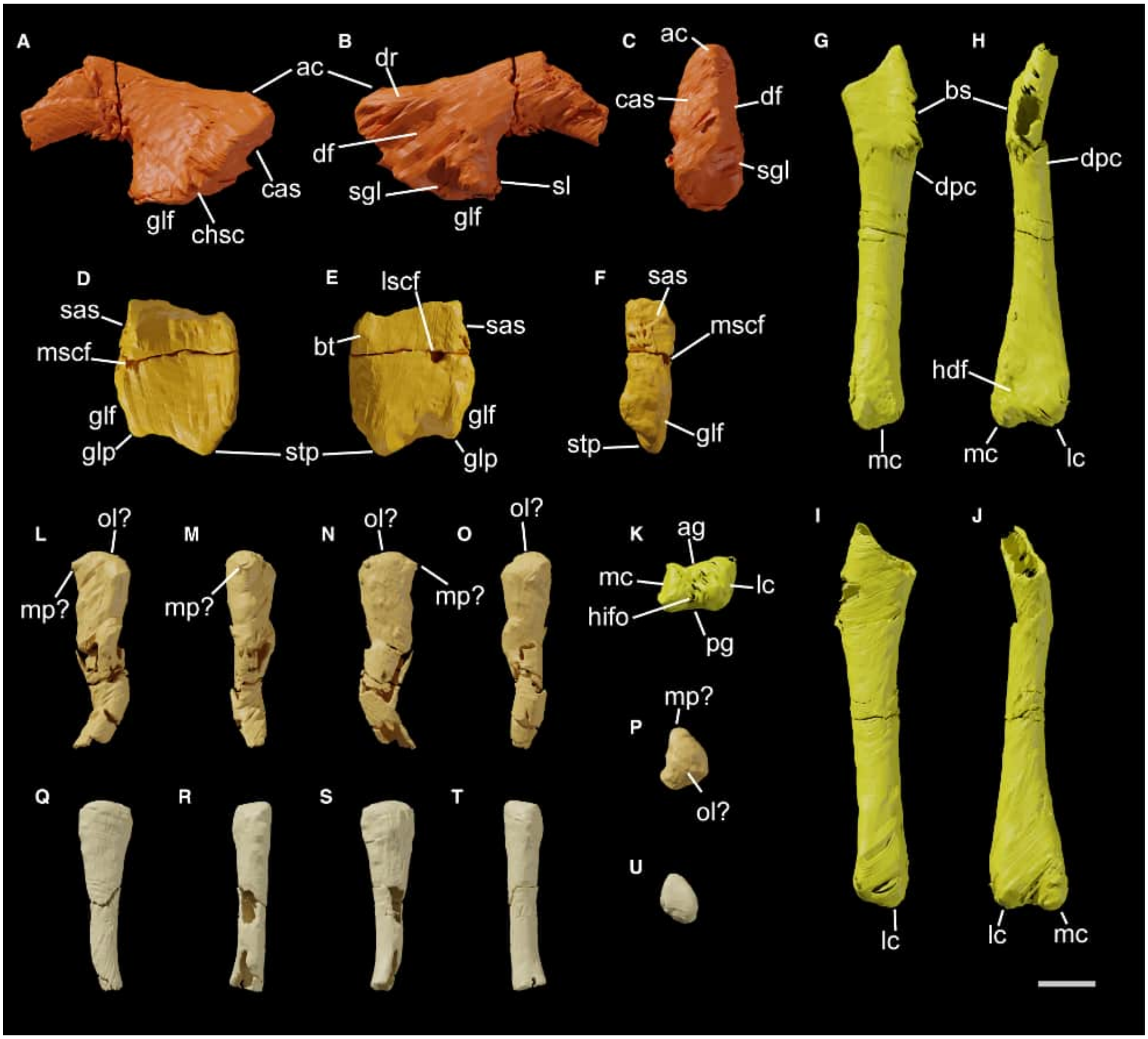

FIG. 12. Forelimb skeleton of GPIT-PV-122984. A–C, left scapula in: A, medial; B, lateral; C, anterior view. D–F, left coracoid in: D, medial; E, lateral; F, dorsal view. G–K, left humerus in: G, medial; H, anterior; I, lateral; J, posterior; K, proximal view. L–P, right ulna in: L, medial; M, anterior; N, lateral; O, posterior; P, proximal view. Q–U, left radius in: Q, medial; R, anterior, S, lateral; T, posterior; U, proximal view. *Abbreviations*: ac, acromion process; ag, anterior groove, bs, bicipital sulcus; bt, biceps tubercle; cas, coracoid articular surface; df, deltoid fossa; dpc, deltopectoral crest; dr, deltoid ridge; glp, glenoid process of the coracoid; glf, glenoid fossa; hdf, humerus distal fossa; hifo, humeral intercondilar foramen; lc, lateral radial condyle of humerus; lscf, lateral opening of supracoracoid foramen; mc, medial ulnar condyle of humerus; mp, medial process of ulna; mscf, medial opening of supracoracoid foramen; pg, posterior groove; sas, scapular articular surface; sgl, supraglenoid fossa; sl, scapular labrum; stp, sternal process. Scale bar represents 10 mm.

preserved scapula is nearly straight, whereas the posteroventral margin is bowed and lacks a distinct bulge at the shaft base (Fig. 12A, B).

Remarks. The acromion process of GPIT-PV-122984 lacks the prominent dorsal or hooked projection seen in *Ca. dispar*, *U. aphanoecetes* (Carpenter & Wilson 2008), *Ig. bernissartensis* (Norman 1980), *P. gobiensis* (Norman 2002), *Rhabdodon priscus* Matheron 1869 (Chanthasit 2010), *Ta. santacrucensis* (Rozadilla *et al.* 2019), *M. atherfieldensis* (Bonsor *et al.* 2023) and *Oryctodromeus cubicularis* Varricchio *et al.* 2007 (Krumenacker *et al.* 2023). Instead, the acromion process of GPIT-PV-122984 is a modest anterodorsal projection, comparable to that of *Dy. lettowvorbecki* (e.g. dyI, MB.R.5090, GZG.V.6287, GPI-T/RE/5330; Janensch 1955, fig. 31; Hübner 2018, text-fig. 3A–C) and *Dryosaurus* (Carpenter & Galton 2018, fig. 30C, D), but more developed than in *Te. tilletti* (Forster 1990). A canal for the supracoracoid foramen, similar to that of GPIT-PV-122984, occurs in several ankylopollexians (e.g. Gilmore 1909; Norman 1980, 1986; Bonsor *et al.* 2023; Lockwood *et al.* 2024), *Hy. foxii* (Galton 1974), but also in *Dy. lettowvorbecki* MB.R.5090 (Hübner 2018, text-fig. 3A). The narrow deltoid ridge of GPIT-PV-122984 resembles that of *Dy. lettowvorbecki* (e.g. dyI, GZG.V.6287, GPIT/RE/5330; Janensch 1955, fig. 31; Hübner 2018, text-fig. 3B, C) and most *F. herzogae* specimens (Avrahami *et al.* 2024). A sharper but still narrow ridge occurs in *Dryosaurus* (Shepherd *et al.* 1977, fig. 2A; Carpenter & Galton 2018, fig. 30C, D), *Ca. dispar* (Gilmore 1909), *U. aphanoecetes* (Carpenter & Wilson 2008), *Ou. nigeriensis* (Bertozzo *et al.* 2017) and *Th. neglectus* (Gilmore 1915). In contrast, *M. atherfieldensis* (Bonsor *et al.* 2023) and *Te. tilletti* (Forster 1990) possess a wide, rounded deltoid ridge. The supraglenoid fossa of GPIT-PV-122984 is small but distinct, as in *Dy. lettowvorbecki* (e.g. dyI, MB.R.5090, GZG.V.6287, GPIT/RE/5330; Janensch 1955, fig. 31; Hübner 2018, text-fig. 3A–C), *Dr. elderae* (Carpenter & Galton 2018, fig. 30D), *Iy. raathi* (Forster *et al.* 2023), *U. aphanoecetes* (Carpenter & Wilson 2008) and *Cu. prestwichii* (Maidment *et al.* 2022). Shallower fossae are found in *Ca. dispar* (Carpenter & Wilson 2008; McDonald 2011) and *M. atherfieldensis* (Bonsor *et al.* 2023), whereas such a fossa is reduced or absent in '*Do. bampingi*' (Norman 1986), *Hi. scutodens* (McDonald *et al.* 2010), *Co. chasei* (Lockwood *et al.* 2024), *Te. tilletti* (Forster 1990), and rhabdodontomorphs (Weishampel *et al.* 2003; Chanthasit 2010; Zanno *et al.* 2023). *Iguanodon bernissartensis* RBINS R51 clearly bears a supraglenoid fossa, despite some contrary reports (e.g. Bonsor *et al.* 2023; Lockwood *et al.* 2024).

Coracoid. For description, the long axis of the coracoid was oriented dorsoventrally. The left coracoid is preserved except for its dorsalmost portion. Even if broken anteriorly, the coracoid is already dorsoventrally taller than anteroposteriorly long (Fig. 12D, E). The bone is almost flat, with a medial concavity and a lateral weak convexity. On the lateral surface, immediately anterior to the undulating posterior margin, lies a well-marked supracoracoid foramen (Fig. 12E), fully enclosed by the coracoid, opening into a posteromedially directed canal. Immediately dorsally to this foramen, a fracture runs from the anterior to the posterior margin of the bone (Fig. 12D, E). Near the anterodorsal corner of the lateral preserved surface there is a faint biceps tubercle (*sensu* Prieto-Márquez 2011) (Fig. 12E). The bone is mediolaterally thinner in its anterior portion, thickening in its posterior part, where it forms the scapular articular surface dorsally and part of the glenoid fossa margin ventrally (Fig. 12D–F). In posterior view the articular surface for the scapula is irregular, but it lacks well-marked ridges. At the ventromedial corner of this articular surface (immediately ventrally to the fracture), the medial opening of the supracoracoid foramen is visible (Fig. 12D, F), for the passage of the supracoracoid neurovascular canal. Laterally, the glenoid fossa margin forms a rounded ridge that terminates ventrally in a rounded glenoid process (Fig. 12D, E). The scapula and coracoid contribute subequally to the dorsoventral length of the glenoid margin (*c.* 15 mm each), although the scapular margin is transversely wider (*c.* 11.5 mm) than that of the coracoid (*c.* 8 mm). On the ventral margin, the glenoid process is separated from the more ventral and subtriangular sternal process by an embayment that is anteroposteriorly wider than dorsoventrally deep (Fig. 12D, E).

Remarks. In GPIT-PV-122984, the lateral opening of the supracoracoid foramen is fully enclosed within the coracoid, as in most iguanodontians, except for some species (Norman 2004), but medially, in GPIT-PV-122984 the supracoracoid canal opens on the ventromedial corner of the posterior scapular contact surface. This condition of the medial opening is also reported for *Dy. lettowvorbecki* MB.R.1485 (Hübner 2018, text-fig. 5B), *Ou. nigeriensis* (Taquet 1976), '*Do. bampingi*' (Norman 1986) and *Ta. santacrucensis* (Rozadilla *et al.* 2019), differing from the more anteriorly located openings of this foramen in *Co. chasei* (Lockwood *et al.* 2024), *Te. tilletti* (Forster 1990), rhabdodontids (Weishampel *et al.* 2003; Chanthasit 2010), *Hy. foxii* (Galton 1974), most thescelosaurids (Scheetz 1999; Krumenacker *et al.* 2023; Avrahami *et al.* 2024), and possibly *V. canaliculatus* (based on the dubious IWCMS 2007·4 in Barrett *et al.* 2011). In *Ca. dispar*, *Ig. bernissartensis* and *Cu. prestwichii* the openings of the foramen are positioned on the articular surface both laterally and medially (Gilmore 1909; Norman 1980; Maidment *et al.* 2022) and without forming the posteromedially inclined canal seen in GPIT-PV-122984, *Ou. nigeriensis*, '*Do. bampingi*', *Ta. santacrucensis* and probably *Dy. lettowvorbecki* MB.R.1485. A faint biceps tubercle, as in GPIT-PV-122984, occurs in *Ca. dispar* (Gilmore 1909), *Ig. bernissartensis* (Norman 1980), *M. atherfieldensis* (Bonsor *et al.* 2023), and in *Dy. lettowvorbecki* MB.R.1485 and MB.R.3474 (Hübner 2018, text-fig. 5A, C), but appears absent in *Dryosaurus*, *Ta. santacrucensis* and *Th. neglectus* (Poole 2022). The glenoid process of GPIT-PV-122984 does not develop a robust pedicle, unlike the condition possibly reported for *V. canaliculatus* (based on IWCMS 2007·4, reported in Barrett *et al.* 2011). A distinct sternal process is present in GPIT-PV-122984, as in all iguanodontians (Norman 2004), but it is much reduced when compared with the hooked morphology of *Te. tilletti* (Forster 1990), *Hy. foxii* (Galton 1974), various ankylopollexians (e.g. Norman 1980; Carpenter & Wilson 2008; Maidment *et al.* 2022; Bonsor *et al.* 2023; Lockwood *et al.* 2024), *Z. shqiperorum* (Weishampel *et al.* 2003), *R. priscus* (Chanthasit 2010) and thescelosaurids (e.g. Gilmore 1915; Krumenacker *et al.* 2023; Avrahami *et al.* 2024). A similar weak, subtriangular process is documented for *Dy. lettowvorbecki* (e.g. dyI, MB.R.1485, MB.R.3474, MB.R.1476, SMNSoN2, GPIT/RE/3871; Janensch 1955, fig. 23; Hübner 2018, text-fig. 5A, C–F).

Humerus. The left humerus is preserved but lacks its proximal portion, including the head (Fig. 12G–J). In anterior view, a major fracture separates and displaces the uppermost preserved fragment, whereas additional smaller fractures occur along the slender diaphysis. The uppermost fragment bears a shallow depression for the bicipital sulcus (Fig. 12G), which originally faced anteromedially, indicating a slight torsion to the shaft. Lateral to the sulcus, a low, rounded deltopectoral crest extends from the broken dorsal margin onto the diaphysis (Fig. 12G, H), enabling reconstruction of the position of the dorsalmost fragment. Originally, the crest was restricted to the anterolateral surface of the humerus and was not visible in posterior view. The distal epiphysis is complete, with a medial ulnar condyle and a lateral radial condyle (Fig. 12H, J, K). The medial condyle projects more ventrally (Fig. 12H, J), but the lateral condyle is broader anteroposteriorly and mediolaterally (Fig. 12K). The lateral margin of the medial condyle is slightly eroded. The condyles are separated anteriorly and posteriorly by shallow grooves of similar depth: the anterior groove expands into a shallow fossa on the distal anterior surface, whereas the posterior groove is pierced by a foramen (Fig. 12K).

Remarks. The humerus of GPIT-PV-122984 is characterized by a slender diaphysis and a very low deltopectoral crest restricted to the anterior surface, a condition reported for *Dy. lettowvorbecki*, *Dr. altus* (Galton 1981), *Ta. santacrucensis* (Rozadilla *et al.* 2019), *Iy. raathi* (Forster *et al.* 2023), *Cu. prestwichii* (Maidment *et al.* 2022) and *Or. cubicularis* (Krumenacker *et al.* 2023). In contrast, the crest forms a more prominent projection in *Ca. dispar* (Gilmore 1909; Carpenter & Wilson 2008), *M. atherfieldensis* (Bonsor *et al.* 2023), rhabdodontids (Weishampel *et al.* 2003; Chanthasit 2010), *Hy. foxii* (Galton 1974), *J. shangyuanensis* (Han *et al.* 2012) and *Th. neglectus* (Gilmore 1915). *Uteodon aphanoecetes* has a rounded but distinctly developed deltopectoral crest (Carpenter & Wilson 2008). In *Ig. bernissartensis*, '*Do. bampingi*', *Hi. scutodens* and *Te. tilletti* this crest also protrudes laterally (Norman 1980, 1986; Forster 1990; McDonald *et al.* 2010; Bonsor *et al.* 2023). GPIT-PV-122984 has a lateral condyle that is mediolaterally and anteroposteriorly wider than the medial condyle, as consistently demonstrated in *Dy. lettowvorbecki* (e.g. dyI, SMNSoN3, SMNSoN2; Janensch 1955, fig. 34d; Hübner 2018, text-fig. 7E–F, table 9.2.3) and described for *Ou. nigeriensis* (Taquet 1976). In contrast, the condyles are subequal in *Dr. altus* YPM 1876 (Galton 1981), *M. atherfieldensis* (Bonsor *et al.* 2023) and *Or. cubicularis* (Krumenacker *et al.* 2023), whereas the medial condyle is wider in *Iy. raathi* (Forster *et al.* 2023), *P. gobiensis* (Norman 2002), rhabdodontids (Weishampel *et al.* 2003; Chanthasit 2010) and *J. shangyuanensis* (Han *et al.* 2012). On the anterior surface, the distal fossa of GPIT-PV-122984 is shallow, as in dryosaurids (Janensch 1955; Galton 1981; Hübner 2018, text-fig. 7B, D) and *Cu. prestwichii* (Maidment *et al.* 2022), whereas it forms a deeper distal fossa in *Ca. dispar* (Gilmore 1909), *Ig. bernissartensis* (Norman 1980), *M. atherfieldensis* (Bonsor *et al.* 2023) and *Te. tilletti* (Forster 1990). The medial condyle of GPIT-PV-122984 lacks a distinct supinator ridge, unlike the condition of *Ou. nigeriensis* (Bertozzo *et al.* 2017), *Cu. prestwichii* (Maidment *et al.* 2022) and *M. atherfieldensis* (Bonsor *et al.* 2023). In fact, apart from slight erosion, it closely resembles the medial condyle of *Dy. lettowvorbecki* SMNSoN2 (Hübner 2018, text-fig. 7E). The intercondylar foramen of GPIT-PV-122984 is also recorded for *Dryosaurus* CM 21786 (Shepherd *et al.* 1977).

Ulna. For description, the element long axis was oriented dorsoventrally. A fragmentary long bone is interpreted as the right ulna. It preserves the proximal epiphysis and part of the diaphysis, whereas the distal portion is missing. In dorsal view, the proximal end is subtriangular in outline due to the presence of two angular processes (Fig. 12P). The olecranon is not clearly recognizable, probably due to erosion (Fig. 12L, N, O). The most prominent proximal projection is tentatively identified as the medial process of the ulna, which is connected to the posteromedial angle by a concave medial margin (Fig. 12L, M, O). This concavity continues distally along the medial surface of the bone (Fig. 12L). The preserved shaft, although heavily fractured and distorted, tapers distally (Fig. 12L–O).

Remarks. Although erosion may have affected its preservation, the proximal end of the ulna of GPIT-PV-122984 does not appear to develop a prominent lateral process, similarly to *Dy. lettowvorbecki* GPIT/RE/3909 and GPIT/RE/3451 (Hübner 2018, text-fig. 6C, D), and *Dr. altus* YPM 187 (Galton 1981, fig. 7H). In contrast, a more pronounced lateral process is reported in some ankylopollexians, such as *U. aphanoecetes* (Carpenter & Wilson 2008) and *M. atherfieldensis* (Bonsor *et al.* 2023).

Radius. For description, the element long axis was oriented dorsoventrally. A slender and elongated bone, found in close association with the left humerus, is tentatively interpreted as the left radius. The element appears to preserve the proximal end and most of the diaphysis, whereas the distal end is broken. The proximal articular surface is slightly D shaped in cross-section (Fig. 12U), with a flatter medial margin and a gently convex lateral margin (Fig. 12Q, S, U). The diaphysis has some fractures, and it lacks some portions of bone, but overall narrows distally while maintaining the D-shaped section. In its distalmost preserved portion, the radius is anterolaterally deflected (Fig. 12Q–S).

Remarks. The radius of GPIT-PV-122984 is relatively gracile, similarly to what documented in *Dy. lettowvorbecki* (Hübner 2018, appendix 1), *Dr. altus* (Galton 1981), *Iy. raathi* (Forster *et al.* 2023), *U. aphanoecetes* (Carpenter & Wilson 2008), *M. atherfieldensis* (Bonsor *et al.* 2023), *Ou. nigeriensis* (Bertozzo *et al.* 2017) and *P. gobiensis* (Norman 2002), whereas it is more robust in *Ig. bernissartensis* (Norman 1980).

Femur. The left femur is preserved with its proximal portion broken and, therefore, missing its head. The preserved shaft, dorsal to the distal epiphysis, shows multiple fractures and deformation. Despite these alterations, the femur was originally slender, anteroposteriorly bowed in mediolateral view and mediolaterally bowed in anteroposterior view (Fig. 13A–D). Therefore, the element shaft presented medial and posterior slightly concave surfaces. At the broken proximal edge, the anterior surface shows a laterally constricted process, partially separated from the shaft, representing the base of the missing lesser trochanter (Fig. 13A, B). The fourth trochanter is fully preserved on the medial margin of the posterior face of what was probably the proximal shaft (Fig. 13B–D). This trochanter is pendant shaped and forms a posteroventrally elongated, tapering process. A nutritional foramen lies immediately lateral to its base (Fig. 13C). In medial view, anterior but distinct from the trochanter base, is an oval insertion scar for musculus

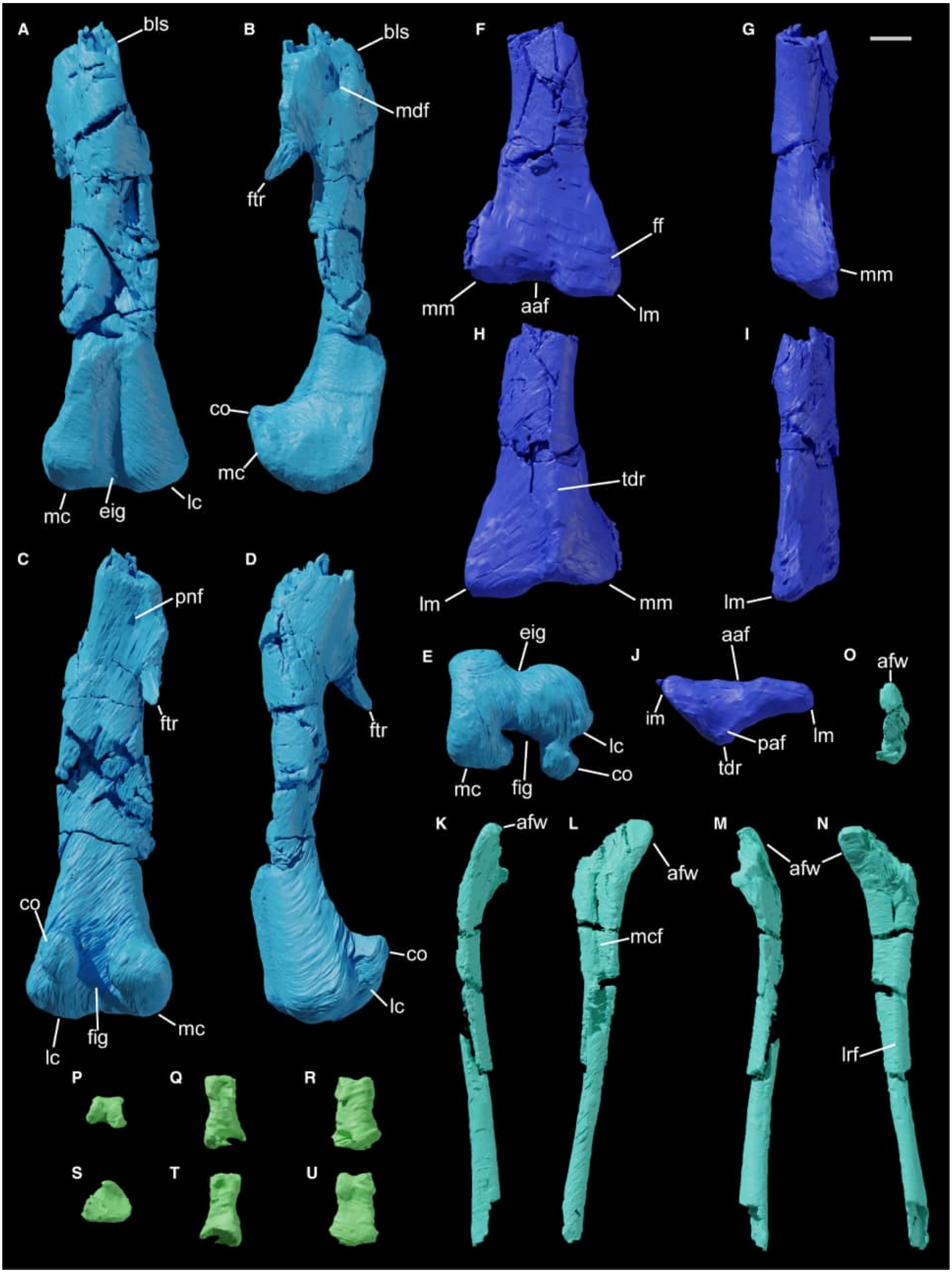
A
bls
mc
eig
lc
B
bls
mdf
ftr
co
mc
F
ff
mm
aaf
lm
G
mm
H
tdr
lm
mm
I
lm
C
pnf
ftr
co
lc
fig
mc
D
ftr
co
lc
E
eig
lc
co
mc
fig
J
aaf
im
paf
lm
tdr
O
afw
K
afw
L
afw
mcf
M
N
afw
lrf
P
Q
R
S
T
U

FIG. 13. Hindlimb skeleton of GPIT-PV-122984. A–E, left femur in: A, anterior; B, medial; C, posterior; D, lateral; E, distal view. F–J, left tibia in: F, anterior; G, medial; H, posterior; I, lateral; J, distal view. K–O, reconstructed appearance of left fibula in: K, anterior; L, medial; M, posterior; N, lateral; O, proximal view. P–U, right Ph IV-1 in: P, distal; Q, lateral; R, dorsal; S, proximal; T, medial; U, ventral view. *Abbreviations*: aaf, anterior astragalus facet; afw, anterior fibular wing; bls, base of lesser trochanter; co, condyloid; eig, extensor intercondylar groove; ff, fibular facet; fig, flexor intercondylar groove; ftr, fourth trochanter; lc, lateral condyle; lm, lateral malleolus; lrf, lateral ridge of fibula; mc, medial condyle; mdf, medial depression of the femur; mm, medial malleolus; paf, posterior astragalus facet; pnf, posterior nutrient foramen; tdr, tibial distal ridge. Scale bar represents 10 mm.

caudofemoralis longus, with a steep anterior edge and smoother posterior border (Fig. 13B). The distal femur expands laterally into two condyles, separated by anterior and posterior grooves (Fig. 13A, C). Anteriorly, the extensor intercondylar groove is shallow and V shaped, whereas the posterior flexor intercondylar groove forms a deep sulcus (Fig. 13A, C, E). In ventral view, the medial tibial condyle projects posteriorly with a rounded outline and a medially expanded, nearly flat articular surface, partially covering the opening of the flexor groove (Fig. 13E). Its medial wall is flat, edged from the articular surface, and bears fine, longitudinal striations, possibly for the origin of musculus femoro-tibialis (Galton 1981), visible on the exposed bone but not in the CT model (Appendix S1, Fig. S1.3). The lateral fibular condyle bears posteriorly a condylid with a laterally constricted base and a slightly convex surface (Fig. 13E). Although the medial condyle is larger, both condyles end posteriorly at nearly the same level.

Remarks. The femur of GPIT-PV-122984 is relatively gracile and bowed in lateral view, as in dryosaurids (Janensch 1955; Galton 1981, 2009; Barrett *et al.* 2011; Escaso *et al.* 2014), whereas rhabdodontids (Weishampel *et al.* 2003; Chanthasit 2010) and skeletally mature *Te. tilletti* (Forster 1990) have straight shafts. In ankylopollexians, the shaft is more robust and proximally straighter, although still distally bowed (Norman 2004). The fourth trochanter is proximally located, as in dryosaurids and unlike ankylopollexians (Galton 1981; Norman 2004; Rotatori *et al.* 2020). The fourth trochanter of GPIT-PV-122984 is pendant shaped, as in dryosaurids (Janensch 1955; Galton 1981; Barrett *et al.* 2011), *Z. shqiperorum* (Godefroit *et al.* 2009), *Ia. smithi* (Zanno *et al.* 2023), *Te. tilletti* (Forster 1990), and *J. shangyuanensis* (Han *et al.* 2012), but lacks the prominent hook-like morphology of *Hy. foxii* (Galton 1974) and most thescelosaurids (e.g. Gilmore 1915; Scheetz 1999; Krumenacker *et al.* 2023; Avrahami *et al.* 2024). In *Iy. raathi*, the fourth trochanter may form a pendant process or a triangular fin, depending on the specimen (Forster *et al.* 2023), whereas in *Ca. dispar* (Gilmore 1909) and *Ob. bunnueli* (Sánchez-Fenollosa *et al.* 2023) it forms a ridge, and in most styracosternans it is even wider dorsoventrally (Norman 2004). A nutrient foramen near the fourth trochanter, as in GPIT-PV-122984, is also present in *Dy. lettowvorbecki* (Hübner 2018, appendix 1) and *V. canaliculatus* (Barrett *et al.* 2011), *J. shangyuanensis* (Han *et al.* 2012), and several thescelosaurids (Gilmore 1915; Avrahami *et al.* 2024). GPIT-PV-122984 has a rounded fossa for the caudofemoral musculature on the medial side of the femur, as is typical of dryosaurids (Barrett *et al.* 2011; Escaso *et al.* 2014). This fossa is well separated from the fourth trochanter, as in *Dy. lettowvorbecki* (Janensch 1955), *Dryosaurus* (Galton 1981) and *Eo. nanohallucis* (Escaso *et al.* 2014), whereas the fossa is separated by a raised ridge in *El. nigeriensis* (Galton 2009), is located at the base of the trochanter in *V. canaliculatus* (Barrett *et al.* 2011), and directly on the lateral face of the trochanter in *Iy. raathi* (Forster *et al.* 2023). This fossa is closer to the trochanter and extends more into the distal part of the shaft in *Ca. dispar* (Gilmore 1915), many styracosternans (Norman 1980; Bertozzo *et al.* 2017; Lockwood *et al.* 2021), and *J. shangyuanensis* (Han *et al.* 2012). The extensor intercondylar groove is shallow and open in GPIT-PV-122984 as in *Dy. lettowvorbecki* (Janensch 1955; Galton 1981), *Dryosaurus* (Shepherd *et al.* 1977; Galton 1981), *Eo. nanohallucis* (Escaso *et al.* 2014) and *Iy. raathi* (Forster *et al.* 2023). In particular, it resembles the V-shaped extensor groove of *Dy. lettowvorbecki* (e.g. GPIT/RE/4156, MB.R.2517, MB.R.2511; Hübner 2018, text-fig. 16B–D). Conversely, the groove is deeper and U shaped in *V. canaliculatus* (Galton 1975; Barrett *et al.* 2011), *El. nigeriensis* (Galton 2009), *Ca. dispar* (Gilmore 1909), *U. aphanoecetes* (Carpenter & Wilson 2008), *Cu. prestwichii* (Maidment *et al.* 2022), *Draconyx loureiroi* (Rotatori *et al.* 2022), *Ob. bunnueli* (Sánchez-Fenollosa *et al.* 2023), *P. gobiensis* (Norman 2002), rhabdodontids (Weishampel *et al.* 2003; Chanthasit 2010), and *Te. tilletti* (Forster 1990). The groove is instead partially enclosed in *Ou. nigeriensis* (Taquet 1976), *Ig. bernissartensis* (Norman 1980), *M. atherfieldensis* (Bonsor *et al.* 2023) and *Co. chasei* (Lockwood *et al.* 2024). The groove is absent or poorly developed in *Hy. foxii* (Galton 1974), *J. shangyuanensis* (Han *et al.* 2012) and *Or. cubicularis* (Krumenacker *et al.* 2023). The medial condyle of GPIT-PV-122984 has a medial protrusion over the flexor groove, as in *Dy. lettowvorbecki* dy36 and MB.R.2511 (Janensch 1955, pl. 14, fig. 1d; Hübner 2018 text-fig. 16D) and *V. canaliculatus* IWCMS 2007·4 (Barrett *et al.* 2011, text-fig. 6H), although it is less developed in some smaller femora of both taxa (*Dy. lettowvorbecki* MB.R.2517 and GPIT/RE/4156; Hübner 2018, text-fig. 16B, C; *V. canaliculatus* NHMUK R185; Barrett *et al.* 2011, pl. 1, fig. 12). A partially covered opening of the flexor groove occurs in several iguanodontians (e.g. Norman 1980; Weishampel *et al.* 2003; Carpenter & Wilson 2008; Forster *et al.* 2023; Bonsor *et al.* 2023), but is fully open in *Draconyx loureiroi* (Rotatori *et al.* 2022), *Hy. foxii* (Galton 1974) and *J. shangyuanensis* (Han *et al.* 2012). The medial wall of the medial condyle of GPIT-PV-122984 is flat, with fine striations that have been described also for *Dy. lettowvorbecki* dy37 (Janensch 1955, pl. 14, fig. 2), and which are not as pronounced as in *Ig. bernissartensis* (Norman 1980) and *M. atherfieldensis* (Bonsor *et al.* 2023). GPIT-PV-122984 lacks anteroposteriorly expanded distal condyles, unlike many styracosternans (e.g.

Norman 1980; Bertozzo *et al.* 2017; Bonsor *et al.* 2023) and rhabdodontids (Weishampel *et al.* 2003; Chanthasit 2010).

Tibia. The distal portion of the left tibia is preserved. The distalmost diaphysis shows multiple fractures and is nearly elliptical in cross-section, with flattened anterior and posterior surfaces (Fig. 13F, G, I). The distal epiphysis is mediolaterally expanded into medial and lateral malleoli, articulating with the astragalus and calcaneum, respectively. In cross-section it is subtriangular, due to a prominent dorsoventral ridge on the posterior face, between the malleoli (Fig. 13H, J). The lateral malleolus is more expanded laterally and slightly ventrally than the medial one, reflecting the larger size of the astragalus relative to the calcaneum (Fig. 13F, H, J). Between the malleoli, the anterior ventral margin bears a dorsoventral depression forming the anterior astragalus facet (Fig. 13F, J) for the anterior ascending process of the astragalus. Posteriorly, a shallow depression beneath, overhung by the base of the distal ridge, forms a posterior astragalus facet (Fig. 13J). This facet probably related to the articulation with the posterior ascending process of the astragalus. The anterior surface of the lateral malleolus bears a flattened fibular facet (Fig. 13F).

Remarks. The distal tibia of GPIT-PV-122984, with an expanded epiphysis bearing distinct medial and lateral malleoli, has the typical configuration of many dryosaurids (Janensch 1955; Galton 1981; Barrett *et al.* 2011) and other cursorial ornithopods (e.g. Galton 1974; Herne *et al.* 2018; Forster *et al.* 2023), but also of *Draconyx loureiroi* (Rotatori *et al.* 2022). It is less robust than the distal tibiae of *Ig. bernissartensis* (Norman 1980), *M. atherfieldensis* (Bonsor *et al.* 2023) and *Th. neglectus* (Gilmore 1915). The subtriangular cross-section of GPIT-PV-122984 is also recorded for *Dy. lettowvorbecki* (e.g. MB.R.2523 and SMNSoN5; Hübner 2018, text-fig. 18F, G), other dryosaurids (Galton 1981; Barrett *et al.* 2011; Escaso *et al.* 2014), *Iy. raathi* (Forster *et al.* 2023), *Ca. dispar* (Gilmore 1909), *U. aphanoecetes* (Carpenter & Wilson 2008), *Cu. prestwichii* (Maidment *et al.* 2022), *Draconyx loureiroi* (Rotatori *et al.* 2022), *Diluvicursor pickeringi* Herne *et al.* 2018, *Hy. foxii* (Galton 1974), *J. shangyuanensis* (Han *et al.* 2012), various thescelosaurids (Avrahami *et al.* 2024), and also some styracosternans (e.g. Bonsor *et al.* 2023; Lockwood *et al.* 2024), but conversely *Ig. bernissartensis*, *Hi. scutodens* and *R. priscus* lack a prominent ridge between the malleoli (Norman 1980; Chanthasit 2010; McDonald *et al.* 2010). The lateral malleolus of GPIT-PV-122984 is slightly ventrally expanded, as in dryosaurids (Janensch 1955; Galton 1981; Barrett *et al.* 2011; Escaso *et al.* 2014), but less so than in *Ca. dispar* and *U. aphanoecetes* (Carpenter & Wilson 2008), *Ob. bunnueli* (Sánchez-Fenollosa *et al.* 2023), rhabdodontids (Weishampel *et al.* 2003; Chanthasit 2010) and *Te. tilletti* (Forster 1990). A shallow depression on the posterior part of the ventral surface related to the posterior astragalus facet, like in GPIT-PV-122984, is reported for all of the preserved specimens of *Dy. lettowvorbecki* (Hübner 2018), *V. canaliculatus* (Barrett *et al.* 2011) and *Co. chasei* (Lockwood *et al.* 2024). Galton (1981) noted a marked posterior notch to receive the astragalus in the distal epiphysis of the *Dr. altus* lectotype (YPM 1876) and a lost *Dy. lettowvorbecki* specimen (dyIV), although for the latter this feature is evident only from ambiguous drawings (fig. 20A of Galton 1981, from Janensch 1955, fig. 70). In contrast, the specimens listed by Galton (1981) for lacking this notch are all ascribed to *Dy. lettowvorbecki* (fig. 19G–N: HMN WJ9027/MB.R.2523 and HMN WJ975/MB.R.2524; it was also indicated in dy38 from Janensch 1955, pl. 14, fig. 3), except for *Dr. altus* YPM 1884, which again is represented only by an ambiguous drawing (Galton 1981, fig. 15B). Therefore, although Galton (1981) did not formalize this distinction, a pronounced notch might differentiate *Dr. altus* from *Dy. lettowvorbecki*.

Fibula. Two long bone fragments are interpreted as the proximal portion and part of the diaphysis of the left fibula, found displaced, but matching in size and morphology. The fibula is slender and elongate (Fig. 13K–N). The proximal fragment bears several transverse fractures and a bowed outline in anterior view, probably due to taphonomic distortion. The proximal epiphysis is incomplete posteriorly, but the anterodorsally projecting fibular wing is preserved (Fig. 13L, N). In medial view, a dorsoventral groove forms a concavity on the proximal fragment (Fig. 13L). The proximal fragment is mediolaterally compressed in its dorsal portion, whereas more ventrally it develops a subtriangular cross-section with a ridge on the lateral side (Fig. 13K, M, O). The diaphyseal fragment has an elliptical, anteroposteriorly compressed cross-section (Fig. 13L, N), giving the fibular shaft a twisted appearance.

Remarks. The anterior margin of the proximal end of the fibula of GPIT-PV-122984 is concave, because of the expansion created by the fibular wing, as is the case in many ornithopods, except for most hadrosaurids (Horner *et al.* 2004; Poole 2022).

Pedal phalanx. For description, the element flexor surface was oriented facing ventrally. A preserved pedal phalanx is tentatively interpreted as the first phalanx of the right fourth digit (Ph IV-1). The proximal articular surface is dorsoventrally concave with a subtriangular outline, although damaged medially (Fig. 13S), and is subequal in width and height. The shaft continues this subtriangular outline, with a broad, flat ventral surface and a narrower dorsal surface (Fig. 13R, U). Distally, the shaft tapers both lateromedially and dorsoventrally, supporting a distal articular surface narrower than the proximal one (Fig. 13Q–U). The distal articular surface bears two rounded condyles, each with a ridge at its edge: the medial ridge directed medioventrally, the lateral one lateromedially (Fig. 13P). The medial projection is larger, generating an asymmetrical V-shaped cross-section of the distal end, with a ventral concavity. The ridge of the lateral condyle ends proximally with a small proximolateral projection (Fig. 13R).

Remarks. The preserved phalanx of GPIT-PV-122984 resembles the morphology of some similar-sized Ph IV-1 specimens of *Dy. lettowvorbecki* (e.g. GPIT/RE/6226 and MB.R.1542.2; Hübner 2018, text-fig. G-L), particularly with regard to the subtriangular proximal surface and the distal condyles configuration, with the medial projection larger than the lateral one.

ONTOGENETIC STAGE ASSESSMENT

Sutural closure

Cranial skeleton. The cranial elements of GPIT-PV-122984 are separated along sutural surfaces, except for the exoccipital–opisthotic and the basisphenoid–parasphenoid, which form two fused complexes, with obliterated suture lines (*sensu* Bailleul *et al.* 2016). In *Dy. lettowvorbecki*, the exoccipital–opisthotic are reportedly the first elements to fuse, followed by the base of the cranium, which includes the basisphenoid, the parasphenoid and the basioccipital (Hübner & Rauhut 2010). In GPIT-PV-122984 the basioccipital is unfused and disarticulated from the parabasisphenoid complex, as in the small specimen MB.R.3536, but unlike the early ontogenetic stage BSPG AS I 834, in which the basioccipital and parabasisphenoid are closely sutured (Hübner & Rauhut 2010). In the larger *Dy. lettowvorbecki* GZG V. 6481, the basioccipital remains separated from the parabasisphenoid at its suture (Hübner & Rauhut 2010). In *Dr. elderae*, the otoccipital and basicranium already form a fused complex in early ontogenetic stages (Dunfee 2022). The next elements expected to fuse in *Dy. lettowvorbecki* are the supraoccipital and parietal (Hübner & Rauhut 2010). Although the parietal is absent in GPIT-PV-122984, the supraoccipital does not show signs of breakage along its contact surfaces, nor fusion with the surrounding bones, unlike in the larger *Dy. lettowvorbecki* dyA/MB.R.1372 or other skeletally mature iguanodontians, in which it is tightly fused to the parietal (Taquet 1976; Sobral *et al.* 2012; Lockwood *et al.* 2024). The preserved right frontal of GPIT-PV-122984 has a straight, non-interdigitated interfrontal suture, with no fusion with the missing left frontal (Bailleul *et al.* 2016), consistent with skeletally immature ornithopods (Verdú *et al.* 2015; Dunfee 2022), including *Dy. lettowvorbecki* (e.g. GPIT/RE/1595/17 and GPIT/RE/1595/15; Janensch 1955; Hübner & Rauhut 2010).

Axial skeleton. The degree of neurocentral suture closure varies among the preserved vertebrae of GPIT-PV-122984. Although CT imaging slightly reduced suture visibility compared with the exposed bone (Appendix S1, Figs S1.4–S1.6), the segmentation process enabled us to evaluate the degree of fusion not only externally, but also on all of the synchondrosial surfaces (Appendix S1, Figs S1.7A–D, S1.8A, B). All post-axial cervical vertebrae except Cv3 show the neural arch aligned with the centrum, with at least partial neurocentral suture closure. In Cv3, the arch is fully disarticulated from the centrum and both synchondrosial surfaces are smooth, indicating minimal fusion (Fig. 8B, C). Cv4 shows a faint suture line, limited to the right side (Fig. 8M; Appendix S1, Fig. S1.4), suggesting partial closure. In Cv5 the suture is visible anteriorly at the arch peduncles and partly in lateral view (Fig. 8Q, S). From the 3D model of Cv6 and Cv7, sutures are visible only in posterior view (Fig. 9C, I). The 3D model of Cv8 shows a partially closed left neurocentral suture, visible across the parapophysis and posteriorly below the peduncle (Fig. 9M–O), whereas its right suture is almost closed (Fig. 9P). Cv9 exposes most of the neurocentral area: the left suture is partially closed, visible anteriorly at the parapophysis and posteriorly (Fig. 9S–U; Appendix S1, Fig. S1.5), whereas the right is partially closed but still largely open anteriorly (Fig. 9V; Appendix S1, Fig. S1.6). The D1 centrum is entirely exposed: the right neurocentral suture is well defined and is only slightly closed (Fig. 10E; Appendix S1, Fig. S1.5), whereas the left is almost closed (Fig. 10B; Appendix S1, Fig. S1.6). In D2, the right neurocentral suture is nearly open with only small bony bridges (Fig. 10J, K; Appendix S1, Fig. S1.5), but the left one is almost fully closed (Fig. 10H; Appendix S1, Fig. S1.6), visible only in posterior view (Fig. 10J). The two more posterior preserved dorsal vertebrae have their neural arch and centrum disarticulated, given that their contact surfaces are irregular with ridges, suggesting ongoing fusion but still essentially open sutures (Fig. 11G, H, O, P). In comparison, the large *Dy. lettowvorbecki* specimen dyI retains at least partially open neurocentral sutures in all preserved cervicals and dorsals (Hübner 2018). Even the larger isolated cervicals of *Dy. lettowvorbecki* show partially open neurocentral sutures (Hübner 2018). However, a small *Dy. lettowvorbecki* axis, GPIT-PV-1120503 (Appendix S1, Fig. S1.9A–D), already has at least partially closed neurocentral sutures, with the neural arch firmly aligned with the centrum, similar to what is observed in the associated vertebrae of comparable size in GPIT-PV-122984. Some degree of distortion affected several of the vertebrae of GPIT-PV-122984, probably influencing the differential closure of the neurocentral sutures through the preserved series, as reported also by Hübner (2018). However, the overall degree of fusion is consistent throughout most of the preserved cervical series, except for Cv3. Moreover, this fusion extends into the internal portion of the neurocentral synchondroses of GPIT-PV-122984. Therefore, the observed fusion pattern is considered to be genuine and not the result of post-mortem processes.

Appendicular skeleton. The scapula–coracoid contact surfaces of GPIT-PV-122984 are irregular with small ridges, suggesting that the two elements remained unfused.

Qualitative traits & ratios

Ontogenetically variable qualitative characters and ratios, previously documented in *Dy. lettowvorbecki* and other ornithopods, can be observed in GPIT-PV-122984.

Cranial skeleton. The basioccipital of GPIT-PV-122984 bears a rounded ventral lip with a single anterior tip, as in early ontogenetic *Dy. lettowvorbecki* (BSPG AS I 834, MB.R.3536), whereas larger specimens (dyA/MB.R.1373, dyB/MB.R.1367, GZG.V.6481) show a trapezoidal lip, with two anterior tips (Hübner & Rauhut 2010). The basioccipital neck dorsoventral height/condyle lateral width ratio for GPIT-PV-122984 is *c.* 0.51, intermediate between small specimens of *Dy. lettowvorbecki* (MB.R.3536 = 0.23; BSPG AS I 834 = 0.36) and larger ones (0.71 for dyA/MB.R.1373; Hübner & Rauhut 2010). The neck lateral width/condyle lateral width ratio for GPIT-PV-122984 is *c.* 1.02, which matches that of small specimens of *Dy. lettowvorbecki* (MB.R.3536 = 1.04; BSPG AS I 834 = 0.97), but exceeds larger ones (dyA/MB.R.1373 = 0.83; dyB/MB.R.1367 = 0.81; Hübner & Rauhut 2010). The basioccipital neck constriction lies near the occipital condyle contribution in GPIT-PV-122984, as in the case of the early ontogenetic stage *Dy. lettowvorbecki* MB.R.3536, unlike the mid-length constriction of larger specimens. The rhomboidal outline of the basioccipital of GPIT-PV-122984 is laterally wider close to the level of the basal tubera than near the occipital condyle, as also for the early ontogenetic stages of *Dy. lettowvorbecki* and of other ornithischians (Hübner & Rauhut 2010). The supraoccipital of GPIT-PV-122984 bears a faint nuchal crest, as in small *Dy. lettowvorbecki* (e.g. BSPG AS I 834; Hübner & Rauhut 2010; lost specimen shown in Janensch 1955, fig. 7), and early ontogenetic stage *Dr. elderae* CM 11340 (Dunfee 2022). Conversely, larger dryosaurid specimens, such as *Dy. lettowvorbecki* dyA/MB.R.1372 (Sobral *et al.* 2012) or *Dr. elderae* CM 3392 and CM 87688 (Carpenter & Lamanna 2015; Dunfee 2022) have a thin but taller and sharper nuchal crest. The prootic crest is low in GPIT-PV-122984, as in the early ontogenetic stage *Dy. lettowvorbecki* BSPG AS I 834 (Hübner & Rauhut 2010), whereas in the larger dyA/MB.R.1370 it is notably sharper (Sobral *et al.* 2012). In GPIT-PV-122984, the prootic appears to incompletely enclose the trigeminal foramen, a condition also seen in the early ontogenetic stage *Dr. elderae* CM 11340. In contrast, the trigeminal foramen is fully enclosed by the prootic in larger dryosaurids, as in *Dy. lettowvorbecki* dyA/MB.R.1370 (Sobral *et al.* 2012) and *Dr. elderae* CM 3392 and CM 87688 (Carpenter & Lamanna 2015; Dunfee 2022), but also in the small *Dy. lettowvorbecki* prootic GPIT-PV-69072 (comparable in size to GPIT-PV-122984), which clearly encloses the trigeminal foramen. This notable difference between GPIT-PV-69072 and GPIT-PV-122984 may result from damage to the latter, although there are no clear indications of breakage, or alternatively, from intraspecies variation. The parabasisphenoid of GPIT-PV-122984 appears to have a body length (excluding the anterior rostrum and the posterior contributions to the basal tubera) subequal to the width (length/width ratio *c.* 1.09), whereas in the larger specimen *Dy. lettowvorbecki* dyA/MB.R.1373 the body of the parabasisphenoid appears to be longer than wider (ratio *c.* 1.25). The parabasisphenoid contributions to the basal tubera of GPIT-PV-122984 are prominent but lack the rugosity of the larger *Dy. lettowvorbecki* dyA/MB.R.1373 (Hübner & Rauhut 2010). The abducens foramen of GPIT-PV-122984 is formed by a notch, as in the early ontogenetic stage *Dr. elderae* CM 11340, whereas the advanced ontogenetic stage CM 87688 possesses a fully enclosed foramen (Dunfee 2022). The frontal of GPIT-PV-122984 has a small, flat dome, comparable to *Dy. lettowvorbecki* (BSPG AS I 834, GPIT/RE/1595/15 and GPIT/RE/1595/17) and other ornithopods identified as skeletally immature (Evans *et al.* 2007; Forster *et al.* 2023).

Appendicular skeleton. In the scapula of GPIT-PV-122984, the posteroventral edge of the shaft base lacks the bulge present in large *Dy. lettowvorbecki* (e.g. GZG.V.6287) and resembles smaller specimens, such as GPIT/RE/5651 (Hübner 2018). The coracoid of GPIT-PV-122984 is gently concave posteriorly, a feature that becomes more marked during ontogeny in *Dy. lettowvorbecki*, and lacks the lateral ridge reported for large *Dy. lettowvorbecki* (e.g. MB.R.1485, MB.R.3474; Hübner 2018). The olecranon process of the ulna in *Dy. lettowvorbecki*, known to enlarge during ontogeny, is difficult to identify in GPIT-PV-122984, and in the small GPIT/RE/3451. The lateral proximal process of the ulna of GPIT-PV-122984 matches the condition of the smaller GPIT/RE/3451 rather than the stronger process of the larger GPIT/RE/3909 (Hübner 2018). The femur of GPIT-PV-122984 bears a medial muscle scar near the fourth trochanter with a sharp anterior and fluent posterior edge, resembling small to medium *Dy. lettowvorbecki* (e.g. MB.R.2517), whereas in larger femora (e.g. MB.R.2511) the depression is shallower with a steeper anteroventral edge (Hübner 2018). The extensor intercondylar groove of the distal femur of GPIT-PV-122984 is shallow, as in small *Dy. lettowvorbecki* (e.g. MB.R.2517, GPIT/RE/4156), contrasting with the deeper groove of larger specimens (e.g. MB.R.2511; Hübner 2018). In Ph IV-1 of GPIT-PV-122984, the proximal articular surface is subequal in lateral and dorsoventral dimensions, unlike larger individuals, in which it is taller than wide (Hübner 2018).

Morphometric analysis

For graphical purposes, all PC1 and PC2 scores were multiplied by −1 and are hereafter referred to as inverted PC1 and PC2.

In PCA of the femora dataset, PC1 explains 78.4% of the total variance and PC2, 3.7%. PC1 is influenced almost equally by all measured variables, with all of the related loadings between −0.21 and −0.10 (Appendix S2, Fig. S2.1A), whereas PC2 shows greater variability, with loadings ranging between −0.17 and 0.31 (Appendix S2, Fig. S2.1A). GPIT-PV-122984 plots close to the smaller femora in total length in the dataset, on the left side of the *Dysalotosaurus* morphospace (Appendix S2, Fig. S2.2A), corresponding to negative values of inverted PC1 (originally positive values of PC1). GPIT-PV-122984 is separated from most of the other specimens along PC2, which accounts for a minor portion of the total variance.

PCA of the tibiae dataset returned a PC1 that explains 76.8% of the total variance, and PC2, 10.5%. PC1 is similarly influenced by all of the original variables, with loadings ranging between −0.14 and −0.27 (Appendix S2, Fig. S2.1B), whereas the PC2 loadings range from −0.40 to 0.32 (Appendix S2, Fig. S2.1B). GPIT-PV-122984 plots in the left *Dysalotosaurus* morphospace area, with small to medium tibiae, corresponding to negative inverted PC1 values (Appendix S2, Fig. S2.2B).

In both analyses, PC1 captures most of the variance with similar loadings, and therefore represents an ‘overall size axis’ (Hammer & Harper 2008), and size was demonstrated to be a reliable ontogenetic indicator in *Dy. lettowvorbecki* (Hübner 2012, 2018). In addition, given that the geometric mean of long bone measures is a good proxy for specimen absolute size (Klingenberg 1996), RMA regressions between inverted PC1 and the log-transformed geometric mean enable us to illustrate the growth series of the species, both for the femora and the tibiae datasets.

The RMA regression model for the femora dataset shows a strong correlation between age/size and skeletal elements measured ($p > 2 \times 10^{-16}$; $R^2 = 0.8377$), with GPIT-PV-122984 plotting among the smallest specimens and probably earliest ontogenetic stages (Fig. 14A). The tibiae regression model, although based on a smaller sample, also shows a good correlation between age/size and skeletal elements measured ($p > 1.48 \times 10^{-5}$; $R^2 = 0.6362$), placing GPIT-PV-122984 again among early ontogenetic stages (Fig. 14B).

Finally, the regression equation of Hübner *et al.* (2021) was used to estimate the absolute age of GPIT-PV-122984: $y = 0.257x - 3.936$, where x is the mediolateral distal width of the femur (*c.* 33.7 mm for GPIT-PV-122984) and y the absolute age. The result indicates an absolute age between 4 and 5 years for GPIT-PV-122984 (*c.* 4.72).

ANCESTRAL STATE RECONSTRUCTION

The ASR on the locus of neurocentral fusion in the cervical series shows a diversified condition among archosauromorphs (Fig. 15). Pseudosuchians consistently lack a cervical locus of neurocentral fusion, observed both in modern crocodylians and in Triassic species (Brochu 1996; Irmis 2007; Nesbitt 2007), suggesting its ancestral absence in the clade. In contrast, the Triassic archosauromorph *Hyperodapedon* already shows a cervical locus of neurocentral fusion (Heinrich *et al.* 2021). A cervical locus is also seen in the pterosaur *Anhanguera* (Kellner & Tomida 2000). Within Dinosauria, the locus is variably present. Data regarding Ornithischia are scarce. At least two ceratopsians, *Montanoceratops* and *Protoceratops*, show a locus of neurocentral fusion in the cervical series (Brown & Schlaikjer 1940; Chinnery & Weishampel 1998; Irmis 2007), whereas it is apparently absent in *Chasmosaurus* (Currie *et al.* 2016; Griffin *et al.* 2021). Most reported ornithopods, including *Dryosaurus*, show a simple tail-to-head closure sequence (Gilmore 1909, 1925; Irmis 2007; Galton 2009; Griffin *et al.* 2021), lacking a cervical locus of neurocentral fusion. However, the new evidence from *Dysalotosaurus* suggests that such a locus may have developed in at least some ornithopod species. Among sauropodomorphs, a cervical locus is absent in Triassic to Middle Jurassic taxa (Yates 2003; Galton & Kermack 2010; Hofmann & Sander 2014; Fronimos & Wilson 2017; Griffin *et al.* 2021), but present in several Late Jurassic and Cretaceous macronarians (Ikejiri 2003; Gallina 2011) or diplodocoids (Melstrom *et al.* 2016; Tschopp & Mateus 2017), with the exception of *Haplocantosaurus* (Hatcher 1903; Irmis 2007). Theropods generally possess a cervical locus of neurocentral fusion (De Klerk *et al.* 2000; Xu *et al.* 2004; O’Connor 2007; Fowler *et al.* 2011; Malafaia *et al.* 2017; Griffin 2018; Nesbitt *et al.* 2019; Poust *et al.* 2020; Griffin *et al.* 2021; Caldwell *et al.* 2024; Wang & Pei 2025), with exceptions such as *Eustreptospondylus* (Sadleir *et al.* 2008) and *Oksoko* (Funston 2024). Extant birds consistently retain a cervical locus (Starck 1993). The ASR indicates that absence of a cervical locus was the ancestral archosaur condition, with independent acquisitions in sauropodomorphs and theropods. In fact, the presence of a cervical locus probably represented the ancestral state in Neosauropoda and Avetheropoda.

The locus of neurocentral fusion in the caudal series is widespread among extinct archosauromorphs (Appendix S3, Fig. S3.1), with few exceptions in ceratopsians and theropods. In contrast, extant altricial birds show a head-to-tail closure sequence (Starck 1993), and thus lack a caudal locus. The ASR recovered a 50% probability that the last common ancestor of the sampled

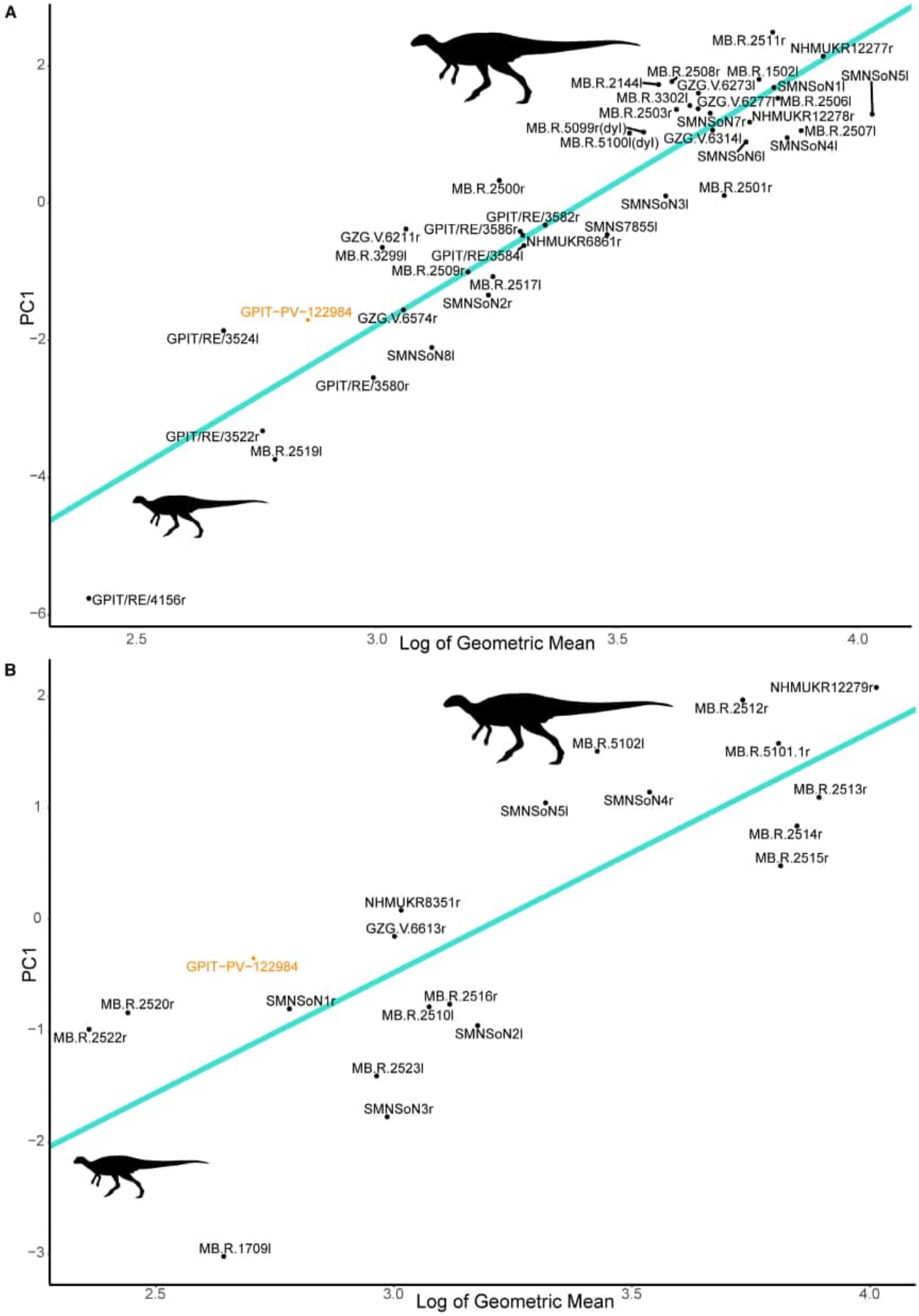

FIG. 14. Morphometric analysis. The position of GPIT-PV-122984 is marked in orange. A, reduced major axis (RMA) regression of the femora. B, RMA regression of the tibiae. Silhouettes of *Dysalotosaurus* modified from http://phylopic.org/ (credit: Matthew Dempsey; CC BY 4.0).

archosauromorphs possessed a caudal locus, and the same value is found also at the base of the clade Dinosauria. The probability rises to 89.2%, suggesting that a caudal locus of fusion was ancestrally present in pseudosuchians, Cerapoda, Theropoda, and in the last common ancestor of *Plateosaurus* and Sauropoda.

PHYOLOGENETIC ANALYSIS

Equal weighting

The parsimony analysis with EW for all characters retained 312 MPTs of 1399 steps each. In the strict consensus tree, both the normal and the OSC OTUs of GPIT-PV-122984 fall inside Dryosauridae (Fig. 16A), in a polytomy with the *Dysalotosaurus* OTUs (both normal and OSC). Dryosauridae also include both *Iyuku* (both normal and OSC), *Dryosaurus altus* (adult), and '*Dryosaurus* juvenile', whereas *Kangnasaurus* and *Valdosaurus* fall outside the clade. The inclusion of GPIT-PV-122984 among Dryosauridae is based on the following combination of characters: weakly developed acromion process (char. 195, 1 > 0); and scapula and coracoid contributions to the glenoid fossa in craniocaudal length subequal (char. 205, 0 > 1). Furthermore, GPIT-PV-122984 forms a clade with the *Dysalotosaurus* OTUs based on: lateral distal condyle of humerus wider (char. 216, 1 > 0); and femur bowed laterally (char. 291, 0 > 1).

Extended implied weighting k = 3

The parsimony analysis using EIW with k = 3 for all characters retained 5 MPTs of 1420 steps each. In the strict consensus tree, both the normal and the OSC OTUs of GPIT-PV-122984 fall inside Dryosauridae (Fig. 16B; Appendix S4, Fig. S4.1), in a polytomy consisting of *Dryosaurus altus*, '*Dryosaurus* juvenile' and the clade formed by *Iyuku* and *Dysalotosaurus* (both normal and OSC). *Kangnasaurus* and *Valdosaurus* fall outside Dryosauridae. The inclusion of GPIT-PV-122984 among Dryosauridae is based on a weakly developed acromion process (char. 195, 1 > 0). The *Iyuku* + *Dysalotosaurus* clade is supported by the absence of a ventral keel on centra of cranial and mid-dorsal vertebrae (char. 163, 1 > 0).

Extended implied weighting k = 5

The parsimony analysis using EIW with k = 5 for all characters retained 5 MPTs of 1415 steps each. In the strict consensus tree, both the normal and the OSC OTUs of GPIT-PV-122984 have the same position as in the k = 3 analysis (Appendix S4, Fig. S4.2), supported by the same characters.

Extended implied weighting k = 10

The parsimony analysis using EIW with k = 10 for all characters retained 3 MPTs of 1400 steps each. In the strict consensus tree, both the normal and the OSC OTUs of GPIT-PV-122984 fall inside Dryosauridae (Fig. 16C; Appendix S4, Fig. S4.3), in a polytomy with the *Dy. lettowvorbecki* OTUs (both normal and OSC). Dryosauridae also contains both *Iyuku* (normal coding and OSC), *Dryosaurus altus* (adult) and '*Dryosaurus* juvenile', whereas *Kangnasaurus* and *Valdosaurus* fall outside the clade. The inclusion of GPIT-PV-122984 OTUs among Dryosauridae and inside a clade with the *Dysalotosaurus* OTUs is supported by the same combination of characters recovered in the EW analysis.

Extended implied weighting k = 11

The parsimony analysis using EIW with k = 11 for all characters retained 3 MPTs of 1400 steps each. In the strict consensus tree, both the normal and the OSC OTUs of GPIT-PV-122984 fall inside Dryosauridae (S4, Fig. S4.4), in a polytomy with the *Dy. lettowvorbecki* OTUs (both normal and OSC). Dryosauridae includes also *Iyuku* (both normal coding and OSC), *Dryosaurus altus* (adult), and '*Dryosaurus* juvenile', whereas *Kangnasaurus* and *Valdosaurus* fall outside the clade. The position of GPIT-PV-122984 OTUs is supported by the same combination of characters recovered in the EW analysis (and in the k = 10 analysis).

DISCUSSION

Taxonomic attribution & anatomical details

The elements encased in the block GPIT-PV-122984 belong to a single small *Dy. lettowvorbecki* individual. No duplicate elements were found in the block, and all of them are consistent in size. Some elements show a subparallel alignment that denotes an influence of the currents on their position; however, many elements are articulated or semi-articulated, suggesting limited transportation and implying their association. Cranial bones, cervical, and anterior dorsal vertebrae are arranged in a post-mortem opisthotonic position, and also all other elements are closely associated, such as the elements of the left forearm. In addition, GPIT-PV-122984 plots in a similar position in the RMA regressions for both the tibia

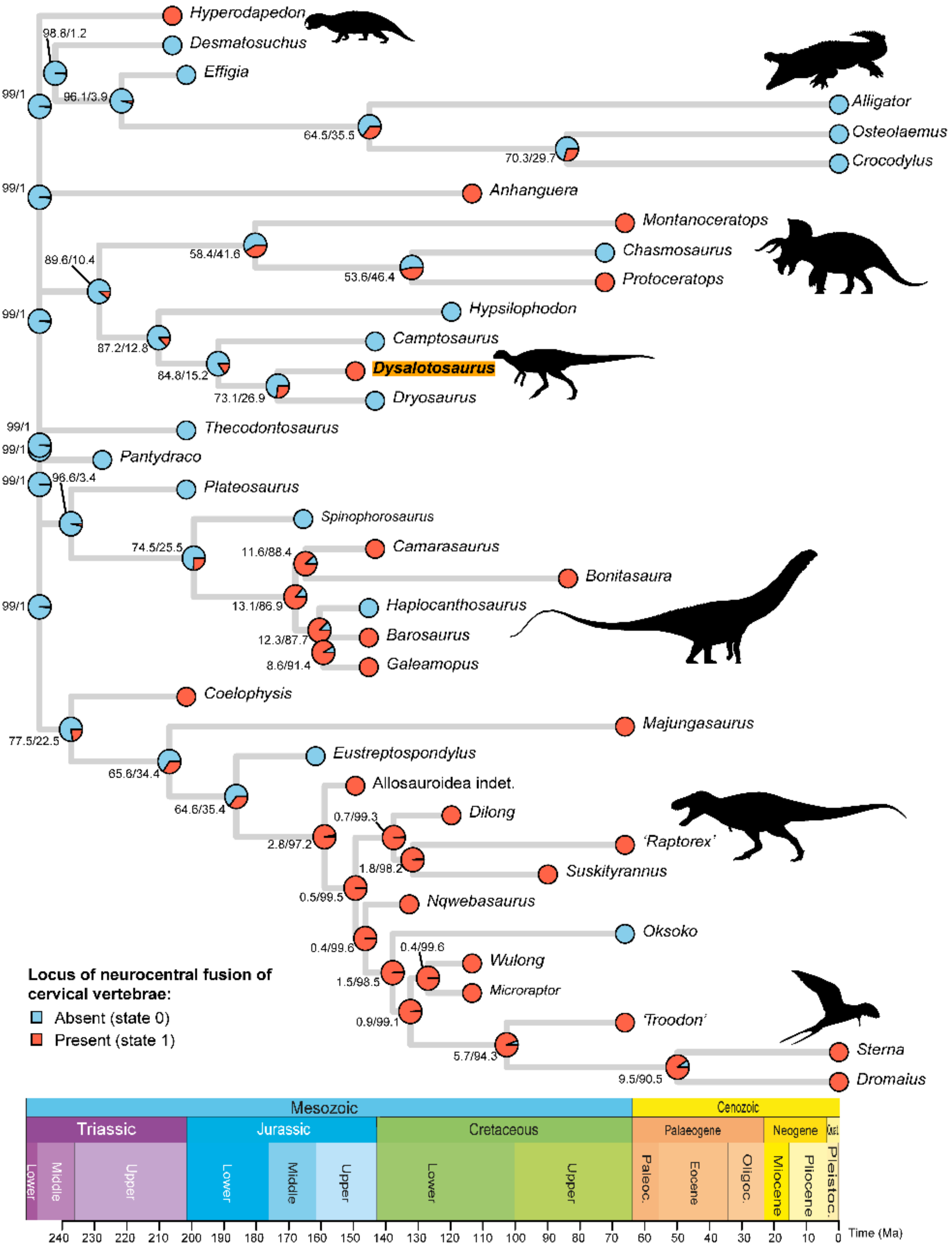
Hyperodapedon
Desmatosuchus
98.8/1.2
Effigia
99/1
96.1/3.9
Alligator
64.5/35.5
Osteolaemus
70.3/29.7
Crocodylus
99/1
Anhanguera
Montanoceratops
58.4/41.6
Chasmosaurus
89.6/10.4
53.6/46.4
Protoceratops
99/1
Hypsilophodon
87.2/12.8
Camptosaurus
Dysalotosaurus
84.8/15.2
73.1/26.9
Dryosaurus
99/1
Thecodontosaurus
99/1
Pantydraco
99/1
98.6/3.4
Plateosaurus
Spinophorosaurus
74.5/25.5
11.6/88.4
Camarasaurus
Bonitasaura
99/1
13.1/86.9
Haplocanthosaurus
12.3/87.7
Barosaurus
8.6/91.4
Galeamopus
Coelophysis
77.5/22.5
Majungasaurus
65.6/34.4
Eustreptospondylus
64.6/35.4
Allosauroidea indet.
0.7/99.3
Dilong
2.8/97.2
'Raptorex'
1.8/98.2
Suskityrannus
0.5/99.5
Nqwebasaurus
Oksoko
0.4/99.6
0.4/99.6
Wulong
1.5/98.5
Microraptor
0.9/99.1
'Troodon'
5.7/94.3
Sterna
9.5/90.5
Dromaius
Locus of neurocentral fusion of cervical vertebrae:
🟦 Absent (state 0)
🟥 Present (state 1)
Mesozoic
Cenozoic
Triassic
Jurassic
Cretaceous
Palaeogene
Neogene
Qt.
Lower
Middle
Upper
Lower
Middle
Upper
Lower
Upper
Paleoc.
Eocene
Oligoc.
Miocene
Pliocene
Pleistoc.
240
230
220
210
200
190
180
170
160
150
140
130
120
110
100
90
80
70
60
50
40
30
20
10
0
Time (Ma)

FIG. 15. Ancestral state reconstruction for the presence of the locus of neurocentral fusion of cervical vertebrae. The position of *Dysalotosaurus* is highlighted in orange. Circles at tips show taxon states, pie charts at nodes show likelihood of ancestral states. The time scale is modified from the International Chronostratigraphic Chart v2024/12 (Cohen *et al.* 2013). Silhouettes modified from http://phylopic.org/ Credits: *Dysalotosaurus*, Matthew Dempsey (CC BY 4.0); all the other silhouettes (*Hyperodapedon* and *Crocodylus*, Steven Traver; *Triceratops*, Jagged Fang Designs; *Galeamopus*, Tasman Dixon; *Tyrannosaurus*, Manuel Brea Lueiro; *Sterna*, Sharon Wegner-Larsen) are CC0 1.0.

and the femur, indicating that the two elements match in proportions with the rest of the *Dy. lettowvorbecki* specimens.

The GPIT-PV-122984 femur shows typical features of Dryosauridae: proximally located fourth trochanter; deep intercondylar distal groove; and a deep pit for musculus caudofemoralis longus at the base of the fourth trochanter. Other cranial and postcranial features also support placement in Dryosauridae. GPIT-PV-122984 is confidently attributed to *Dy. lettowvorbecki*, distinguishable from *Dryosaurus* by: prootic with the CN VII foramen more ventrally placed than the fenestra ovalis and the trigeminal foramen; small first chevron; and lateral radial condyle of the humerus mediolaterally and anteroposteriorly wider than the medial ulnar condyle. The taxonomic attribution is also consistent with the provenance of Ig/WJ quarry in the Tendaguru area, where nearly only *Dy. lettowvorbecki* fossils occur.

Additional features observed for GPIT-PV-122984 that are not yet explicitly reported for *Dy. lettowvorbecki* but which are also present in other specimens, include: basioccipital contribution to the basal tubera projects below the level of the basioccipital contribution to the occipital condyle; and distal tibia lacking a deep notch at the level of the articulation with the posterior ascending process of the astragalus, in contrast to *Dr. altus*. In addition, a cervical series of nine vertebrae can be assessed for *Dy. lettowvorbecki*.

The preserved inner ear morphology is consistent with previous descriptions of *Dy. lettowvorbecki* (Sobral *et al.* 2012; Lautenschlager & Hübner 2013). The anteroposterior inclination of the lateral semicircular canal suggests a slightly upturned alert posture of the head for *Dy. lettowvorbecki*, potentially maximizing binocular vision when looking upward (Lautenschlager & Hübner 2013).

Ontogenetic trends

The separation of cranial elements, incomplete fusion of some vertebrae and of the pectoral girdle, and several cranial and appendicular features agree with the placement of GPIT-PV-122984 as belonging to the earliest ontogenetic stages in the morphometric growth trajectories.

Cranial characters, such as the shape and proportion of the basioccipital, the development of the nuchal and prootic crests, and the frontal dome, correspond to the early ontogenetic stages of *Dy. lettowvorbecki* as described by Hübner & Rauhut (2010). Similarly, scapular and coracoid morphology, the development of the femoral median muscle scar and extensor intercondylar groove, and the proportions of the pedal phalanx are consistent with conditions observed in the smallest individuals of *Dy. lettowvorbecki* (Hübner 2018).

Two braincase features can be discussed in terms of their potential ontogenetic variability in *Dy. lettowvorbecki*. In GPIT-PV-122984, the prootic does not appear to completely surround the trigeminal foramen, whereas in larger individuals, the foramen is entirely enclosed by the prootic, suggesting ontogenetic closure, similar to *Dr. elderae* (Dunfee 2022). However, at least one other small prootic of *Dy. lettowvorbecki* exhibits a fully enclosed trigeminal foramen, indicating either damage to the prootic of GPIT-PV-122984 or intraspecies variation for this feature. In contrast, the abducens foramina of the parabasisphenoid are not fully enclosed in GPIT-PV-122984, paralleling the condition in the early ontogenetic stage *Dr. elderae* (Dunfee 2022) and suggesting that complete enclosure may develops later in ontogeny.

Regarding the postcranial axial skeleton of GPIT-PV-122984, most of the preserved cervical vertebrae exhibit partially closed neurocentral sutures, with the exception of Cv3, which remains completely open. In the dorsal series, D1 and D2 show partially closed sutures, although they are mostly open on the right side. In contrast, the two more posteriorly preserved dorsals have completely open sutures, suggesting the presence of a locus of neurocentral fusion in the cervical series. However, the open condition in Cv3 rules out a simple head-to-tail closure pattern, implying that the locus is situated in the mid-cervical region, from which fusion would have spread. Hübner (2018) demonstrated that caudal neurocentral sutures close earlier than dorsal and cervical ones in *Dy. lettowvorbecki* given that even the larger preserved cervical vertebrae exhibit partially open neurocentral sutures, whereas numerous completely closed vertebrae are observed in the caudal series. The new observations concerning GPIT-PV-122984 do not contradict the previous interpretation, but rather suggest the existence of a complex pattern of neurocentral suture

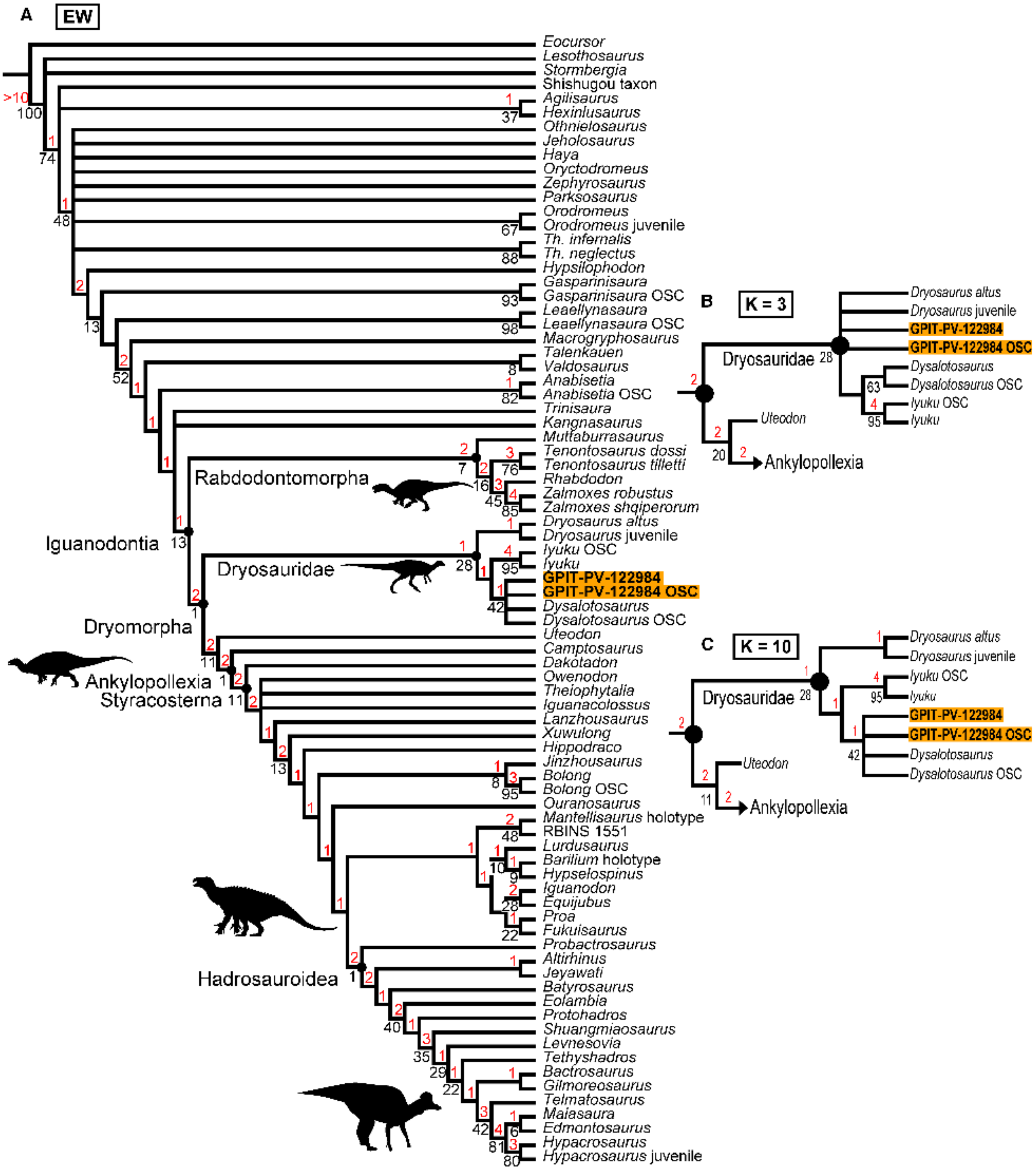

FIG. 16. Strict consensus trees from: A, equal weighting (EW) analysis; B, detail of the Dryomorpha clade (Ankylopollexia collapsed) in the extended implied weighting (EIW) analysis with k = 3; C, detail of the Dryomorpha clade (Ankylopollexia collapsed) in the EIW analysis with k = 10. The positions of the GPIT-PV-122984 operational taxonomic units are highlighted in orange. The numbers above branches (in red) represent Bremer support values, whereas the numbers below branches (in black) represent bootstrap values. *Abbreviation*: OSC, ontogenetically sensitive character. Silhouettes modified from http://phylopic.org/ Credits: *Dysalotosaurus*, Matthew Dempsey (CC BY 4.0); all other silhouettes (*Rhabdodon,* François-Louis Pelissier; *Camptosaurus* and *Iguanodon,* Tasman Dixon; *Corythosaurus,* Craig Dylke) are CC0 1.0.

closure, involving two separate loci of fusion. These loci would have been located in the caudal and cervical series, from which the fusion would have progressed toward the dorsal vertebrae. Given that the caudals are the only preserved vertebrae of *Dy. lettowvorbecki* to show consistently closed neurocentral sutures, it is likely that the process of fusion started in the caudal series. However, GPIT-PV-122984 suggests that the process of closure started independently at the cervical locus, without a linear tail-to-head pattern. Furthermore, a small isolated *Dy. lettowvorbecki* axis, GPIT-PV-1120503, shows partially closed neurocentral sutures, supporting this interpretation. More complete cervical and dorsal series and caudal material of a single individual would be needed to robustly confirm the proposed growth dynamic. Nonetheless, the demonstrated early onset of cervical neurocentral suture closure reinforces the high degree of precociality that has already been recognized for many traits of *Dy. lettowvorbecki* (Hübner & Rauhut 2010; Hübner 2012; Lautenschlager & Hübner 2013).

Histological correlation between distal femur width and absolute age suggests that GPIT-PV-122984 was 4–5 years old at the time of death. This provides a direct correlation between absolute age and the ontogenetic condition of various cranial and postcranial features described herein, representing a rare opportunity for *Dy. lettowvorbecki*, given the scarcity of associated material.

Implications for vertebral fusion timing among Archosauria

The neurocentral fusion sequence appears to be highly variable among archosauromorphs. Neither the simple tail-to-head pattern observed in crocodylians nor the head-to-tail sequence reported in some extant birds can be universally applied to extinct taxa (Brochu 1996; Irmis 2007; Griffin *et al.* 2021). A caudal locus of neurocentral fusion is widespread among archosauromorphs, but a cervical locus is also documented in several lineages. In particular, the presence of both caudal and cervical loci has been identified in many theropod and sauropodomorph dinosaurs (Irmis 2007; Griffin *et al.* 2021; Caldwell *et al.* 2024), the pterosaur *Anhanguera* (Kellner & Tomida 2000), and the rhynchosaur *Hyperodapedon* (Heinrich *et al.* 2021). In these taxa, neurocentral closure is initiated independently from the anterior and posterior regions of the vertebral column. Among ornithischians, data on neurocentral suture closure patterns remain scarce. The new evidence provided by GPIT-PV-122984 represents the first hypothesized description of a cervical locus of neurocentral fusion in Ornithopoda, which probably co-occurred with a caudal locus. All previously documented cases in ornithopods have only a caudal locus reported, but available data on the clade remain limited, with notably no direct reports for hadrosaurids. According to previous studies (Irmis 2007; Griffin *et al.* 2021), *Dryosaurus* shows a simple tail-to-head pattern, in contrast with the cervical locus documented here for the closely related *Dy. lettowvorbecki*. Nonetheless, our first-hand observations challenge these results, which are based, most likely, on literature reviews alone.

Ancestral state reconstructions suggest that the last common ancestor of archosaurs lacked a cervical fusion locus, which arose independently in multiple lineages. In contrast, the last common ancestor of archosaurs had a 50% probability of possessing a caudal locus, although this condition was probably ancestral for Cerapoda (*sensu* Madzia *et al.* 2021), Theropoda, and the last common ancestor of *Plateosaurus* and Sauropoda.

Neurocentral suture closure is often used as an ontogenetic proxy in fossil archosaurs (Griffin *et al.* 2021). However, as demonstrated here and in previous studies (Irmis 2007; Griffin *et al.* 2021; Verrière *et al.* 2022; Caldwell *et al.* 2024), closure sequences among Archosauromorpha cannot be reduced to the extant model patterns and must be assessed species by species. In addition, Griffin (2018) hypothesized that fusion sequence variation may occur within populations of *Coelophysis bauri*. However, detailed accounts of closure patterns remain insufficient for most archosauromorphs, which would be essential to evaluate their variation across clades, within species, and their reliability as ontogenetic indicators. In *Dy. lettowvorbecki*, cervical fusion appears to begin relatively early in ontogeny, reinforcing the need for caution in using isolated vertebrae to infer maturity. The degree of neurocentral suture closure should therefore be used only in combination with other proxies when assessing the ontogenetic stage of *Dy. lettowvorbecki*, as already emphasized for archosaurs in general by Griffin *et al.* (2021).

Phylogeny & ontogenetic sensitive traits

All phylogenetic analyses place both the normal and OSC coding of GPIT-PV-122984 among Dryosauridae. However, only the EW analysis and the EIW analyses with higher k-values (k = 10; k = 11) recover a clade formed exclusively by GPIT-PV-122984 and *Dysalotosaurus*. In contrast, the other EIW analyses (k = 3; k = 5) fail to fully resolve dryosaurid relationships, instead producing a polytomy with GPIT-PV-122984, *Dr. altus* and the clade formed by *Iyuku* and *Dysalotosaurus* OTUs. These results highlight the sensitivity of the Poole (2022) matrix to homoplasy.

Nonetheless, the approach proposed by Poole (2022), as modified in this study, is effective in placing early ontogenetic specimens within a phylogenetic framework, particularly in the case of GPIT-PV-122984, which had already been identified as *Dysalotosaurus*. Poole (2022) argued that the most reliable phylogenetic topology is obtained by scoring ontogenetically variable characters as unknown in taxa represented only by immature individuals. Although this principle was partially followed in this study, the procedure of including in the same analysis both OTUs scored as 'adult' or OSC and as 'juvenile' or normal is considered safer, especially for isolated or fragmentary material. This approach enables assessment of the placement of both scorings and their relative positions in the resulting topology.

CONCLUSION

GPIT-PV-122984 is a semi-articulated small specimen of *Dysalotosaurus lettowvorbecki* (Dryosauridae, Ornithopoda, Dinosauria) from the Upper Jurassic Tendaguru Formation (Tanzania), preserved in a single block. The material represents a single individual, as indicated by the consistent size and close association of axial, cranial and postcranial, and appendicular (forelimb and hindlimb) elements. This exceptional preservation provides a rare opportunity to examine the associated material of *Dy. lettowvorbecki*, facilitating the identification of new anatomical details and providing valuable insights into the ontogenetic osteological variation of the species.

Qualitative traits, ratios and placement on growth trajectories (RMA regressions) agree in identifying GPIT-PV-122984 as an individual at an early ontogenetic stage. We estimate an absolute age at the time of death between 4 and 5 years, enabling precise correlation of its morphological features with a defined ontogenetic stage. In addition to previously reported ontogenetic changes, new patterns are demonstrated by this specimen, particularly in the braincase and vertebral series. The near-complete cervical series and preserved dorsal vertebrae enable direct observation of neurocentral suture closure: most cervicals (except Cv3) have at least partially closed sutures, whereas the posterior dorsals retain open sutures with disarticulated neural arches. This condition cannot be explained by the simple 'tail-to-head' fusion sequence usually assumed for ornithopods, suggesting the presence of a cervical locus of neurocentral fusion in *Dy. lettowvorbecki*.

The presence of a cervical fusion locus in *Dy. lettowvorbecki* represents the first evidence of this condition in Ornithopoda. Ancestral state reconstruction suggests that cervical loci evolved independently in multiple archosauromorph lineages. To refine evolutionary interpretations and assess the reliability of neurocentral closure as an ontogenetic stage proxy, more detailed descriptions of closure sequences in ornithopods and other archosauromorphs are required.

Because the specimen is skeletally immature, the phylogenetic analyses were conducted using a modified approach designed to account for ontogenetic variation in character states, derived from earlier literature (Poole 2022). This method incorporates both virtually mature and immature character scorings in a single analysis and has been shown to reliably place early ontogenetic individuals within a phylogenetic framework.

Acknowledgements. This project was possible thanks to the Erasmus+ Traineeship 2024/2025 Programme, which funded a 3 month stay by RR at the Senckenberg HEP, University of Tübingen (Baden-Württemberg, Germany). FMR's research was supported by National Funds thanks to the FCT – Fundação para a Ciencia e a Tecnologia I.P. by Research Unit UIDB/04035/2020 (https://doi.org/10.54499/UIDB/04035/2020). We are grateful to Dr Ingmar Werneburg for granting access to the collections of GPIT and to Henrik Stöhr for providing valuable information on the Tendaguru material housed there. We are thankful for the access provided to comparative material by Dr Oliver Rauhut of the Bayerische Staatssammlung für Paläontologie und Geologie (Munich), Dr Daniela Schwarz, Dr Andreas Rassuly and Emily Eybing of the Museum für Naturkunde (Berlin), and Dr Rainer R. Schoch of the Staatliches Museum für Naturkunde (Stuttgart). Our thanks to two anonymous reviewers and editors Dr Sally Thomas and Dr Susannah Maidment for their very helpful comments, which greatly improved this paper. We thank the Willi Henning Society for making TNT v1.6 available for the phylogenetic analyses reported in this study. Open access publication funding provided by FCT (b-on). Open access publication funding provided by FCT (b-on).

Author contributions. **Conceptualization** Riccardo Rocchi (RR), Filippo Maria Rotatori (FMR), Gabriel S Ferreira (GSF), Federico Fanti (FF); **Data Curation** RR; **Formal Analysis** RR, FMR; **Funding Acquisition** FMR, RR; **Investigation** RR; **Methodology** RR, FMR; **Project Administration** FF; **Resources** GSF; **Software** GSF; **Supervision** FF, FMR; **Validation** FF, FMR; **Visualization** RR, FMR; **Writing – Original Draft Preparation** RR; **Writing – Review & Editing** RR, FMR, GSF, FF.

DATA ARCHIVING STATEMENT

Supporting data for this manuscript, including the datasets and scripts necessary to replicate phylogenetic and ancestral state analyses are archived in MorphoBank: http://morphobank.org/permalink/?P6025; CT data of the specimen and 3D models resulting from the segmentation are available from MorphoSource: https://www.morphosource.org/projects/000774830.

Editor. Susannah Maidment

SUPPORTING INFORMATION

Additional Supporting Information can be found online (https://doi.org/10.1002/spp2.70085):

Appendix S1. Includes: 3D imaging on Blender; additional anatomical figures (Figs S1.1–S1.9); MorphoSource media list (Table S1.1); detailed measurements (Tables S1.2–S1.19).

Appendix S2. Includes additional figures related to the morphometric analyses (Figs S2.1, S2.2).

Appendix S3. Includes additional information on the ancestral state reconstruction (Table S3.1; Fig. S3.1).

Appendix S4. Includes additional trees from the phylogenetic analyses (Figs S4.1–S4.4).

REFERENCES

Aberhan, M., Bussert, R., Heinrich, W.-D., Schrank, E., Schultka, S., Sames, B., Kriwet, J. and Kapilima, S. 2002. Palaeoecology and depositional environments of the Tendaguru beds (late Jurassic to early Cretaceous, Tanzania). *Fossil Record*, **5**, 19–44.

Avrahami, H. M., Makovicky, P. J., Tucker, R. T. and Zanno, L. E. 2024. A new semi-fossorial thescelosaurine dinosaur from the Cenomanian-age Mussentuchit Member of the Cedar Mountain Formation, Utah. *The Anatomical Record*, **307**, 3717–3781.

Bailleul, A. M., Scannella, J. B., Horner, J. R. and Evans, D. C. 2016. Fusion patterns in the skulls of modern archosaurs reveal that sutures are ambiguous maturity indicators for the Dinosauria. *PLoS One*, **11**, e0147687.

Bapst, D. W. 2012. paleotree: an R package for paleontological and phylogenetic analyses of evolution. *Methods in Ecology and Evolution*, **3**, 803–807.

Barrett, P. M. and Maidment, S. C. R. 2017. The evolution of ornithischian quadrupedality. *Journal of Iberian Geology*, **43**, 363–377.

Barrett, P. M., Butler, R. J., Twitchett, R. J. and Hutt, S. 2011. New material of *Valdosaurus canaliculatus* (Ornithischia: Ornithopoda) from the Lower Cretaceous of southern England. *Special Papers in Palaeontology*, **86**, 131–163.

Baur, G. 1891. Remarks on the reptiles generally called Dinosauria. *The American Naturalist*, **25**, 434–454.

Bertozzo, F., Vecchia, F. M. D. and Fabbri, M. 2017. The Venice specimen of *Ouranosaurus nigeriensis* (Dinosauria, Ornithopoda). *PeerJ*, **5**, e3403.

Bertozzo, F., Kecheng, N., Gillette, N. V. and Godefroit, P. 2025. Anatomical description and digital reconstruction of the skull of *Jeholosaurus shangyuanensis* (Dinosauria, Ornithopoda) from China. *PLoS One*, **20**, e0312519.

Bonsor, J. A., Lockwood, J. A., Leite, J. V., Scott-Murray, A. and Maidment, S. C. 2023. The osteology of the holotype of the British iguanodontian dinosaur *Mantellisaurus atherfieldensis*. *Monographs of the Palaeontographical Society*, **177**, 1–63.

Boulenger, G. A. 1881. *Sur l'arc pelvien chez les dinosauriens de Bernissart. Bulletin de l'Académie Royale des Sciences, des Lettres et des Beaux-Arts de Belgique*, **1**. F. Hayez.

Boyd, C. A. 2014. The cranial anatomy of the neornithischian dinosaur *Thescelosaurus neglectus*. *PeerJ*, **2**, e669.

Brochu, C. A. 1996. Closure of neurocentral sutures during crocodilian ontogeny: implications for maturity assessment in fossil archosaurs. *Journal of Vertebrate Paleontology*, **16**, 49–62.

Brown, B. and Schlaikjer, E. M. 1940. The structure and relationships of *Protoceratops*. *Annals of the New York Academy of Sciences*, **40**, 133–265.

Bussert, R., Heinrich, W.-D. and Aberhan, M. 2009. The Tendaguru Formation (Late Jurassic to Early Cretaceous, southern Tanzania): definition, palaeoenvironments, and sequence stratigraphy. *Fossil Record*, **12**, 141–174.

Button, D. J. and Zanno, L. E. 2023. Neuroanatomy of the late Cretaceous *Thescelosaurus neglectus* (Neornithischia: Thescelosauridae) reveals novel ecological specialisations within Dinosauria. *Scientific Reports*, **13**, 19224.

Caldwell, H. R., Bedolla, E. and Varricchio, D. J. 2024. Patterns of postcranial fusion in the emu (*Dromaius novaehollandiae*) and Cretaceous theropod dinosaur *Troodon formosus*. *Journal of Vertebrate Paleontology*, **44** (6), e2493166.

Carpenter, K. and Galton, P. 2018. A photo documentation of bipedal ornithischian dinosaurs from the Upper Jurassic Morrison Formation, USA. *Geology of the Intermountain West*, **5**, 167–207.

Carpenter, K. and Lamanna, M. C. 2015. The braincase assigned to the ornithopod dinosaur *Uteodon* McDonald, 2011, reassigned to *Dryosaurus* Marsh, 1894: implications for iguanodontian morphology and taxonomy. *Annals of Carnegie Museum*, **83**, 149–165.

Carpenter, K. and Wilson, Y. 2008. A new species of *Camptosaurus* (Ornithopoda: Dinosauria) from the Morrison Formation (Upper Jurassic) of Dinosaur National Monument, Utah, and a biomechanical analysis of its forelimb. *Annals of Carnegie Museum*, **76**, 227–263.

Cau, A. 2024. A unified framework for predatory dinosaur macroevolution. *Bollettino della Società Paleontologica Italiana*, **63**, 1–19.

Chanthasit, P. 2010. The ornithopod dinosaur *Rhabdodon* from the Late Cretaceous of France: anatomy, systematics and paleobiology. PhD thesis, Université Claude Bernard-Lyon, 196 pp. https://theses.hal.science/tel-00841228v1

Chinnery, B. J. and Weishampel, D. B. 1998. *Montanoceratops cerorhynchus* (Dinosauria: Ceratopsia) and relationships among basal neoceratopsians. *Journal of Vertebrate Paleontology*, **18**, 569–585.

Cohen, K. M., Finney, S. C., Gibbard, P. L. and Fan, J.-X. 2013, updated. The ICS International Chronostratigraphic Chart. *Episodes*, **36**, 199–204.

Cruzado-Caballero, P., Fortuny, J., Llácer, S. and Canudo, J. I. 2015. Paleoneuroanatomy of the European lambeosaurine dinosaur *Arenysaurus ardevoli*. *PeerJ*, **3**, e802.

Currie, P. J., Holmes, R. B., Ryan, M. J. and Coy, C. 2016. A juvenile chasmosaurine ceratopsid (Dinosauria, Ornithischia) from the Dinosaur Park Formation, Alberta, Canada. *Journal of Vertebrate Paleontology*, **36**, e1048348.

De Klerk, W. J., Forster, C. A., Sampson, S. D., Chinsamy, A. and Ross, C. F. 2000. A new coelurosaurian dinosaur from the

Early Cretaceous of South Africa. *Journal of Vertebrate Paleontology*, **20**, 324–332.

Dieudonné, P.-E., Cruzado-Caballero, P., Godefroit, P. and Tortosa, T. 2021. A new phylogeny of cerapodan dinosaurs. *Historical Biology*, **33**, 2335–2355.

Díez Díaz, V., Akhlaq, S., Campbell, A., Depraetere, M., Mahlow-Tillack, K., Heumann, I. and Schwarz, D. 2025. Risks and responsibilities: the German Tendaguru Collection as cultural heritage and its 3D digitisation. 69–82. *In* Ioannides, M., Issini, G. and Oliveira, D. (eds) *3D research challenges in cultural heritage IV*. Springer, Lecture Notes in Computer Science 13577.

Dray, S. and Dufour, A.-B. 2007. The ade4 package: implementing the duality diagram for ecologists. *Journal of Statistical Software*, **22** (4), 1–20.

Dray, S., Dufour, A.-B., Thioulouse, J., Chessel, D., Jombart, T., Pavoine, S., Lobry, J. R., Ollier, S., Borcard, D., Legendre, P., Bougeard, S. and Siberchicot, A. 2025. ade4: analysis of ecological data: exploratory and Euclidean methods in environmental sciences. https://CRAN.R-project.org/package=ade4

Dunfee, D. R. 2022. Ontogenetic analysis of a juvenile braincase of the Upper Jurassic ornithopod dinosaur *Dryosaurus elderae*: new implications from microcomputed tomography. BSc thesis, Ohio University, 61 pp. http://rave.ohiolink.edu/etdc/view?acc_num=ouhonors1651234928992288

Escaso, F., Ortega, F., Dantas, P., Malafaia, E., Silva, B., Gasulla, J. M., Mocho, P., Narváez, I. and Sanz, J. L. 2014. A new dryosaurid ornithopod (Dinosauria, Ornithischia) from the Late Jurassic of Portugal. *Journal of Vertebrate Paleontology*, **34**, 1102–1112.

Evans, D. C., Reisz, R. R. and Dupuis, K. 2007. A juvenile *Parasaurolophus* (Ornithischia: Hadrosauridae) Braincase from Dinosaur Provincial Park, Alberta, with comments on crest ontogeny in the genus. *Journal of Vertebrate Paleontology*, **27**, 642–650.

Ezcurra, M. D. 2024. Exploring the effects of weighting against homoplasy in genealogies of palaeontological phylogenetic matrices. *Cladistics*, **40**, 242–281.

Farke, A. A., Chok, D. J., Herrero, A., Scolieri, B. and Werning, S. 2013. Ontogeny in the tube-crested dinosaur *Parasaurolophus* (Hadrosauridae) and heterochrony in hadrosaurids. *PeerJ*, **1**, e182.

Fonseca, A. O., Reid, I. J., Venner, A., Duncan, R. J., Garcia, M. S. and Müller, R. T. 2024. A comprehensive phylogenetic analysis on early ornithischian evolution. *Journal of Systematic Palaeontology*, **22** (1), 2346577.

Forster, C. 1990. The postcranial skeleton of the ornithopod dinosaur *Tenontosaurus tilletti*. *Journal of Vertebrate Paleontology*, **10**, 273–294.

Forster, C. A., De Klerk, W. J., Poole, K. E., Chinsamy-Turan, A., Roberts, E. M. and Ross, C. F. 2023. *Iyuku raathi*, a new iguanodontian dinosaur from the Early Cretaceous Kirkwood Formation, South Africa. *The Anatomical Record*, **306**, 1762–1803.

Fowler, D. W., Woodward, H. N., Freedman, E. A., Larson, P. L. and Horner, J. R. 2011. Reanalysis of "*Raptorex kriegsteini*": a juvenile tyrannosaurid dinosaur from Mongolia. *PLoS One*, **6**, e21376.

Fraas, E. 1908. Ostafrikanische dinosaurier. *Palaeontographica (1846–1933)*, **55**, 105–144.

Fronimos, J. A. and Wilson, J. A. 2017. Neurocentral suture complexity and stress distribution in the vertebral column of a sauropod dinosaur. *Ameghiniana*, **54**, 36–49.

Funston, G. F. 2024. Osteology of the two-fingered oviraptorid *Oksoko avarsan* (Theropoda: Oviraptorosauria). *Zoological Journal of the Linnean Society*, **202**, zlae011.

Gallina, P. A. 2011. Notes on the axial skeleton of the titanosaur *Bonitasaura salgadoi* (Dinosauria-Sauropoda). *Anais da Academia Brasileira de Ciências*, **83**, 235–246.

Galton, P. M. 1974. The ornithischian dinosaur *Hypsilophodon* from the Wealden of the isle of Wight. *Bulletin of the British Museum (Natural History) Geology*, **25**, 1–152.

Galton, P. M. 1975. English hypsilophodontid dinosaurs (Reptilia: Ornithischia). *Palaeontology*, **18**, 741–752.

Galton, P. M. 1977. The ornithopod dinosaur *Dryosaurus* and a Laurasia–Gondwanaland connection in the Upper Jurassic. *Nature*, **268**, 230–232.

Galton, P. M. 1981. *Dryosaurus*, a hypsilophodontid dinosaur from the Upper Jurassic of North America and Africa postcranial skeleton. *Paläontologische Zeitschrift*, **55**, 271–312.

Galton, P. M. 1983. The cranial anatomy of *Dryosaurus*, a hypsilophodontid dinosaur from the Upper Jurassic of North America and East Africa, with a review of hypsilophodontids from the Upper Jurassic of North America. *Geologica et Palaeontologica*, **17**, 207–243.

Galton, P. M. 1989. Crania and endocranial casts from ornithopod dinosaurs of the families Dryosauridae and Hypsilophodontidae (Reptilia: Ornithischia). *Geologica et Palaeontologica*, **23**, 217–239.

Galton, P. 2009. Notes on Neocomian (Lower Cretaceous) ornithopod dinosaurs from England – *Hypsilophodon*, *Valdosaurus*, '*Camptosaurus*', '*Iguanodon*' – and referred specimens from Romania and elsewhere. *Revue de Paleobiologie*, **28**, 211–273.

Galton, P. and Kermack, D. 2010. The anatomy of *Pantydraco caducus*, a very basal sauropodomorph dinosaur from the Rhaetian (Upper Triassic) of South Wales UK. *Revue de Paleobiologie*, **29**, 341–404.

Galton, P. M. and Taquet, P. 1982. *Valdosaurus*, a hypsilophodontid dinosaur from the Lower Cretaceous of Europe and Africa. *Geobios*, **15**, 147–159.

Gilmore, C. W. 1909. Osteology of the Jurassic reptile *Camptosaurus*, with a revision of the species of the genus, and descriptions of two new species. *Proceedings of the United States National Museum*, **36**, 197–332.

Gilmore, C. W. 1913. A new dinosaur from the Lance formation of Wyoming. *Smithsonian Miscellaneous Collections*, **61** (5), 1–5.

Gilmore, C. W. 1915. Osteology of *Thescelosaurus*, an orthopodous dinosaur from the Lance Formation of Wyoming. *Proceedings of the United States National Museum*, **49**, 591–616.

Gilmore, C. W. 1920. Osteology of the carnivorous Dinosauria in the United States National Museum: with special reference to the genera *Antrodemus* (*Allosaurus*) and *Ceratosaurus*. *Smithsonian Institution, United States National Museum, Bulletin*, **110**, 1–159.

Gilmore, C. W. 1925. Osteology of ornithopodous dinosaurs from the Dinosaur National Monument, Utah. *Memoirs of the Carnegie Museum*, **10**, 385–410.

Godefroit, P., Codrea, V. and Weishampel, D. B. 2009. Osteology of *Zalmoxes shqiperorum* (Dinosauria, Ornithopoda), based on new specimens from the Upper Cretaceous of Năălaţ ţ-Vad (Romania). *Geodiversitas*, **31**, 525–553.

Goloboff, P. A. and Morales, M. E. 2023. TNT version 1.6, with a graphical interface for MacOS and Linux, including new routines in parallel. *Cladistics*, **39**, 144–153.

Griffin, C. T. 2018. Developmental patterns and variation among early theropods. *Journal of Anatomy*, **232**, 604–640.

Griffin, C. T., Stocker, M. R., Colleary, C., Stefanic, C. M., Lessner, E. J., Riegler, M., Formoso, K., Koeller, K. and Nesbitt, S. J. 2021. Assessing ontogenetic maturity in extinct saurian reptiles. *Biological Reviews*, **96**, 470–525.

Hammer, Ø. and Harper, D. A. 2008. *Paleontological data analysis*. John Wiley & Sons.

Han, F.-L., Barrett, P. M., Butler, R. J. and Xu, X. 2012. Postcranial anatomy of *Jeholosaurus shangyuanensis* (Dinosauria, Ornithischia) from the Lower Cretaceous Yixian Formation of China. *Journal of Vertebrate Paleontology*, **32**, 1370–1395.

Harmon, L., Weir, J., Brock, C., Glor, R. and Challenger, W. 2008. GEIGER: investigating evolutionary radiations. *Bioinformatics*, **24**, 129–131.

Hatcher, J. B. 1903. Osteology of *Haplocanthosaurus*, with description of a new species and remarks on the probable habits of the Sauropoda and the age and origin of the *Atlantosaurus* beds. Additional remarks on *Diplodocus*. *Memoirs of the Carnegie Museum*, **2**, 1–75.

Haughton, S. H. 1915. On some dinosaur remains from Bushmanland. *Transactions of the Royal Society of South Africa*, **5** (1), 259–264.

Heinrich, W.-D. 1999. First haramiyid (Mammalia, Allotheria) from the Mesozoic of Gondwana. *Fossil Record*, **2**, 159–170.

Heinrich, C., Paes Neto, V. D., Lacerda, M. B., Martinelli, A. G., Fiedler, M. S. and Schultz, C. L. 2021. The ontogenetic pattern of neurocentral suture closure in the axial skeleton of Hyperodapedontinae (Archosauromorpha, Rhynchosauria) and its evolutionary implications. *Palaeontology*, **64**, 409–427.

Hennig, E. 1915. *Kentrosaurus aethiopicus*, der Stegosauride des Tendaguru. *Sitzungsberichte der Gesellschaft naturforschender Freunde zu Berlin*, **1915**, 219–247.

Herne, M. C., Tait, A. M., Weisbecker, V., Hall, M., Nair, J. P., Cleeland, M. and Salisbury, S. W. 2018. A new small-bodied ornithopod (Dinosauria, Ornithischia) from a deep, high-energy Early Cretaceous river of the Australian–Antarctic rift system. *PeerJ*, **5**, e4113.

Hofmann, R. and Sander, P. M. 2014. The first juvenile specimens of *Plateosaurus engelhardti* from Frick, Switzerland: isolated neural arches and their implications for developmental plasticity in a basal sauropodomorph. *PeerJ*, **2**, e458.

Hooley, R. W. 1925. On the skeleton of *Iguanodon atherfieldensis* sp. nov., from the Wealden Shales of Atherfield (Isle of Wight). *Quarterly Journal of the Geological Society of London*, **81**, 1–61.

Horner, H. R., Weishampel, D. B. and Forster, C. A. 2004. Hadrosauridae. 438–463. *In* Weishampel, D. B., Dodson, P. and Osmólska, H. (eds) *The Dinosauria*, Second edition. University of California Press.

Hübner, T. 2011. Ontogeny in *Dysalotosaurus lettowvorbecki*. PhD thesis, Ludwig-Maximilians-Universität, München, 318 pp.

Hübner, T. R. 2012. Bone histology in *Dysalotosaurus lettowvorbecki* (Ornithischia: Iguanodontia): variation, growth, and implications. *PLoS One*, **7**, e29958.

Hübner, T. 2018. The postcranial ontogeny of *Dysalotosaurus lettowvorbecki* (Ornithischia: Iguanodontia) and implications for the evolution of ornithopod dinosaurs. *Palaeontographica Abteilung A: Palaozoologie*, **310**, 43–120.

Hübner, T. R. and Rauhut, O. W. M. 2010. A juvenile skull of *Dysalotosaurus lettowvorbecki* (Ornithischia: Iguanodontia), and implications for cranial ontogeny, phylogeny, and taxonomy in ornithopod dinosaurs. *Zoological Journal of the Linnean Society*, **160**, 366–396.

Hübner, T. R., Foth, C., Heinrich, W.-D., Schwarz, D. and Bussert, R. 2021. Research history, taphonomy, and age structure of a mass accumulation of the ornithopod dinosaur *Dysalotosaurus lettowvorbecki* from the Upper Jurassic of Tanzania. *Acta Palaeontologica Polonica*, **66**, 275–300.

Hulke, J. W. 1880. *Iguanodon Prestwichii*, a new species from the Kimmeridge Clay, distinguished from *I. Mantelli* of the Wealden Formation in the S.E. of England and Isle of Wight by differences in the shape of the vertebral centra, by fewer than five sacral vertebrœ, by the simpler character of its tooth-serrature, &c., founded on numerous fossil remains lately discovered at Cumnor, near Oxford. *Quarterly Journal of the Geological Society of London*, **36**, 433–456.

Huxley, T. H. 1870. On *Hypsilophodon foxii*, a new dinosaurian from the Wealden of the Isle of Wight. *Quarterly Journal of the Geological Society of London*, **26**, 3–12.

Ikejiri, T. 2003. Sequence of closure of neurocentral sutures in *Camarasaurus* (Sauropoda) and implications for phylogeny in Reptilia. *Journal of Vertebrate Paleontology*, **23**, 65A.

Ikejiri, T. 2012. Histology-based morphology of the neurocentral synchondrosis in *Alligator mississippiensis* (Archosauria, Crocodylia). *The Anatomical Record*, **295**, 18–31.

Irmis, R. B. 2007. Axial skeleton ontogeny in the Parasuchia (Archosauria: Pseudosuchia) and its implications for ontogenetic determination in archosaurs. *Journal of Vertebrate Paleontology*, **27**, 350–361.

Janensch, W. 1914a. Bericht über den Verlauf der Tendaguru-Expedition. *Archiv für Biontologie*, **3**, 15–58.

Janensch, W. 1914b. Übersicht über die Wirbeltierfauna der Tendaguruschichten, nebst einer kurzer Charakterisierung der neu aufgeführten Arten von Sauropoden. *Archiv für Biontologie*, **3**, 226–261.

Janensch, W. 1920. Über *Elaphrosaurus bambergi* und die megalosaurier aus den Tendaguru-Schichten Deutsch-Ostafrikas. *Sitzungsberichte der Gesellschaft Naturforschender Freunde zu Berlin*, **1920**, 226–235.

Janensch, W. 1955. Der Ornithopode *Dysalotosaurus* der Tendaguruschichten. *Palaeontographica-Supplementbände*, **7**, 105–176.

Kellner, A. and Tomida, Y. 2000. Description of a new species of Anhangueridae (Pterodactyloidea) with comments on the pterosaur fauna from the Santana Formation (Aptian–Albian), northeastern Brazil. *National Science Museum Monographs*, **17**, 9–137.

Klingenberg, C. P. 1996. Multivariate allometry. 23–49. *In* Marcus, L. F., Corti, M., Loy, A., Naylor, G. J. P. and Slice, D. E. (eds) *Advances in morphometrics*. Springer.

Krumenacker, L. J., Varricchio, D. J., Organ, C., Gardner, J. D., Britt, B. B. and Boyd, C. 2023. Osteology and phylogenetic relationships of the mid-Cretaceous neornithischian dinosaur *Oryctodromeus cubicularis* Varricchio, 2007. *Journal of Vertebrate Paleontology*, **43**, e2330581.

Kuzmin, I. T., Boitsova, E. A., Gombolevskiy, V. A., Mazur, E. V., Morozov, S. P., Sennikov, A. G., Skutschas, P. P. and Sues, H.-D. 2021. Braincase anatomy of extant Crocodylia, with new insights into the development and evolution of the neurocranium in crocodylomorphs. *Journal of Anatomy*, **239**, 983–1038.

Lania, A., Pabst, B. and Scheyer, T. M. 2025. Craniomandibular osteology of a new massopodan sauropodomorph (Dinosauria: Sauropodomorpha) from the Late Triassic (latest Norian) of Canton Aargau, Switzerland. *Swiss Journal of Palaeontology*, **144**, 39.

Lautenschlager, S. and Hübner, T. 2013. Ontogenetic trajectories in the ornithischian endocranium. *Journal of Evolutionary Biology*, **26**, 2044–2050.

Lockwood, J. A. F., Martill, D. M. and Maidment, S. C. R. 2021. A new hadrosauriform dinosaur from the Wessex Formation, Wealden Group (Early Cretaceous), of the Isle of Wight, southern England. *Journal of Systematic Palaeontology*, **19**, 847–888.

Lockwood, J. A. F., Martill, D. M. and Maidment, S. C. R. 2024. *Comptonatus chasei*, a new iguanodontian dinosaur from the Lower Cretaceous Wessex Formation of the Isle of Wight, southern England. *Journal of Systematic Palaeontology*, **22**, 2346573.

Lydekker, R. 1889. On the Remains and Affinities of five Genera of Mesozoic Reptiles. *Quarterly Journal of the Geological Society of London*, **45**, 41–59.

Maddison, W. P. and Maddison, D. R. 2021. Mesquite: a modular system for evolutionary analysis, version 3.81. https://www.mesquiteproject.org/

Madzia, D., Arbour, V. M., Boyd, C. A., Farke, A. A., Cruzado-Caballero, P. and Evans, D. C. 2021. The phylogenetic nomenclature of ornithischian dinosaurs. *PeerJ*, **9**, e12362.

Maidment, S. C. R. and Barrett, P. M. 2011. The locomotor musculature of basal ornithischian dinosaurs. *Journal of Vertebrate Paleontology*, **31**, 1265–1291.

Maidment, S. C. R., Chapelle, K. E. J., Bonsor, J. A., Button, D. and Barrett, P. M. 2022. Osteology and relationships of *Cumnoria prestwichii* (Ornithischia: Ornithopoda) from the Late Jurassic of Oxfordshire, UK. *Monographs of the Palaeontographical Society*, **176**, 1–55.

Maier, G. 2003. *African dinosaurs unearthed: The Tendaguru expeditions*. Indiana University Press.

Maisch, M. W. and Matzke, A. T. 2019. An isolated dinosaurian prootic with possible stegosaurian affinities (Dinosauria: Thyreophora) from the Upper Jurassic Qigu Formation of the southern Junggar Basin, NW-China. *Neues Jahrbuch für Geologie und Paläontologie – Abhandlungen*, **294**, 275–283.

Malafaia, E., Mocho, P., Escaso, F. and Ortega, F. 2017. A juvenile allosauroid theropod (Dinosauria, Saurischia) from the Upper Jurassic of Portugal. *Historical Biology*, **29**, 654–676.

Mantell, G. A. 1825. VIII. Notice on the *Iguanodon*, a newly discovered fossil reptile, from the sandstone of Tilgate, in Sussex. *Philosophical Transactions of the Royal Society of London*, **115**, 179–186.

Marsh, O. C. 1878. Principal characters of American Jurassic dinosaurs. *American Journal of Science*, **3**, 411–416.

Marsh, O. C. 1879. Notice of new Jurassic reptiles. *American Journal of Science, Series 3*, **18**, 501–505.

Marsh, O. C. 1881. Principal characters of American Jurassic dinosaurs. Part IV. Spinal cord, pelvis, and limbs of *Stegosaurus*. *American Journal of Science, Series 3*, **21**, 167–170.

Marsh, O. C. 1894. The typical Ornithopoda of the American Jurassic. *American Journal of Science, Series 3*, **48**, 85–90.

Mateus, O. and Antunes, M. T. 2001. *Draconyx loureiroi*, a new camptosauridae (Dinosauria, Ornithopoda) from the Late Jurassic of Lourinhã, Portugal. *Annales de Paléontologie*, **87**, 61–73.

Matheron, P. 1869. Notice sur les reptiles fossiles des dépôts fluvio-lacustres crétacés du bassin à lignite de Fuveau. *Mémoires de l'Académie des Sciences, Belles-Lettres, et Arts de Marseille*, **1868–1869**, 345–379.

McDonald, A. T. 2011. The taxonomy of species assigned to *Camptosaurus* (Dinosauria: Ornithopoda). *Zootaxa*, **2783**, 52–68.

McDonald, A. T., Kirkland, J. I., Deblieux, D. D., Madsen, S. K., Cavin, J., Milner, A. R. and Panzarin, L. 2010. New basal iguanodonts from the Cedar Mountain Formation of Utah and the evolution of thumb-spiked dinosaurs. *PLoS One*, **5**, e14075.

Melstrom, K. M., D'Emic, M. D., Chure, D. and Wilson, J. A. 2016. A juvenile sauropod dinosaur from the Late Jurassic of Utah, U.S.A., presents further evidence of an avian style air-sac system. *Journal of Vertebrate Paleontology*, **36**, e1111898.

Milner, A. R. and Norman, D. B. 1984. The biogeography of advanced ornithopod dinosaurs (Archosauria: Ornithischia): a cladistic-vicariance model. 145–150. *In* Reif, W.-E. and Westphal, F. (eds) *Third symposium on Mesozoic terrestrial ecosystems, short papers*. Attempto Verlag, Tübingen, 259 pp.

Nesbitt, S. 2007. The anatomy of *Effigia okeeffeae* (Archosauria, Suchia), theropod-like convergence, and the distribution of related taxa. *Bulletin of the American Museum of Natural History*, **2007**, 1–84.

Nesbitt, S. J. 2011. The early evolution of archosaurs: relationships and the origin of major clades. *Bulletin of the American Museum of Natural History*, **2011**, 1–292.

Nesbitt, S. J., Denton, R. K., Loewen, M. A., Brusatte, S. L., Smith, N. D., Turner, A. H., Kirkland, J. I., McDonald, A. T. and Wolfe, D. G. 2019. A mid-Cretaceous tyrannosauroid and the origin of North American end-Cretaceous dinosaur assemblages. *Nature Ecology & Evolution*, **3**, 892–899.

Nopcsa, F. 1902. Dinosaurierreste aus Sieben bürgen II. (Schädelreste von *Mochlodon*). Mit einem Anhange: zur Phylogenie der Ornithopodiden. Mit einem Anhange: zur Phylogenie der Ornithopodiden. *Denkschriften der* *königlichen Akademie der Wissenschaften. Mathematisch-Naturwissenschaftlichen Klasse*, **72**, 149–175.

Norman, D. B. 1980. On the ornithischian dinosaur *Iguanodon bernissartensis* from the Lower Cretaceous of Bernissart (Belgium). *Memoires de l'Institut Royal des Sciences Naturelles de Belgique*, **178**, 1–103.

Norman, D. B. 1986. On the anatomy of *Iguanodon atherfieldensis* (Ornithischia: Ornithopoda). *Memoires de l'Institut Royal des Sciences Naturelles de Belgique, Sciences de la Terre*, **56**, 281–372.

Norman, D. B. 2002. On Asian ornithopods (Dinosauria: Ornithischia). 4. *Probactrosaurus*. *Zoological Journal of the Linnean Society*, **136**, 113–144.

Norman, D. B. 2004. Basal Iguanodontia. 413–437. *In* Weishampel, D. B., Dodson, P. and Osmólska, H. (eds) *The Dinosauria*, Second edition. University of California Press.

Novas, F. E., Cambiaso, A. V. and Ambrosio, A. 2004. A new basal iguanodontian (Dinosauria, Ornithischia) from the Upper Cretaceous of Patagonia. *Ameghiniana*, **41**, 75–82.

O'Connor, P. M. 2007. The postcranial axial skeleton of *Majungasaurus crenatissimus* (Theropoda: Abelisauridae) from the Late Cretaceous of Madagascar. *Journal of Vertebrate Paleontology*, **27**, 127–163.

Oelrich, T. M. 1956. The anatomy of the head of *Ctenosaura pectinata* (Iguanidae). *Miscellaneous Publications of the Museum of Zoology of the University of Michigan*, **94**, 1–122.

Ostrom, J. 1970. Stratigraphy and paleontology of the Cloverly Formation (Lower Cretaceous) of the Bighorn Basin area, Wyoming and Montana. *Bulletin of the Peabody Museum of Natural History*, 35.

Owen, R. 1842. Report on British fossil reptiles. Part II. 60–204. *In* British Association (ed.) *Report of the eleventh meeting of the British Association for the Advancement of Science, held at Plymouth in July 1841*. John Murray, London.

Panciroli, E., Funston, G. F., Maidment, S. C. R., Butler, R. J., Benson, R. B. J., Crawford, B. L., Fair, M., Fraser, N. C. and Walsh, S. 2025. The first and most complete dinosaur skeleton from the Middle Jurassic of Scotland. *Earth and Environmental Science Transactions of the Royal Society of Edinburgh*, **116** (1–2), 1–12.

Paradis, E. and Schliep, K. 2018. ape 5.0: an environment for modern phylogenetics and evolutionary analyses in R. *Bioinformatics*, **35**, 526–528.

Paul, G. S. 2008. A revised taxonomy of the iguanodont dinosaur genera and species. *Cretaceous Research*, **29**, 192–216.

Pompeckj, J. F. 1920. Das angebliche Vorkommen und Wandern des Parietalforamens bei Dinosauriern. *Sitzungsberichte der Gesellschaft Naturforschender Freunde zu Berlin*, **3**, 109–129.

Poole, K. 2022. Phylogeny of iguanodontian dinosaurs and the evolution of quadrupedality. *Palaeontologia Electronica*, **25**, a30.

Poole, K. 2023. Placing juvenile specimens in phylogenies: an ontogenetically sensitive phylogenetic assessment of a new genus of iguanodontian dinosaur from the Early Cretaceous Kirkwood Formation, South Africa. *The Anatomical Record*, **306**, 1939–1950.

Poust, A. W., Gao, C., Varricchio, D. J., Wu, J. and Zhang, F. 2020. A new microraptorine theropod from the Jehol Biota and growth in early dromaeosaurids. *The Anatomical Record*, **303**, 963–987.

Prieto-Márquez, A. 2011. Cranial and appendicular ontogeny of *Bactrosaurus johnsoni*, a hadrosauroid dinosaur from the Late Cretaceous of northern China. *Palaeontology*, **54**, 773–792.

R Core Team 2024. R: a language and environment for statistical computing. R Foundation for Statistical Computing. https://www.R-project.org

Reck, H. 1913. *GTE Field Catalogue, 1912–1913*. Pal. Mus SII, Tendaguru-Expedition, **9**.

Revell, L. J. 2024. phytools 2.0: an updated R ecosystem for phylogenetic comparative methods (and other things). *PeerJ*, **12**, e16505.

Rocchi, R., Rotatori, F. M., Ferreira, G. S. and Fanti, F. 2026a. Media of 'An exquisitely preserved young iguanodontian from the Upper Jurassic of Tanzania sheds light on skeletal fusion patterns within Archosauria' [dataset]. MorphoSource. https://www.morphosource.org/projects/000774830

Rocchi, R., Rotatori, F. M., Ferreira, G. S. and Fanti, F. 2026b. Project 6025: An exquisitely preserved young iguanodontian from the Upper Jurassic of Tanzania sheds light on skeletal fusion patterns within Archosauria [dataset]. MorphoBank. https://www.morphobank.org/permalink/?P6025

Rotatori, F. M., Moreno-Azanza, M. and Mateus, O. 2020. New information on ornithopod dinosaurs from the Late Jurassic of Portugal. *Acta Palaeontologica Polonica*, **65**, 35–57.

Rotatori, F. M., Moreno-Azanza, M. and Mateus, O. 2022. Reappraisal and new material of the holotype of *Draconyx loureiroi* (Ornithischia: Iguanodontia) provide insights on the tempo and mode of evolution of thumb-spiked dinosaurs. *Zoological Journal of the Linnean Society*, **195**, 125–156.

Rotatori, F. M., Ferrari, L., Sequero, C., Camilo, B., Mateus, O. and Moreno-Azanza, M. 2023. An unexpected early-diverging iguanodontian dinosaur (Ornithischia, Ornithopoda) from the Upper Jurassic of Portugal. *Journal of Vertebrate Paleontology*, **43**, e2310066.

Rotatori, F. M., Escaso, F., Camilo, B., Bertozzo, F., Malafaia, E., Mateus, O., Mocho, P., Ortega, F. and Moreno-Azanza, M. 2025. Evidence of large-sized ankylopollexian dinosaurs (Ornithischia: Iguanodontia) in the Upper Jurassic of Portugal. *Journal of Systematic Palaeontology*, **23**, 2470789.

Rotatori, F. M., Chiarenza, A. A., Fanti, F. and Moreno-Azanza, M. 2026. The early origin of Iguanodontia: new insights into the macroevolution, diversity and biogeography of the clade. *Palaeontology*, **69**, e70057.

Rozadilla, S., Agnolín, F. L. and Novas, F. E. 2019. Osteology of the Patagonian ornithopod *Talenkauen santacrucensis* (Dinosauria, Ornithischia). *Journal of Systematic Palaeontology*, **17**, 2043–2089.

Rozhdestvensky, A. K. 1966. New iguanodonts from Central Asia: phylogenetic and taxonomic relationships between late Iguanodontidae and early Hadrosauridae. *Paleontological Journal*, **1966**, 103–116.

Ruiz-Omeñaca, J. I., Pereda Suberbiola, X. and Galton, P. M. 2006. *Callovosaurus leedsi*, the earliest dryosaurid dinosaur (Ornithischia: Euornithopoda) from the Middle Jurassic of England. 3–16. *In* Carpenter, K. (ed.) *Horns and beaks: Ceratopsian and ornithopod dinosaurs*. Indiana University Press.

Russell, D., Beland, P. and McIntosh, J. S. 1980. Paleoecology of the dinosaurs of Tendaguru (Tanzania). *Memoires de Societe Geologique de France*, **59**, 169–175.

Sadleir, R., Barrett, P. and Powell, H. 2008. The anatomy and systematics of *Eustreptospondylus oxoniensis*, a theropod dinosaur from the Middle Jurassic of Oxfordshire, England. *Monograph of the Palaeontographical Society*, **160**, 1–82, pl. 1.

Sames, B. 2008. Application of Ostracoda and Charophyta from the Late Jurassic to Early Cretaceous Tendaguru formation at Tendaguru, Tanzania (East Africa): biostratigraphy, palaeobiogeography and palaeoecology. *Palaeogeography, Palaeoclimatology, Palaeoecology*, **264**, 213–229.

Sampson, S. D. and Witmer, L. M. 2007. Craniofacial anatomy of *Majungasaurus crenatissimus* (Theropoda: Abelisauridae) from the Late Cretaceous of Madagascar. *Journal of Vertebrate Paleontology*, **27**, 32–104.

Sánchez-Fenollosa, S., Verdú, F. J. and Cobos, A. 2023. The largest ornithopod (Dinosauria: Ornithischia) from the Upper Jurassic of Europe sheds light on the evolutionary history of basal ankylopollexians. *Zoological Journal of the Linnean Society*, **199**, 1013–1033.

Scheetz, R. D. 1999. Osteology of *Orodromeus makelai* and the phylogeny of basal ornithopod dinosaurs. PhD thesis, Montana State University, United States, Montana, 186 pp.

Schwarz, D., Fritsch, G., Issever, A. S., Berlin, C. U. and Hildebrandt, T. 2023. Description of contents of unopened bamboo corsets and crates from Quarry Ig/WJ of the Tendaguru locality (Late Jurassic, Tanzania, East Africa) as revealed by medical CT data and the potential of this data under paleontological and historical aspects. *Palaeontologia Electronica*, **26**, a4.

Seeley, H. G. 1888. I. On the classification of the fossil animals commonly named Dinosauria. *Proceedings of the Royal Society of London*, **43**, 165–171.

Sereno, P. C. 1986. Phylogeny of the bird-hipped dinosaurs (Order Ornithischia). *National Geographic Research*, **2**, 234–256.

Sereno, P. C. 1991. *Lesothosaurus*, “Fabrosaurids,” and the early evolution of Ornithischia. *Journal of Vertebrate Paleontology*, **11**, 168–197.

Shepherd, J., Galton, P. M. and Jensen, J. A. 1977. Additional specimens of the hypsilophodontid dinosaur *Dryosaurus altus* from the Upper Jurassic of western North America. *Brigham Young University Geological Studies*, **24**, 11–15.

Slowikowski, K., Schep, A., Hughes, S., Dang, T. K., Lukauskas, S., Irisson, J.-O., Kamvar, Z. N., Ryan, T., Christophe, D., Hiroaki, Y., Gramme, P., Abdol, A. M., Barrett, M., Cannoodt, R., Krassowski, M., Chirico, M., Aphalo, P. and Barton, F. 2024. ggrepel: Automatically position non-overlapping text labels with ‘ggplot2’. https://cran.r-project.org/web/packages/ggrepel/index.html

Sobral, G., Hipsley, C. A. and Müller, J. 2012. Braincase redescription of *Dysalotosaurus lettowvorbecki* (Dinosauria, Ornithopoda) based on computed tomography. *Journal of Vertebrate Paleontology*, **32**, 1090–1102.

Starck, J. M. 1993. Evolution of avian ontogenies. 275–366. *In* Power, D. M. (ed.) *Current ornithology*. Springer.

Sues, H.-D. 1980. A pachycephalosaurid dinosaur from the Upper Cretaceous of Madagascar and its paleobiogeographical implications. *Journal of Paleontology*, **54**, 954–962.

Taquet, P. 1976. *Géologie et paléontologie du gisement de Gadoufaoua (aptien du Niger)*, Cahiers de Paléontologie. Centre national de la Recherche scientifique, Paris.

Thomas, D. 2015. The cranial anatomy of *Tenontosaurus tilletti* Ostrom, 1970 (Dinosauria, Ornithopoda). *Palaeontologia Electronica*, **18**, 1–99.

Tschopp, E. and Mateus, O. 2017. Osteology of *Galeamopus pabsti* sp. nov. (Sauropoda: Diplodocidae), with implications for neurocentral closure timing, and the cervico-dorsal transition in diplodocids. *PeerJ*, **5**, e3179.

Uhen, M. D., Allen, B., Behboudi, N., Clapham, M. E., Dunne, E., Hendy, A., Holroyd, P. A., Hopkins, M., Mannion, P., Novack-Gottshall, P., Pimiento, C. and Wagner, P. 2023. Paleobiology database user guide version 1.0. *PaleoBios*, **40** (11), 1–56.

Varricchio, D. J., Martin, A. J. and Katsura, Y. 2007. First trace and body fossil evidence of a burrowing, denning dinosaur. *Proceedings of the Royal Society B*, **274**, 1361–1368.

Vazquez, A. 2024. *MeasureIt*. Blender extensions. https://extensions.blender.org/add-ons/measureit/ [accessed 17 May 2025]

Verdú, F. J., Royo-Torres, R., Cobos, A. and Alcalá, L. 2015. Perinates of a new species of *Iguanodon* (Ornithischia: Ornithopoda) from the lower Barremian of Galve (Teruel, Spain). *Cretaceous Research*, **56**, 250–264.

Verrière, A., Fröbisch, N. B. and Fröbisch, J. 2022. Regionalization, constraints, and the ancestral ossification patterns in the vertebral column of amniotes. *Scientific Reports*, **12**, 22257.

Vila, B., Sellés, A., Moreno-Azanza, M., Razzolini, N. L., Gil-Delgado, A., Canudo, J. I. and Galobart, À. 2022. A titanosaurian sauropod with Gondwanan affinities in the latest Cretaceous of Europe. *Nature Ecology and Evolution*, **6**, 288–296.

Virchow, H. 1919. *Atlas und Epistropheus bei den Schildkröten. Sitzungsberichte Der Gesellschaft Naturforschender Freunde Zu Berlin*, **8**. R. Friedländer und Sohn.

Wang, R. and Pei, R. 2025. The smallest known specimen of *Microraptor* (Dinosauria: Dromaeosauridae) from the Jiufotang Formation in northeastern China. *Historical Biology*, **37**, 1757–1767.

Weishampel, D. B., Jianu, C.-M., Csiki, Z. and Norman, D. B. 2003. Osteology and phylogeny of *Zalmoxes* (n. g.), an unusual euornithopod dinosaur from the latest Cretaceous of Romania. *Journal of Systematic Palaeontology*, **1**, 65–123.

Wickham, H., Vaughan, D., Girlich, M. and Ushey, K. 2024. tidyr: Tidy messy data. https://cran.r-project.org/web/packages/tidyr/index.html

Wickham, H., Chang, W., Henry, L., Pedersen, T. L., Takahashi, K., Wilke, C., Woo, K., Yutani, H., Dunnington, D. and van den Brand, T. 2025. ggplot2: Create elegant data visualisations using the grammar of graphics. https://cran.r-project.org/web/packages/ggplot2/index.html

Wilson, J. A. 1999. A nomenclature for vertebral laminae in sauropods and other saurischian dinosaurs. *Journal of Vertebrate Paleontology*, **19**, 639–653.

Wilson, J. A. 2002. Sauropod dinosaur phylogeny: critique and cladistic analysis. *Zoological Journal of the Linnean Society*, **136**, 215–275.

Winkler, D. A., Murry, P. A. and Jacobs, L. L. 1997. A new species of *Tenontosaurus* (Dinosauria: Ornithopoda) from the Early Cretaceous of Texas. *Journal of Vertebrate Paleontology*, **17**, 330–348.

Witzmann, F., Asbach, P., Remes, K., Hampe, O., Hilger, A. and Paulke, A. 2008. Vertebral pathology in an ornithopod dinosaur: a hemivertebra in *Dysalotosaurus lettowvorbecki* from the Jurassic of Tanzania. *The Anatomical Record*, **291**, 1149–1155.

Witzmann, F., Claeson, K. M., Hampe, O., Wieder, F., Hilger, A., Manke, I., Niederhagen, M., Rothschild, B. M. and Asbach, P. 2011. Paget disease of bone in a Jurassic dinosaur. *Current Biology*, **21**, R647–R648.

Xu, X., Wang, X.-L. and You, H.-L. 2000. A primitive ornithopod from the Early Cretaceous Yixian Formation of Liaoning. *Vertebrata PalAsiatica*, **38**, 318–325.

Xu, X., Norell, M. A., Kuang, X., Wang, X., Zhao, Q. and Jia, C. 2004. Basal tyrannosauroids from China and evidence for protofeathers in tyrannosauroids. *Nature*, **431**, 680–684.

Yates, A. M. 2003. A new species of the primitive dinosaur *Thecodontosaurus* (Saurischia: Sauropodomorpha) and its implications for the systematics of early dinosaurs. *Journal of Systematic Palaeontology*, **1**, 1–42.

Yu, C., Prieto-Marquez, A., Chinzorig, T., Badamkhatan, Z. and Norell, M. 2020. A neoceratopsian dinosaur from the early Cretaceous of Mongolia and the early evolution of Ceratopsia. *Communications Biology*, **3**, 499.

Zanno, L. E., Gates, T. A., Avrahami, H. M., Tucker, R. T. and Makovicky, P. J. 2023. An early-diverging iguanodontian (Dinosauria: Rhabdodontomorpha) from the Late Cretaceous of North America. *PLoS One*, **18**, e0286042.